Tesis Doctoral

Experimentos fotónicos de tomografía selectiva y eficiente de procesos cuánticos

Schmiegelow, Christian Tomás

2011

UNIVERSIDAD DE BUENOS AIRES
Facultad de Ciencias Exactas y Naturales
Departamento de Física

Experimentos fotónicos de tomografía selectiva y eficiente de procesos cuánticos

Trabajo de Tesis para optar por el título de
Doctor de la Universidad de Buenos Aires
en el Área Ciencias Físicas
por Christian Tomás Schmiegelow

Director de Tesis: Juan Pablo Paz
Director Asistente de Tesis: Miguel Antonio Larotonda
Consejero de Estudios: Fernando Lombardo
Lugar de Trabajo: Depto. de Física, FCEyN, UBA

Octubre 2011

Resumen

Esta tesis presenta la primer demostración experimental de un nuevo método para caracterizar la evolución de sistemas cuánticos de un modo eficiente y selectivo. Es el resultado de una colaboración entre teóricos y experimentales en la búsqueda de métodos que permitan caracterizar, controlar y entender el comportamiento de sistemas cuánticos con el objetivo de poder realizar tareas de información cuántica. Está dividida en dos partes. En la primer parte se desarrollan las bases experimentales y describe el armado del laboratorio. Las técnicas experimentales utilizadas y las ideas fundamentales relacionadas con el uso de fotones como objetos capaces de procesar información cuántica son descriptas. La segunda parte primero revee distintos métodos de tomografía de procesos cuánticos con especial énfasis en el método que implementamos experimentalmente por primera vez: tomografía de procesos cuánticos selectiva y eficiente. Finalmente, se describe la impementación experimental de este nuevo método en sistemas de uno y dos qubits. Las diferentes evoluciones estudiadas presentan clara evidencia de su perfomance robusta en la determinación de propiedades de un sistema de un modo eficiente y selectivo.

Palabras Clave: información cuántica, óptica cuántica, tomografía de procesos cuánticos.

Photonic experiments on selective efficient quantum process tomography

Abstract

This thesis presents the first experimental demonstration of a new method to characterize the evolution of quantum systems in an efficient and selective manner. It is the result of the joint collaboration between theoreticians and experimentalists in a quest to characterize, control and understand the behaviour of quantum systems in order to perform quantum information tasks. It is divided into two parts. The first part covers the experimental foundations and set up of the laboratory. Experimental techniques used and the basic ideas regarding using single photons as quantum information processing devices are detailed. The second part first reviews different methods for quantum process tomography with special emphasis in the method we experimentally implement for the first time: selective efficient quantum process tomography. Finally, the experimental implementation of this new method on one and two qubit systems is presented. Different evolutions are studied presenting clear evidence of its robust performance in determining in their properties in an efficient and selective manner.

Key Words: quantum information, quantum optics, quantum process tomography.

Agradecimientos

A mis directores. A Juan Pablo por darme la oportunidad de tabajar en física experimental. Y a Richi por haberme enseñado a ser un físico experimental.

A mi madre y hermanos. Por su incondicional apoyo siempre.

A mis amigos de antaño. A Alex, Damu, Dani, Franco, Mateo, Pol, Quielo y Tomi. Y a las divinas de sus novias: Andru, Ine, Maru y Sofi. Y a las ex-novias de Mat y a las amigas de ellas: en especial a Agus y a Lu.

A Martín. Por los mejores tres años de mi vida, en los que además hice los experimentos de esta tésis.

A mis compañeros de trabajo UBA. A los compañeros de los quantum drunken: Augusto, Leo, Ceci y Ariel y todos los que alguna vez pasaron a tomar una cerveza o contar algo de física. A Ceci por sus incansable manera de ofrecer siempre las mejores recomendaciones y por su, también incansable, espíritu de fiesta. A Ariel con quien no solo tuve el placer de compartir oficina durante casi toda la tesis sino con quién drisfruté muchísimo trabajando juntos en el segundo experimento de esta tesis. A Bruno, de quien esperamos que siga nuestro legado (sea lo que sea que eso signifique...). A Fernando Pastwaski con quien compartí el primer año de mi tesis y me ayudó a pensar los primeros experimentos. Tambinén a Nahuel, Esteban y Gaby.

A los compañeros de la FIFA con quienes empezamos los encuentros nacionales de estudiantes de física que se vienen sosteniendo desde ya más 5 años cuando nos juntamos para organizar por primer vez algo en la AFA de San Luis en el 2006. En especial a Emiliano y a Ro.

A una infinidad de amigos con los que compartí distintas actividades entre lo académico, lo recreacional y lo personal. Al Zeke con quién emigré desde La Plata. A Pedro Fontanarrosa. A Diana L.N., Diego P.D., Esteban D., Adrián R.L., Pato G., Vero P.S., Sebi G., Guille P., Vico, Paco, Maia B., Bruno D., Flor A., Marcos T., Yoni S., Tati A.A., Ana A., Enzo T., Mati G., Flor C., Nico N.M., Manu G., Nico E., Inés L., Manu S., el Funes, Fede H., Gus, el Hippie, Juan Pablo D.B., Santi, Bernardo C., Guada R., Bruno M.,Nahuel S., Belu L., Francisco B., ...

A los amigos de DISEN (Diversidad Sexual en Exactas y Naturales).

A todos los estudiantes con los que compartí laboratorio. A Mónica Aguero. A todos los que hicieron labo 6 y 7 en CITEDEF cerca mío: a Hernan B. y Luciano P; a Sabrina S. y Nahuel F.; a Fede B. y Gaby P.; a Pablo T.A.; a Laura K. y Nacho L.G. A los estudiantes de licenciatura que pasaron por el labo en estos años: Griselda M. y Julián D.

A los Jóvenes Ópticos y Fotofísicos de la Argentina (JOFA). Con quienes organizamos las escuelas apéndices del topfot. En especial Alberto Lencina gran amigo y compañero. A Francisco V., Martín P., Ligia C.B., Celeste D, María Luz M.R., Vivian G., Mauro C., Ariel L., Fabian V. y Fernando A.

A los docentes del DF de la UBA. A Fernando Lomabardo que fue mi consejero de estudios. A Silvia Ledesma y Claudio Iemmi por haber abierto las puertas de su laboratorio para que hicieramos el un experimento de Imágenes Fantasmas. A Ricardo Piegaia por haberme acercado la demostración del Apéndice F. A Cristina Caputo, Gabo Mindling, Oscar Martinez y a todos los que alguna vez tuvieron paciencia para darme una mano.

A Carlos Saavedra quien en una visita me señaló la importancia de la estabilización activa ahorándome largas horas de lucha contra fluctuaciones térmicas y mecánicas.

A mis compañeros de trabajo CITEDEF. En especial a Jorge Codnia, amigo y compaẽro de trabajo; por haberme dado una mano siempre que la necesité, especialmente en cosas de electrónica. A Francis M., Laura A., Nico G. y el resto de los compaẽros de los otros laboratorios; también a Alejando H. y Marcelo K.

A los técnicos de CITEDEF que se bancaron mis nervios cuando necesitaba una pieza rápido. En especial a José L., Luis F. y el equipo de Mario P. en el taller central.

A los colegas ópticos e infromáticos cuánticos latinoamericanos. A Bruno Taketani con quien hicimos los planes del experimento de teleportación ruidosa. A Oishvaldo, Gabo, Adriana, los Brunos, los Rafaeles, Gabi, Planeta, Barbara, Agatha, Mafalda, el Colo, Alejo S., ...

A los colegas infromáticos cuánticos de la argentina con quien más de una vez disfruté discutiendo física. En especial a Mauricio M., Lorena R y Martín B.

A los compañeros de la escuela balseiro 2007. En especial a Pato G., Any Z., Fede P., Valeria P., Nati M. y el Rucki.

A los compañeros del Bachillerato Popular Simón Rodriguez.

A mis compañeros en Alemania. Frank, Max, Daniel, Thomas, Amado, Niels, Yens, Uli, Tim, Koni, Georg, Sam, Michael, the Stephans, Kilian, Christine, Elvira y especialmente a Ferdinand Schmidt-Kaler que me invitá a trabajar en su grupo por tres meses.

A la comunidad open source. Buena parte de esta tesis fue hecha con software libre. Firme en la convicción de que ese es el modelo para desarrollar software.

Al pueblo argentino. Me bancó mis estudios de doctorado. Con él me comprometo a trabajar duro con un objetivo en la frente. El ojetivo de que lo que aprendí sirva para mejorar la manera en la que vivimos.

Contents

Publications List

During the elaboration of this thesis the following publications were produced:

- Articles in journals.

  2011 **Selective and Efficient Quantum Process Tomography without Ancilla**
  C.T. Schmiegelow, A. Bendersky, M.A. Larotonda, J.P. Paz
  Phys. Rev. Lett. 107, 100502 (2011)

  2010 **Selective and efficient quantum process tomography with single photons**
  C.T. Schmiegelow, M.A. Larotonda, J.P. Paz
  Phys. Rev. Lett. 104, 123601 (2010)

- Proceedings.

  2010 **Ghost imaging and ghost diffraction with pseudo-thermal light generated by means of a programmable SLM**
  M. G. Capeluto, H Duisterwinkel, C. T. Schmiegelow, D. Francisco, S. Ledesma, C. Iemmi
  Journal of Physics: Conference Series 274 (2011) 012004

  2010 **Construccion y caracterización de un diodo laser estabilizado sintonizable** *F. Barabas,G. Petrungaro, C. T. Schmiegelow, J. Codnia*
  Anales AFA

  2009 **Fuente de pares de fotones entrelazados en polarización**.
  M.G. Mingolla, C.T. Schmiegelow, M.A. Larotonda
  Anales de la AFA.

  2008 **Generador cuántico de números aleatorios.**
  H. Benítez, L. Perez, C.T. Schmiegelow, M.G. Kovalsky, M.A. Larotonda, A.A. Hnilo.
  Anales de la AFA.

.

To describe ensembles of states which have been prepared in two random possibilities one does so by adding the respective density matrices of the pure stares weighted by the probabilities. For the example mentioned above, density matrix will then be $\rho = p\,|\psi_1\rangle\,\langle\psi_1| + (1-p)\,|\psi_2\rangle\,\langle\psi_2|$ or equivalently

$$\rho = p\rho_1 + (1-p)\rho_2 \tag{1.5}$$

It is interesting to note how this randomness is completely different from that which arises from measurement of a system superposition of the output outcomes. To do so one could consider the following example with two different states. One is described by the pure state $|\psi\rangle = (|0\rangle + |1\rangle)/\sqrt{2}$ and the other by a density matrix with equal probabilities of having the state $|0\rangle$ or $|1\rangle$. The results obtained in experiments performed in these two different set of states will be very different. In the first case there exist a basis, the $|\pm\rangle = (|0\rangle \pm |1\rangle)/\sqrt{2}$ basis, where if one performs a measurement one obtains a result with certainty (the eigenvalue corresponding to $|+\rangle$). In the second case, there is no basis where this happens. In fact, for this second case, it is not difficult to demonstrate that in any basis, the probability of obtaining any result is 1/2. The density matrices of each case are written in matrix form as:

$$\rho = \frac{|0\rangle + |1\rangle}{\sqrt{2}}\frac{\langle 0| + \langle 1|}{\sqrt{2}} = \frac{1}{2}\begin{pmatrix} 1 & 1 \\ 1 & 1 \end{pmatrix} \;\; ; \;\; \rho = \frac{1}{2}(|0\rangle\,\langle 0| + |1\rangle\,\langle 1|) = \frac{1}{2}\begin{pmatrix} 1 & 0 \\ 0 & 1 \end{pmatrix} \tag{1.6}$$

The off diagonal terms missing in the second case are called the coherence terms. They are responsible for most of the "strange" results of quantum systems. A system which is in a quantum superposition will have such terms, and a system which can be described as a random mixture of possibilities will not.

1.1.2 Composite systems and Partial trace.

Density matrices and non-pure (mixed) states also arise in the description of subsystems of larger systems. In fact, one could argue that when one says "a machine which randomly prepares ..." one actually is describing a larger system which in principle could be pure. By looking at just a part of it one sees a random mixture of possibilities which one must describe with a density matrix. Whether or not there is an ultimate quantum pure or mixed state and whether this quantum mechanical description of nature is complete is far beyond the scope of this thesis. However, the mathematics of composite systems is crucial in understanding decoherence and in describing noisy or imperfect quantum channels. (In playful manner people who think that one must always think mixed states as subsystems of pure states say they belong to the Church of the Larger Hilbert Space.)

The state of a composite system of many qubits is described as the tensor product of the states of each qubit. For example for two qubit subsystems described by the states $|\psi_a\rangle$ and $|\psi_b\rangle$, the common state of the system will be $|\psi_a\rangle \otimes |\psi_b\rangle$. It is common to compress notation omitting the tensor product symbol $|\psi_a\rangle\,|\psi_b\rangle$ and often also pushing all the labels into one ket symbol $|\psi_a, \psi_b\rangle$. The most general state

of these two qubits can be described by the vector which is the superposition of the states forming a basis for the whole composite system:

$$|\psi\rangle = \alpha\,|00\rangle + \beta\,|01\rangle + \gamma\,|10\rangle + \delta\,|11\rangle\,. \tag{1.7}$$

Where α, β, γ and δ can be any complex numbers fulfilling $|\alpha|^2 + |\beta|^2 + |\gamma|^2 + |\delta|^2 = 1$ so that the state is normalized.

The description of just one part of the system is done by taking the partial trace over the state space of the other part. Say one wants to describe only subsystem a, then one must make the partial trace over system b on the joint density matrix.

$$\rho_a = \mathsf{Tr}_b(\rho_{ab}) = \sum_i \langle b_i|\,\rho_{ab}\,|b_i\rangle \tag{1.8}$$

Where $\{\langle b_i|\}$ is a basis for system b. Analogously one has a symmetric definition for ρ_b for the subsystem b.

A clear example of a pure composite state which has a subsystem which must be described as a mixture of states is $|\psi\rangle = (|00\rangle + |11\rangle)/\sqrt{2}$. When taking the partial trace over one of the subsystems, say b, the result is exactly what was identified before as a mixed state $\rho_a = (|0\rangle\langle 0| + |1\rangle\langle 1|)/2$. This state can be understood as a mixed state due to a random preparation, as mentioned before, or due to the fact that it is actually a part of a pure state belonging to a larger system.

1.1.3 Entanglement

Composite states as just described above can be particularly intriguing. The state $|\psi\rangle = (|00\rangle + |11\rangle)/\sqrt{2}$, as well as many others, cannot be expressed just as a tensor product of the two subsystems. There is no basis in which one can do so: $|\psi\rangle \neq |\psi_a\rangle \otimes |\psi_b\rangle$. When a composite state can't be written as a tensor product and it must be written as a sum of tensor products it is called entangled.

Entangled states are responsible for another big set of "spooky" things predicted by quantum mechanics such as teleportation and the violation of Bell's inequalities[NC00, Bel87].

1.1.4 Quantum Processes

The evolution of a closed pure quantum system is described by a unitary operator $\hat{U}$ which connects the initial $|\psi\rangle$ and final $|\psi'\rangle$ states.

$$|\psi'\rangle = \hat{U}\,|\psi\rangle \tag{1.9}$$

The description of the evolution of a closed system which is described by a density matrix is then constructed as:

$$\rho' = \hat{U}\rho\hat{U}^\dagger \tag{1.10}$$

When the system is described by a time independent Hamiltonian H then the evolution operator takes the form $U = \exp\{-itH\}$. However this association is not necessarily the best way to go, any unitary operator is in principle a valid quantum evolution. In many cases one is not interested in knowing the underlining

Hamiltonian but, rather, in giving an accurate description of how a system evolves in a given circumstance. It is in the spirit of quantum information to talk about the evolution of system just as unitary evolutions with no reference to Hamiltonians but an emphasis on processes. Sometimes processes are even treated as gates. That is, one step evolutions with some control parameter which modifies its action but no reference to time. For example: the precession of the spin may be viewed as a rotation where the physical parameters describing the field are mapped into directions and angles of rotation: the time parameter is replaced by an angle parameter.

The evolution of open quantum systems requires a different more general description. In the case where the system and environment are initially in a product state $\rho_{tot} = \rho \otimes \rho_{env}$ then the output state of the system may be described as a map $\rho' = \mathcal{E}(\rho)$. This map is obtained by tracing over the environment variables $\mathcal{E}(\rho) = \mathsf{Tr}_{env}(U\rho \otimes \rho_{env}U^\dagger)$. In such a case the most general description of such an evolution can be written in an operator sum (or Kraus) representation.

$$\mathcal{E}(\rho) = \sum_k A_k \rho A_k^\dagger \tag{1.11}$$

If the channel is trace preserving then the A_k operators must satisfy the completeness relation $\sum_k A_k^\dagger A_k = I$.

Another more useful representation, specially in the context of quantum process tomography is the so called χ matrix representation[NC00]. The connection between the Kraus and the χ matrix representations can be established by by writing the operators A_k as linear combinations of E_i operators which form a basis for the operators. Then by writing $A_i = \sum_k e_{ia} E_a$ one can rewrite the process as

$$\mathcal{E}(\rho) = \sum_{ab} \chi_{ab} E_a \rho E_b^\dagger \tag{1.12}$$

The χ matrix must be positive and Hermitian and the completeness relationship then translates to $\sum_{ab} \chi_{ab} E_a E_b^\dagger = I$. For a Hilbert space of dimension D one needs D^2 operators to form a basis. The chi matrix has D^4 elements, but the necessary restrictions reduce this number by D^2. The total parameters characterizing a general channel are thus $D^4 - D^2$. Fully characterizing an arbitrary quantum channel is therefore necessarily an exponentially difficult task: as $D = 2^n$, it scales exponentially with the number n of qubis of the system. In such a situation a method as presented in this thesis, where one is able to selectively extract information about a channel without the need of knowing the full χ matrix, is of fundamental importance for it will make tomography of large qubit systems possible.

1.1.5 Decoherence

Decoherence is a mechanism by which a quantum system evolves in such a way that it goes from a pure to a mixed state. If a quantum system interacts with another one it may end up in a final state which is must be described as a mixture of quantum states and not a superposition. This might be particularly a problem if trying to implement quantum information algorithms which require the system to

remain in a pure state. Keeping quantum systems sufficiently isolated from their environment in order to suppress decoherence is one of the most difficult challenges facing quantum information processing.

A simple model for decoherence can be established by considering a system and an environment composed of one qubit each. The initial composite state is not entangled and the system is in a pure quantum superposition $|\psi(t=0)\rangle = (\alpha|0\rangle + \beta|1\rangle)|E(0)\rangle$. Then the whole system-environment evolves with the Hamiltonian:

$$H = |0\rangle\langle 0| \otimes \hat{O}_0 + |1\rangle\langle 1| \otimes \hat{O}_1. \tag{1.13}$$

Where $\hat{O}_i$ are operators acting over the environment. The system will then, after a time t, evolve to the state $|\psi(t)\rangle = \alpha|0\rangle|E_1(t)\rangle + \beta|1\rangle|E_2(t)\rangle$. By taking the partial trace over the environment one finds that the density matrix describing the system is:

$$\rho = \begin{pmatrix} |\alpha|^2 & \beta^*\alpha f(t) \\ \beta\alpha^* f^*(t) & |\beta|^2 \end{pmatrix}. \tag{1.14}$$

Where the function $f(t)$ depends on how the system-environment evolved. That is:

$$f(t) = \langle E_1(t)|E_0(t)\rangle \tag{1.15}$$

If the $|E_i(t)\rangle$ states evolve to be orthogonal the coherences vanish transforming the initial state of the system from a pure state into a statistical mixture. In many general cases, when the environment is large the system does, in fact, evolve into such mixed states[PZ02].

1.1.6 Pauli Matrices and Operators

Pauli matrices are used throughout this thesis. The three basic Pauli matrices are:

$$X = \begin{pmatrix} 0 & 1 \\ 1 & 0 \end{pmatrix} \;;\; Y = \begin{pmatrix} 0 & -i \\ i & 0 \end{pmatrix} \;;\; Z = \begin{pmatrix} 1 & 0 \\ 0 & -1 \end{pmatrix} \tag{1.16}$$

They are Hermitian and unitary, have eigenvalues ± 1 and they anticommute. Together with the identity I they form a basis of operators of for a state space of dimension 2 (i.e. for a qubit.)

Furthermore, generalized Pauli operators may be constructed for systems of various qubits. For example for a system of two qubits the Pauli operators are (omitting the $\otimes$ symbol): II, IX, IY, IZ, XI, XX, XY, XZ, YI, YX, YY, YZ, ZI, ZX, ZY, ZZ. Analogously operators for more qubits can be constructed. All operators constructed this way will also be Hermitian, unitary with eigenvalues ± 1 and will either commute or anti commute. Also they form a basis of a n qubit state space.

1.1.7 Mutually Unbiased Bases

Mutually unbiased bases (MUBs) are orthonormal bases whose states have no bias towards other states of the other mutually unbiased bases[BBRV08, LBZ02]. If a measurement is performed in one basis and then a subsequent measurement in

another MUB then of the possible outputs have equal probability. Information on the results of a measurement on one basis provides no bias as to which are the possible results in a subsequent measurement in another basis belonging to the MUBs.

The simplest example of MUBs are the bases of two dimensional systems formed by the eigenvectors of the Pauli operators X, Y and Z. As described in textbook examples of Stern-Gerlach experiments a measurement in one direction provides no information about a subsequent measurement in another one[Sak85].

In general two bases K and K' of a d-dimensional Hilbert space will be mutually unbiased iff their states labeled j and j' fulfill:

$$|\langle \psi_j^K | \psi_{j'}^{K'} \rangle|^2 = \frac{1}{d} \tag{1.17}$$

For Hilbert spaces whose dimension is a power of a prime there always exist $d+1$ MUBs[RBKSS05, LBZ02, GHW04]. Moreover for systems of many n qubits these $d+1 = 2^n + 1$ MUBs can be described efficiently[BBRV08, Dan05, Ben11].That is, both enumerating and constructing them can be done with resources that scale polynomially with the number of qubits.

Part I

Experimental Quantum Information with Photons

Chapter 2

Photons as Qubits

Among the very many possible physical supports for quantum information, photons play a very important role. Information can be stored in many of their degrees of freedom. Experiments have been done where polarization, path, momentum, frequency and orbital angular momentum are used as quantum registers (qubits or higher dimensional qudits). Bell inequalities and entanglement tests have been done successfully on these subspaces[ADR82, WJS+98, LJR+09, RT90, MQK+09]. Even hyper-entangled states where different degrees of freedom are in a non-product quantum state have been experimentally demonstrated[BCMDM05, BLPK05]. Photons can also travel long distances on optical fibers or on air providing a means to share quantum resources such as those needed for quantum key distribution and quantum teleportation[SMWF+07, SGG+02, WJS+98, BPM+97].

Photons also have some shortcomings for quantum information processing. They are difficult to generate on demand, they are difficult to store and interactions between them can only be done probabilistically. Moreover, it is very difficult to perform non demolition measurements on them.

In this thesis all experiments use qubits stored on the polarization and path of photons. That is, information is stored in an internal degree of freedom as well as in an external one. Path qubits are defined by the occupation of a pair of disjoint optical modes.

In this chapter the DiVicenzo criteria, which is a list of requirements a physical system must fulfill to be useful as a quantum device, is analyzed. Also comparison to some other systems is presented.

2.1 Requirements - DiVincenzo Criteria

To be useful for quantum computing a physical system must allow one to do several things. DiVincenzo came up with a list of requirements that became a popular way of analyzing how good a system is for quantum computing[DiV00]. Photons fulfill many of these characteristics very well but scalability still seems to be a difficult experimental task. Using DiVincenzo's criteria many of the general aspects of quantum computing with photons are discussed.

1. **System is comprised of well characterized qubits and allows for scalability.** Several well defined qubits can be used as quantum information

registers in photons. Using qubits encoded in the path of photons Knill, Laflamme and Milburn (KLM) have developed a scheme whereby one can perform efficient fault tolerant quantum computing[KLM01]. This scheme is based on linear optical elements such as beam splitters and phase shifters. It requires post-selection, that is, only considering as valid experiments whose results satisfy certain predefined conditions. KLM's scheme can also be mapped onto polarization photons [KMN+07].

2. **Ability to initialize the state of the qubits.** Scalably initializing qubits in photons is currently the mayor issue affecting the development of quantum computers with photons. Spontaneous parametric down conversion (SPDC) in nonlinear crystals is one of the most widely used sources of photons for quantum information but, as will be described in detail below (see 4.1), obtaining more than 4 photons can be achieved but is clearly not a scalable way to go. Other single photons sources such as Nitrogen vacancies in diamond [KMZW00] or Excitons in nano-structured semiconductors [MKB+00, KBKY99] are being intensively studied, but still none seem to fulfill the required characteristics needed to become a scalable solution to state initialization. Generation times and coherence properties of the initialized photons must be such that each pair of photons can show two photon interference in a beam splitter. As detailed in the next sections, this requires timings at the picosecond level and coherence lengths of at least a few microns.
Many experiments, as the ones presented in this thesis, which require little number of qubits can be very well achieved with photons generated by SPDC.

3. **System provides long coherence times, much longer than a gate operation time.** For photons gate times are much shorter than photonic qubit coherence times. Gates for photons are done with optical elements such as wave plates or beam-splitters. These are at the most a few centimeters big so gate times will be in the order of picoseconds. In normal lab conditions with flying photons coherence can be easily maintained over several meters, that is a few nanoseconds, some orders of magnitude more than gate time. With special care experiments where qubits stored in photons travel kilometers over fibers or with the use of telescopes without much loss of coherence have also been done[SMWF+07, SGG+02].
The main source of decoherence in photonic gates is imperfect mode matching and interferometric stability; Chapter 3 and Appendix D deal with interferometers and experimental issues related to obtaining little decoherence when working with photons.

4. **A universal set of gates is experimentally feasible.** Both for path and polarization qubits, a universal set of gates has been proven to work[EKW01]. Chapter 3 deals with the details of each case. However cascading these gates into larger processing devices using bulk optics seems very difficult; for example an experiment with about ten gates and a couple of photons can occupy a full medium sized (2.5x1.5m) optical table. Recently [PCR+08, CRO+11] some proof of principle experiments have been done on integrated optics which could solve all at once several issues holding the bulk optics experiments.

Integrated optics whereby photons travel in waveguides and interferometers engraved into centimeter sized chips can provide fast switching, good mode matching, interferometer stability and scalability.

5. **Qubit specific measurement capability.** Several technologies for detecting photons are available. The three main ones are photomultipliers[Ham], avalanche photo-diodes [Per] and superconductor junctions[Wikb]. Avalanche photodiodes are widely used because of several nice characteristics: they are available for wavelengths from $400nm$ to $1700nm$ [Exc], they can have efficiencies of more than 70%, their dark counts rates can be as low as $5\ counts/s$, and their are fairly easy to use. For example the industry standard models from Perkin Elmer require only a 5 volt power supply to work. Photomultipliers on the other side have lower efficiencies, higher dark counts and are not suitable for wavelengths much over $700nm$. Superconductor junctions have very good photon number resolving characteristics but still have low efficiencies and require cryogenic cooling.

2.2 Other physical implementations

Photonic qubits will probably not be the ultimate support for quantum information processing devices; mainly because of some scalability problems which are still not clear whether will be solved or not. However, they stand the best chance in quantum communication tasks. Their long coherence times and ease of transmitting them long distances in fiber optics or air cannot be matched by any other system.

Many other experimental approaches which use different physical systems are currently being heavily investigated. Research has focused both on the theoretical and experimental level. Here a brief review of some of the most relevant is presented.

- **Ion Traps**. Qubits stored in either electronic or magnetic levels of single ions are a very promising for mid-size quantum information processors. Gates are implemented via common mode oscillations and interactions to external laser or microwave fields. Currently experiments have been able to entangle up to 14 qubits in a fixed ion chain[MSB$^+$11]. Future experiments with structured ion traps might be able to expand this number which, in principle, setting technical difficulty aside, only seems to be limited by a competition between gate application time and coherence time. Also these kind of qubits are particularly well interfaced with photonic qubits[SCB$^+$11, PRS$^+$10, DM10].

- **Nuclear Magnetic Resonance**. Qubits stored in the magnetic orientation of nuclei of different atoms in simple molecules have been a good test bed for some of the first quantum information experiments[VC05]. Gates are implemented via radio frequency pulses which address individually or collectively different atoms. Together with the natural spin-spin interaction given by the position of the atoms in the molecules many quantum gates can be implemented. Scalability is a very big problem in such systems: finding the right molecule which allows for sufficient single qubit addressability as well as controlled interactions is an increasingly difficult task[Jon05].

- **Superconducting Junctions**. Qubits stored either in the charge, the flux or the phase of superconductor Josephson junctions have been extensively studied[MSS01]. The main difficulty in these kind of qubits is controlling decoherence: such junctions are solid state devices which even at cryogenic temperatures are difficult to correctly isolate. Also coupling these qubits is a difficult task. Non of these problems seem to have fundamental limitations. If they are resolved superconductor quantum have the benefit that, being solid state devices, they would allow easy scalability.

- **Other implementations**. Many other physical implementations of quantum information processing devices have been explored so far. A not complete list includes: quantum dots[LD98], Rydberg atoms[SWM10], coherent states of light[BvL05], optical frequency combs[MFP08], low pressure gases[HSP10], Bose-Einstein condensates[HMM03], optical lattices[BCJD99] and single neutral atoms in dipole traps[DeM02].

Chapter 3

Gates for Photons

For the experiments presented in this thesis two degrees of freedom (DOF) of photons were used: polarization and path. This chapter reviews the main gates available for each of these degrees of freedom and between them. Both theoretical and experimental aspects are analyzed. All the gates used in the experiments of this thesis are described in detail. Furthermore an original extension to a known two photon gate is presented.

The choice of these two degrees of freedom is mainly because of the availability of a complete set of tools to manipulate these states. Arbitrary unitary operations as well as controlled operations on each and between these DOF of a same photon can be achieved in a deterministic manner. Controlled gates between different photons can also be done but only probabilistically and therefore require post-selection.

3.1 Single Qubit Gates

3.1.1 Polarization

Polarization at the single photon level behaves the same way as with intense beams. In that sense, the mathematics used to describe classical waves can be mapped into field modes. The polarization of an electromagnetic wave traveling in the z direction is described by the vector $e_x\hat{x} + e_y\hat{y}$ while the polarization of each photon in that wave is described by the state $(e_x\hat{a}_x^\dagger + e_y\hat{a}_y^\dagger)\,|0\rangle$, where $\hat{a}^\dagger, \hat{a}$ are the field mode creation and destruction operators, $|0\rangle$ is the vacuum state of the electromagnetic field and the state is normalized when $|e_x|^2 + |e_y|^2 = 1$.

As polarization qubits we use this degree of freedom of photons. We will call horizontal $|H\rangle$ and vertical $|V\rangle$ polarized states (or photons) states which have linear polarization in those directions with respect to the lab. If the x axis lies in the horizontal direction and the y in the vertical the six states H, V, D, A, R, L are defined as shown in table 3.1.

As described in Chapter 1, these 6 states form a set of 3 mutually unbiased bases for a Hilbert space of dimension 2. They are extensively used in many quantum information and computation tasks. It is also usual to do the mapping $|H\rangle \equiv |0\rangle$ and $|V\rangle \equiv |1\rangle$ to define a computational or logical basis. This mapping also defines the relation between the Bloch sphere, normally used in quantum information to represent 2 dimensional states, with the Poincare sphere, normally

Name	Label State	Physical State	Logical State
Horizontal	$\|H\rangle$	$\hat{a}_x^\dagger \|0\rangle$	$\|0\rangle$
Vertical	$\|V\rangle$	$\hat{a}_y^\dagger \|0\rangle$	$\|1\rangle$
Diagonal	$\|D\rangle$	$(\hat{a}_x^\dagger + \hat{a}_y^\dagger) \|0\rangle /\sqrt{2}$	$(\|0\rangle + \|1\rangle)/\sqrt{2}$
Antidiagonal	$\|A\rangle$	$(\hat{a}_x^\dagger - \hat{a}_y^\dagger) \|0\rangle /\sqrt{2}$	$(\|0\rangle - \|1\rangle)/\sqrt{2}$
Circular Right	$\|R\rangle$	$(\hat{a}_x^\dagger + i\hat{a}_y^\dagger) \|0\rangle /\sqrt{2}$	$(\|0\rangle + i\|1\rangle)/\sqrt{2}$
Circular Left	$\|L\rangle$	$(\hat{a}_x^\dagger - i\hat{a}_y^\dagger) \|0\rangle /\sqrt{2}$	$(\|0\rangle - i\|1\rangle)/\sqrt{2}$

Table 3.1: Labelling of polarization qubit states.

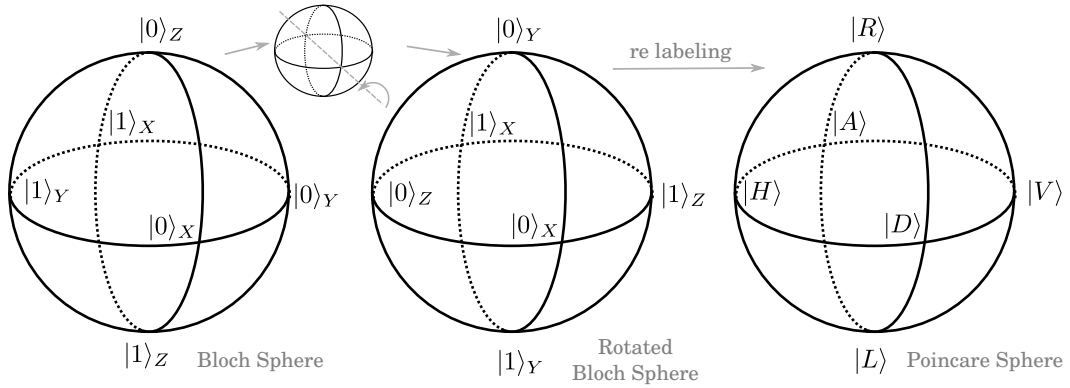

Figure 3.1: **Bloch-Poincare spheres relationship.** As depicted in the images the connection between the Bloch and Poincare spheres is trivial. Some confusion sometimes arises do to the fact that they are usually presented rotated with respect to each other.

used in optics to describe the polarization of light. As shown in Figure 3.1 one is simply a rotation of the other one.

Polarization can be controlled with several techniques. Most of them use birefringent materials to induce phase shifts in one axis with respect to the other one. Wave plates made out of quartz are ideal for this purpose: they are easy to set up and control, are relatively cheap and work well with light of low coherence as will be detailed below.

Other techniques such as electrooptic crystals such as Pockels cells or materials which present magnetooptic effects such as the Faraday effect can be used to control polarization, but in the experiments presented here none of them was used.

Wave plates.

The propagation of photons through linear media can be described by the wave solution $(e_x\hat{a}_x^\dagger + e_y\hat{a}_y^\dagger)e^{i(kz-\omega t)} |0\rangle$ where $k = 2n\pi/\lambda$ and n is the index of refraction of the medium and ω and λ are the frequency and wavelength of the wave in vacuum. If a material is birefringent then its index of refraction depends on the direction. (Quartz is very widely used as a birefringent material for wave plates. Although

many other materials present larger birefringence quartz has very good optical quality and is very strong and easy to produce.) After going thorough a crystal of length Δz and indices of refraction n_x and n_y the polarization gets transformed as (neglecting the time dependence):

$$(e_x\hat{a}_x^\dagger + e_y\hat{a}_y^\dagger)\,|0\rangle \rightarrow (e_x\hat{a}_x^\dagger e^{ik_x\Delta z} + e_y\hat{a}_y^\dagger e^{ik_y\Delta z})\,|0\rangle \tag{3.1}$$

This way, wave plates can be chosen to impinge a desired relative phase ϕ between the two polarization components by selecting the correct Δz such that $\phi = (k_x - k_y)\Delta z \mod (2\pi)$. Then the state after the wave plate is:

$$e^{ik_y\Delta z}(e_x\hat{a}_x^\dagger e^{\phi} + e_y\hat{a}_y^\dagger)\,|0\rangle \tag{3.2}$$

A global phase is also added when going through a wave plate. This is not a problem for global phases play no role in the results of experiments in quantum mechanics. Anyway, when other degrees of freedom are involved what was a global phase for polarization might not be global anymore. This must me taken into account, but does not pose any serious problem. This issues are detailed in Section 3.2.

Wave plates are normally manufactured with two fixed retardations and are called half wave plate (HWP) when $\phi = \pi$ and quarter wave plate (QWP) when $\phi = \pi/2$. (Retardation depends on the wavelength so wave plates work only as proper HWP or QWP when used at the designed wavelength.)

Zero order wave plates.

If a plate of quartz is cut thick enough not to break with normal handling, say $2mm$, then its retardation ϕ will be many times 2π. In particular, for light of $810nm$ the difference in indices of refraction is $n_x - n_y \approx 0.009$ so that the total retardation would be of $\phi \approx 2\pi \times 30$. This could be a potential problem if the coherence length of the photons is less than $30 \times \lambda \approx 18\mu m$. In such a case the wave plate would not only dephase one field component with respect to the other but it will make them loose coherence.

Fortunately this problem can be solved either with *zero* or *true-zero* order wave plates. Zero order wave plates are constructed the following way: two equal plates are cemented with their optical axes at 90° with respect to each other, then one of the plates is polished until exactly the right amount of material is removed such that in combination both wave plates do a retardation of exactly π or $\pi/2$. True-zero order wave plates on the other hand are made by gluing a very thin layer of quartz over a glass substrate (with no birefingence) and polishing the quartz so that is thin enough to provide exact π or $\pi/2$ retardation.

The experiments presented in this thesis always used either zero or true-zero order wave plates. This was necessary because the coherence length of the photons used throughout were always in the order of $10\mu m$ or less (see Section 4.1). All wave plates were anti-reflexion coated for the working wavelengths. Most wave plates were bought at Casix (www.casix.com) and some others from Thorlabs (www.thorlabs.com).

HWP and QWP rotation matrices.

If the axes defining the birefringence of a wave plate are aligned with the H,V directions then an incoming photon in the normalized state $\alpha|H\rangle + \beta|V\rangle$ will be transformed as outlined above. In particular for HWP and QWP one has:

$$\alpha|H\rangle + \beta|V\rangle \xrightarrow{HWP} \alpha|H\rangle - \beta|V\rangle \tag{3.3}$$

$$\alpha|H\rangle + \beta|V\rangle \xrightarrow{QWP} \alpha|H\rangle + i\beta|V\rangle \tag{3.4}$$

These are in fact rotations about the $H(Z)$ axis of the Poincare (Bloch) sphere. For the HWP the rotation is of π while for the QWP the rotation is of $\pi/2$. A careful analysis shows that when setting a wave plate at an angle θ with respect to the H axis then its action is also a rotation of the same amount but with respect to another axis. The rotation axis always lies in the equatorial plane of the Poincare sphere and it will form an angle of 2θ with respect to the H direction.

By associating the Z, X, Y directions with the polarizations H-V, D-A, L-R respectively and taking into account the above considerations the rotation matrices can be constructed in a straight forward manner. One must use the fact that a rotation of a two dimensional state of an angle Θ around an axis $\hat{n}$ is represented in the computational basis as

$$R_{\hat{n}}(\Theta) = \cos\left(\frac{\Theta}{2}\right) I - i \sin\left(\frac{\Theta}{2}\right)(n_x X + n_y Y + n_z Z) \tag{3.5}$$

The matrix for the HWP, whose axis is rotated at an angle θ from horizontal direction, is constructed by realizing it will rotate the polarization in $\Theta = \pi$ around a vector which makes an angle of 2θ with the Z axis and which lies in the linear polarization plane (Z, X) (see Figure 3.2), that is:

$$\begin{aligned} H_\theta &= \cos(\pi/2) I - i \sin(\pi/2)[\cos(2\theta) Z + \sin(2\theta) X] \\ &= -i \begin{pmatrix} \cos(2\theta) & \sin(2\theta) \\ \sin(2\theta) & -\cos(2\theta) \end{pmatrix} \end{aligned} \tag{3.6}$$

The QWP is acts in the same manner but rotates only an angle of $\Theta = \pi/2$. One then has:

$$\begin{aligned} Q_\theta &= \cos(\pi/4) I - i \sin(\pi/4)[\cos(2\theta) Z + \sin(2\theta) X] \\ &= \frac{1}{\sqrt{2}} \left(\mathbf{I} - i \begin{pmatrix} \cos(2\theta) & \sin(2\theta) \\ \sin(2\theta) & \cos(2\theta) \end{pmatrix} \right) \end{aligned} \tag{3.7}$$

Visualizing wave plates in the Poincare sphere.

It is very useful to have a visual representation of rotations. It allows one to understand in a fast and comprehensive manner the action of one or many wave plates in sequence, it is a powerful tool for trouble shooting in the lab and it leads to nice graphical demonstrations which are otherwise cumbersome (as will be shown below).

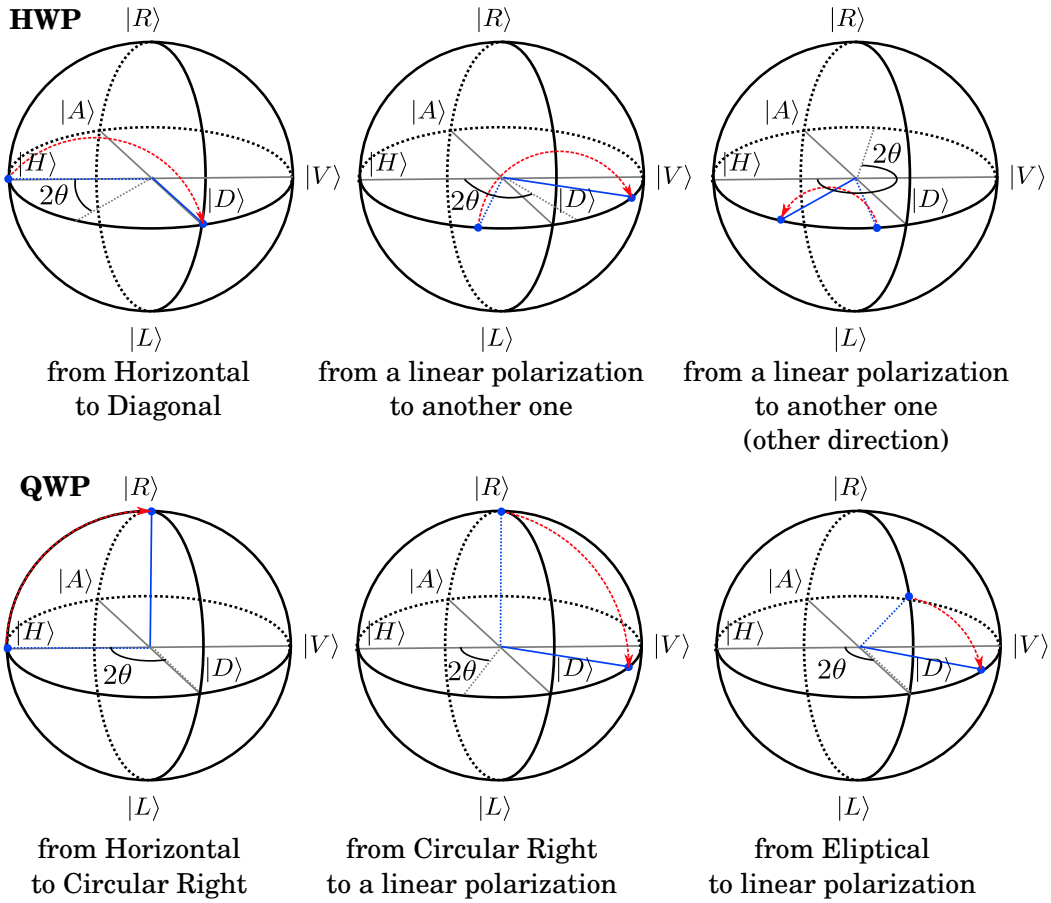

Figure 3.2: **Rotations in the Poincare sphere.** The images show many rotations in the Poincare sphere which might help to build intuition on how HWP and QWP act. The top row shows the action of a HWP at different angles on four different states and the bottom one shows the action of a QWP at other angles on other states. The initial and final states are shown in blue; dashed for initial, solid for final. The red dashed arrow shows the change in the state vector. The dashed gray arrow shows the rotation axis.

Both half and quarter wave plates rotate a state vector over its state space by a fixed amount. The angle of the wave plate with respect to the components of the incoming beam determines the axis of rotation. As described above, this axis always lies on the equatorial plane of the Poincare sphere, that is, the plane which contains the linear porlarizations H, V, A, D.

Figure 3.2 shows a few rotations which are a good aid to getting used to how HWP and QWP act on the Poincare sphere. Naturally, the effect of these gates on non pure states is the same as with pure states but with state vectors which lie on a surface of smaller radius[NC00].

If wave plates are zero or true zero order then they will induce no appreciable decoherence and the above description will adequately model them. This is the case in all experiments presented in this thesis. Anyway, if that was not the case

then the unitary operators H_θ and Q_θ would have to be replaced by a map which would describe adequately its evolution by including the necessary dephasing.

Arbitrary rotation gates with wave plates.

A combination of QWP, HWP and QWP, in that order, can be set to do any rotation operation on the polarization qubit. This is equivalent to saying that a combination of angles for these three wave plates can be chosen so that any pure state can be mapped into any other pure state. With this in mind it is not difficult to see how this combination of plates can be set to do any rotation.

The demonstration comes out directly if the states are charecterized by their latitudes $t_{i/f}$ and longitudes $g_{i/f}$ as shown in Figure 3.3. An example of how this mapping comes arround is exemplified in Figure 3.4. Any state can be mapped into another by following these steps:

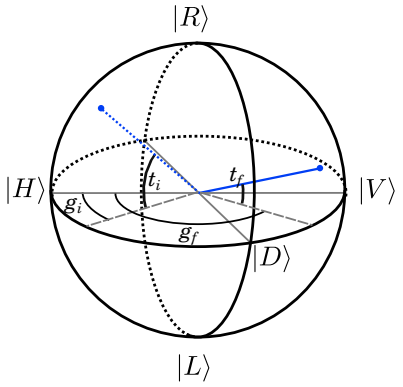

Figure 3.3: Labeling of initial and final states in the Poincare sphere according to their latitudes and longitudes.

1. Set the first QWP at an angle "below" the initial state. That is setting $2\theta = g_i$. This way the initial state is converted into a state with only linear polarization, i.e. the state is rotated into the equatorial plane. (If the initial state was already in the equatorial plane this step does nothing.)
2. Set the angle of the HWP to $2\theta = (g_f - t_f + g_i + t_i)$. This way the state is mapped into another one with linear polarization at longitude $g_f - t_f$.
3. Set the angle of the last QWP to g_f. This way the state will be rotated to the final coordinates (g_f, t_f).

Alternatively one may demonstrate the above in a more analytic fashion, as presented by Englert et. al. in [EKW01]. The combination of the three wave plates at the angles α, β, γ can be written, after some manipulation, as:

$$\begin{aligned} Q_\gamma H_\beta Q_\gamma &= e^{-i(\gamma+3\pi/4)X} e^{i(\alpha-2\beta+\gamma)Z} e^{i(\alpha-\pi/4)X} \\ &= R_X(\theta_3) R_Y(\theta_2) R_X(\theta_1) \end{aligned} \tag{3.8}$$

Then the overall rotation can be written as general Euler rotation with three independent angles θ_i at the directions X, Y and X again. This constitutes an arbitrary rotation for a qubit. Actually, a global phase is missing, but that poses no restrictions as mentioned above and detailed later.

The above constitutes only a demonstration that any rotation can be done with a combination of quarter-half-quarter wave plates but does not provide a way of finding those angles given a certain unitary. To do so, Octave/Matlab code was developed to find the right angles for the wave plates given any unitary as an input.

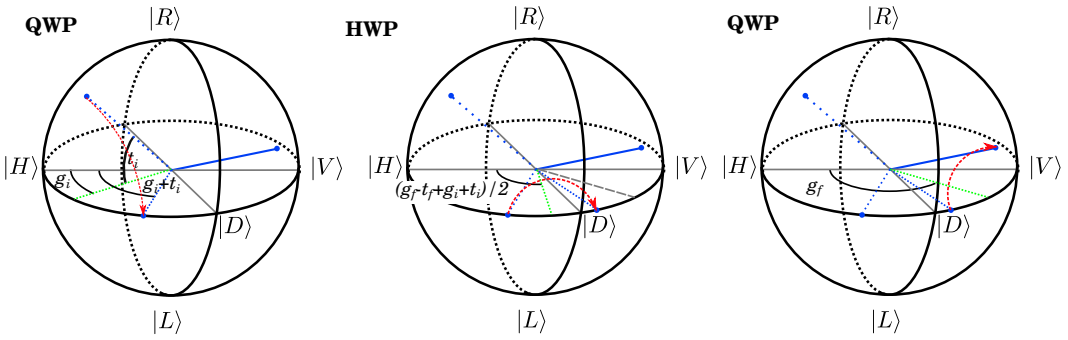

Figure 3.4: **Universal rotations for polarization qubits.** Any state can be mapped into any other by a combination of a quarter, half and quarter wave plates. This example shows the procedure for a specific case by its representation in the Poincare sphere. Blue lines show the states at the intermediate (dashed) and final (solid) states. Green dashed lines show the angle of the wave plate at each stage.

Reflections

Reflections at mirrors also modify the polarization of the beam. In normal metallic mirrors the effect is just to invert the Horizontal component adding to it a π (-1) phase. In matrix form this is represented as:

$$R = \begin{pmatrix} -1 & 0 \\ 0 & 1 \end{pmatrix} \tag{3.9}$$

This is true as long as reflections are exactly on the horizontal plane. A reflection on another plane adds the same phase but not in the H component of the beam but in the reflection plane. These two must be correctly matched so as to do just a phase change of π (-1) in the H component. Very strict care must be taken when aligning experiments with many reflections. An angular missalignment as small as one degree can add up in consecutive reflections scrambling the polarization in an undesired way.

If dielectric mirrors are used then the phase acquired in the reflection might be different. Most dielectric mirrors imping a $\pi/2$ (i) phase in the horizontal component instead of the -1 characteristic of metallic mirrors. In the experiments of this thesis we used only metallic mirrors.

3.1.2 Path

Photons can travel in different spatial modes. Many different approaches to storing qubits, qudits or continuous variables in the different sets of these modes have been explored. For example, storing qubits or qudits in orthogonal states corresponding to different orbital angular momentum of photons has been explored at the single photon regime[MVWZ01] with many different experimental techniques[LVN+09]. Also much research has been done on the x-k continuous variable describing the wave front by transforming one onto the other by lens systems[TGT+11, WMPR10].

Name	Physical State	Logical State
Path A	$\hat{a}_a^\dagger \left\|0\right\rangle$	$\left\|0\right\rangle$
Path B	$\hat{a}_b^\dagger \left\|0\right\rangle$	$\left\|1\right\rangle$
–	$(\hat{a}_a^\dagger + \hat{a}_b^\dagger) \left\|0\right\rangle / \sqrt{2}$	$(\left\|0\right\rangle + \left\|1\right\rangle)/\sqrt{2}$
–	$(\hat{a}_a^\dagger - \hat{a}_b^\dagger) \left\|0\right\rangle / \sqrt{2}$	$(\left\|0\right\rangle - \left\|1\right\rangle)/\sqrt{2}$
–	$(\hat{a}_a^\dagger + i\hat{a}_b^\dagger) \left\|0\right\rangle / \sqrt{2}$	$(\left\|0\right\rangle + i\left\|1\right\rangle)/\sqrt{2}$
–	$(\hat{a}_a^\dagger - i\hat{a}_b^\dagger) \left\|0\right\rangle / \sqrt{2}$	$(\left\|0\right\rangle - i\left\|1\right\rangle)/\sqrt{2}$

Table 3.2: Labelling of path qubit states.

Another option, which was used throughout this thesis, consists on the discretization of two possible Gaussian modes on which a photon can travel. That is, whether a photon is travelling through one or another disjoint paths. This qubit has been called Path, Path-Momentum, or Dual-Rail and it presents lots of advantages for the experiments presented here.

The correspondence between the physical states and the logic states is done in a similar fashion as in with the polarization case. Now we define the single photon creation operators $\hat{a}_{a/b}^\dagger$ which create a photon in a Gaussian spatial mode labelled a or b. One must choose a and b such that they will be two disjoint paths (i.e. with negligible overlap). The photon will either be traveling on one of these paths, on the other one or on an arbitrary superposition of both. Such a superposition state can be written as $(\alpha\hat{a}_a^\dagger + \beta\hat{a}_b^\dagger)\left|0\right\rangle$; here, again, $\left|0\right\rangle$ is the vacuum state of the electromagnetic field and $|\alpha|^2 + |\beta|^2 = 1$ ensures normalization. Correspondingly the table linking physical states and logical states is given in table 3.1.2.

Here, in contrast with the polarization case, many of the names are nonexistent and there is no "Label State" but this is just a question of nomenclature. Anyway, even for path qubits, it is sometimes useful to use the same H,V,D,A,R,L in analogy with the polarization states.

Path qubit control can be achieved in several manners. Maintaining coherence is, though, trickier than in the polarization case. Here the states defining the qubits are in spatially different locations and need to be combined in controlled interferometers to rotate them. As will be described in the next subsections, to see proper interference, one must take adequate care of mode matching as well as interferometric stability to do coherent rotations on Path qubits.

Phase Retarders and Beam-splitters.

The two basic building blocks needed to control path qubits are phase retarders and beam splitters. The actual way to implement these vary from experiment to experiment depending on convenience.

Consider a photon travelling one spatial mode, say a. Its state is then described by the wave vector $\hat{a}_a^\dagger \left|0\right\rangle$, see Figure 3.5. On its path it encounters a semi-reflecting surface, i.e. a beam-splitter. It will get transmitted and reflected with a certain probability. Also an additional phase may appear on the reflected beam. The state at the output of the beam splitter will be of the kind $(\alpha\hat{a}_a^\dagger + \beta\hat{a}_b^\dagger)\left|0\right\rangle$ where α and

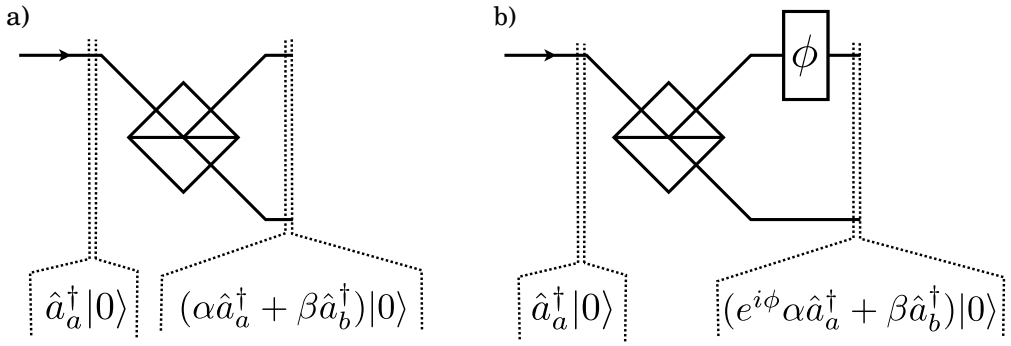

Figure 3.5: **Path qubits.** In a) the action of a general beam-splitter on only one of the input modes is shown. The top mode is the one labeled a and the bottom one b. In b) a phase is added to the top a mode with a phase retarder.

β depend on the characteristics of the beam-splitter used. It may seem that one would need a special beam-splitter for each different mode transformation one ones to do. Fortunately this is not the case. As will be shown below, with a combination of 50:50 beam splitters and phase retarders, one can do arbitrary rotations on the path qubits.

A 50:50 beam-splitter is a beam splitter that will transmit and reflect light equally. Its operation on the logical states can be described by the matrix:

$$BS = \frac{1}{\sqrt{2}} \begin{pmatrix} 1 & i \\ i & 1 \end{pmatrix} \tag{3.10}$$

The relative output phase here is chosen symmetric but in principle depends on the kind of beam-splitter used. For example a cube beam-splitter, where reflection occurs in a dielectric layered surface sandwiched between two prisms, will behave very differently to a plate beam-splitter where reflection takes place at a semi-silvered surface of a glass or quartz plate (see Figure 3.6). However this overall phase is always finally controlled by subsequent phase retarders so the exact knowledge of the real relative phase after a beam-splitters is not normally necessary.

Phase retarders can be implemented in several ways: electrooptic crystals, prisms, glass plates, mirrors on piezoelectric mounts etc. A phase retardation is just an optical element which will make one optical path longer than the other one, thus adding a phase shift ϕ proportional to the difference in paths Δd. The scaling is given by the wavelength of the photon and the index of refraction n of the retarder so that $\phi = 2\pi n \Delta d/\lambda$. This is understood purely from the wave nature of photons. In fact, the description presented here is just the single photon analogue of classical light interferometry.

A general phase retarder operates on the logic states as the matrix proportional to a rotation in Z.

$$P_\phi = \begin{pmatrix} 1 & 0 \\ 0 & e^{i\phi} \end{pmatrix} \tag{3.11}$$

To complete the picture of how path qubits work lets consider the arrange of optical elements shown in Figure 3.7 a). First beam-splitter, then a phase retarder

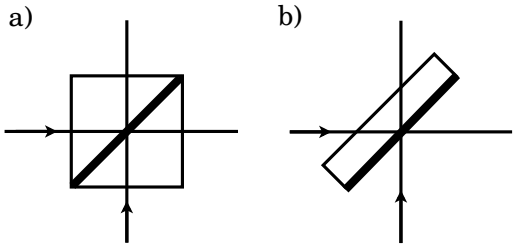

Figure 3.6: **Different beam splitters.** A cube beam-splitter a) and a plate beam splitter b). In a) the beams cross at a dielectric surface sandwiched between two equal pieces of glass, quartz or other optical material. In b) beams cross at a semi silvered surface, one of them arriving from air the other from the optical substrate. Although in principle both kinds of beam splitters could be made with wither semi silvered surfaces or dielectric coatings generally this is not the case.

and last another beam-splitter. Interference at the second beam-splitter will make the outcome depend on the phase set in the phase retarder. The interesting thing is that the transformation ends up being just a rotation in Y with a global phase.

$$VBS_\phi = BS.P_\phi.BS^{-1} \quad = \quad e^{i\phi/2} \begin{pmatrix} \cos(\phi/2) & -\sin(\phi/2) \\ \sin(\phi/2) & \cos(\phi/2) \end{pmatrix} \tag{3.12}$$

By checking its effect on the input states $|0\rangle$ or $|1\rangle$, this transformation can also be understood as a variable beam-splitter. In this way, a combination of two beam-splitters and a phase retarder act on an arbitrary input as a tunable beam-splitter whose reflectivity is controlled by the phase retardation. This combination of optical elements is called a Mach-Zehnder interferometer.

Arbitrary unitary gates with 50:50 beam splitters and phase retarders.

The above gives clear insight on how to construct an arbitrary rotation using beams splitters and phase retarders. As shown in Figure 3.7 b), using a combination of a phase retarder, a Mach-Zehnder interferometer and a final phase retarder an arbitrary rotation can be made. This is straight forward to see by noting that the the composition of elements combine consecutive rotations in the Z, Y, Z logical axes. Then they constitute a set of Euler angles that can perform any rotation. The first phase retarder does a Z rotation, the combination of beam-splitters sandwiching a phase retarder do a Y rotation followed by a final phase plate which performs a Z rotation.

Phase plates.

As phase retarders in all the experiments we used thin glass plates mounted on goniometers. We used $1mm$ thick microscope slides as shown in Figure 3.8. This choice was made for several reasons: a) these phase retarders are small and can be fitted into different interferometers; b) they are easy to construct and are fairly robust and c) they do not misalign beams notably when inserted and rotated. This

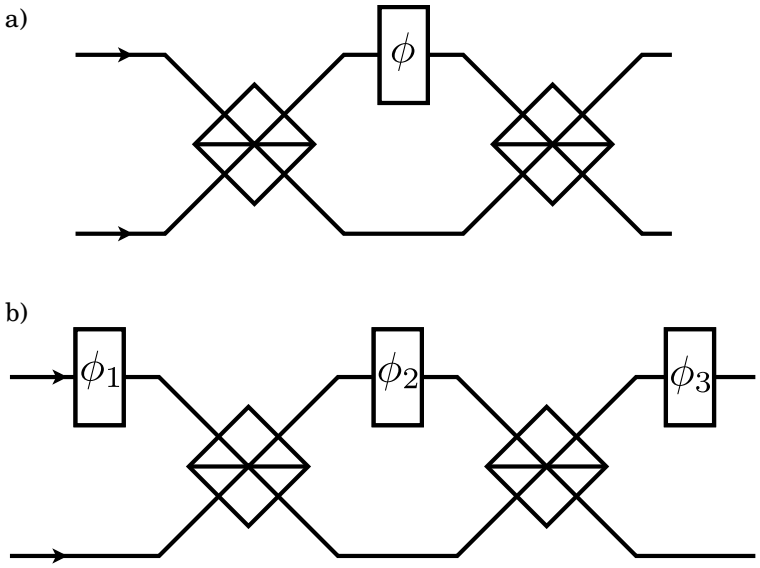

Figure 3.7: **Universal path qubit gates.** Subfigure a) shows a Mach-Zehnder interferometer which acts as a rotation in the logical Y axes of an angle controlled by the phase retarder. Subfigure b) shows how a general rotation of the path qubit can be implemented with a combination of a Mach-Zehnder interferometer and two phase retarders.

last feature was the most important in discarding wedge prisms which are normally used in Mach-Zehnder interferometers.

On the negative side, phase plates constructed this way are a bit tricky to calibrate for the angle of rotation is not linearly related to the phase impinged on the path. Although calibration could be done by calculating the optical path as a function of the angle, this wasn't needed in our experiments. We only needed to set some fixed phases ($0, \pi/4, \pi/2, \pi, \cdots$); these phases can be calibrated easily before starting the experiments by looking at the outputs for maximums, minimums, and balance.

Calibrations were done before staring the experiments and checked every couple of hours. Calibrations were recorded on a fixed ruler by measuring the position of the reflection of an auxiliary red laser pointer on the glass plate. The ruler was placed at a distance of $0.5m$ so as to control the angle with precision $\approx 0.1^\circ$ seen as a displacement of the beam of $1mm$. With such a configuration a π phase shift corresponded to about $2cm$ displacement in the calibration ruler.

Interferometer stability

The trouble with working with path qubits is that relative path lengths must remain stable within a few nanometers. If they don't then the relative phase between the states represented by each paths will also change. Thermal fluctuations and mechanical vibrations cause relative paths to change randomizing the phase and thus producing unwanted decoherence. On a $10cm$-arm Mach-Zehnder interferometer thermal fluctuations can make a π-shift in less than a minute. Mechanical

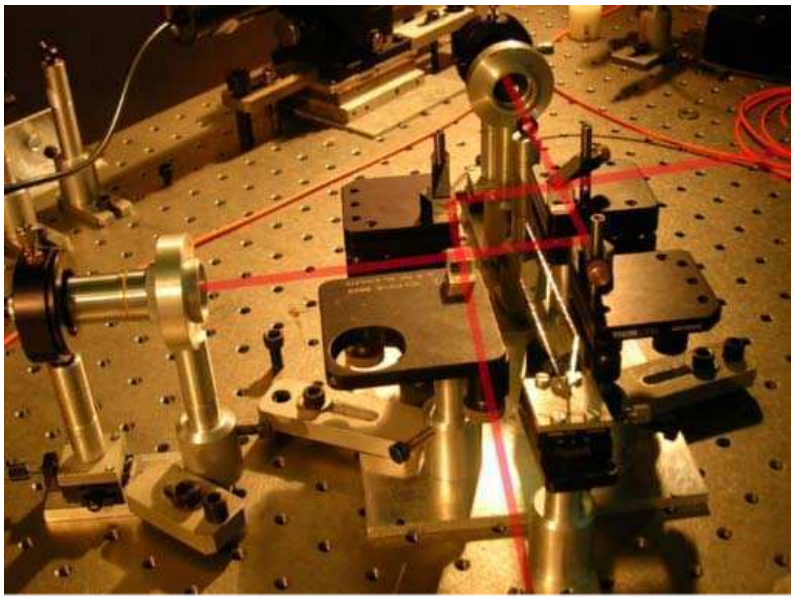

Figure 3.8: **A Mach-Zehnder interferometer.** The relative phase retardation of the arms is controlled by tilting a thin glass plate. This particular interferometer uses penta-prisms instead of mirrors on both arms. Though it is easier to align and balance it was not used in our experiments because it is not easy to actively stabilize.

vibrations can have frequencies of on the range of a few Hz to a couple of kHz. These two main sources of instability must be very stringently controlled to have stable interferometers with which one can perform quantum information tasks.

Mechanical vibrations can be reduced below an appreciable level by sturdy robust construction and placement of optical elements on a stabilized optical table. Thermal fluctuations are a bit trickier; temperature stabilization of the room helps but does not solve the problem completely for air flow and human presence is enough to produce enough temperature imbalance so as to observe a path change.

Two approaches were to solve the temperature fluctuation problem. When we could, we used a special type of interferometer called Sagnac interferometer which is “self stabilized”. When the Sagnac configuration was not possible the approach was to do active stabilization of the interferometer to compensate for thermal fluctuations.

A Sagnac interferometer can be thought as a folded Mach-Zehnder interferometer; Figure 3.9 illustrates this. This interferometer is stable because both beams go through the same path, so if it changes for one it changes for the other one too. Anyhow, an interferometer like this is of no use, because there is no way to control the relative phase of the paths either. A slight modification does the trick, by displacing one of the paths sideways one can separate them, and thus introduce a phase plate in only one of the paths. This way, although the paths are not exactly the same, they are very close and still hit the same optical element so changes due to thermal fluctuations are minimal. An interferometer like this can stay stable several hours without changing its output.

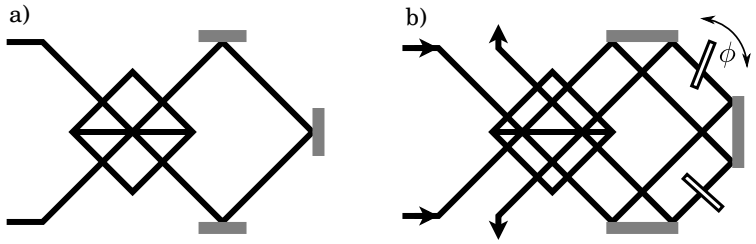

Figure 3.9: **Sagnac interferometers.** They are stable against thermal fluctuations. Only the second one b) was used. Two phase retarders are used so that both paths are equal in length. This is crucial when using low coherence light.

For Mach-Zehnder interferometers we used active stabilization. By inserting a reference beam parallel to the photons paths, but with higher intensity and displaced upwards (or sideways), a reference signal was monitored on a photodiode. This signal was used to control a feedback loop with proportional and integrator stages (PI-loop) with two methods: sider-fringe and lock-in.

In the sider-fringe method the stabilization is done by comparing the input signal with a reference set voltage. The interferometer was maintained stable by acting on the piezoelectric which displaced the mirror by an amount that was proportional to the difference between the set voltage and the one read on the reference photodiode. The details of the circuit are presented in Appendix D.1. This method is fairly easy to implement but is sensitive to power fluctuations of the reference beam. This was particularly a problem when wave plates introduced in the interferometer changed unwillingly the response of the error signal.

To solve the problem of sider-fringe stabilization we adopted a lock-in method. Again, the details of the circuits used are presented in Appendix D.2. A small modulation was introduced on the piezoelectric disk at a frequency of about $2kHz$. Then a circuit compared the relative phases of the excitation signal and the response. This is equivalent to taking the derivative of the error signal. In this way it is therefore possible to lock the interferometer to a maximum or a minimum, which is seen as a zero in the phase sensitive signal. This kind of lock does not depend on the overall power in the locking beam an is thus more robust to intensity fluctuations.

Interferometer visibility

Having a good interference signal in an interferometer is crucial to our experiments. The visibility of the interferometer limits how good gates can be implemented. Visibility is mainly limited by: mode matching, coherence, and beamsplitter reflectivity.

Correct mode matching requires that both beams at the exit of the beam splitter are perfectly superimposed. This occurs when their divergences match and when they are perfectly parallel. If this is not the case either fringes or rings are seen. Maintaining our interferometers in this “zero fringe” state required alignment checking every hour or so. To improve mode matching we also filtered our

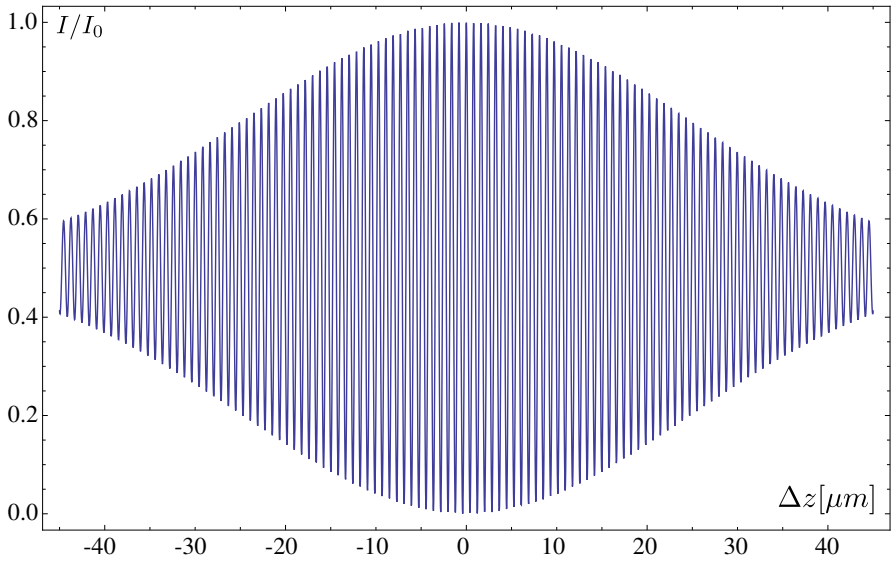

Figure 3.10: **Interference signal as a function of arm displacement.** Due to the finite coherence of the photons the visibility is reduced for differences in path of the order of the coherence length.

photon modes using single mode fibers in different stages.

The visibility is a very useful measure of how well balanced an interferometer is. It is normally defined as in terms of the maximum and minimum intensities as:

$$\mathcal{V} = \frac{I_{max} - I_{min}}{I_{max} + I_{min}}. \tag{3.13}$$

In our experiments, photons had very short coherence lengths $\Delta l \approx 60\mu m$. These are determined by the spectral filtering at the detection (see Chapter 4). In our experiments we had about $\Delta\lambda \approx 10nm$ and $\lambda \approx 810nm$. This way, as just stated, the coherence length is obtained as:

$$\Delta l \sim \frac{\lambda^2}{\Delta\lambda} \approx 60\mu m. \tag{3.14}$$

To observe interference the length difference between the two arms interferometers must be shorter than this. Figure 3.10 shows the expected interference signal for parameters just mentioned. It is seen that beyond the coherence length there is almost no interference left. In fact to use interferometers as quantum gates we will require they have high visibilities. This will allow applying the necessary gates with good fidelity. In fact we aimed at visibilities above 95%. This set the limit for the difference in the two arms to be set no further away from their equal length than $\approx 10um$. To balance interferometers with this precision we used probe light from a powerful (up to $2W$) laser diode which we could tune in coherence length by tuning the power near the threshold. This was beneficial in two senses. We could start with coherence lengths of a couple of millimeters and adjust the interferometer to equal lengths while reducing the coherence of the laser. In this regime the power of the laser was of a few milliwatts. We could also do this readjusting in

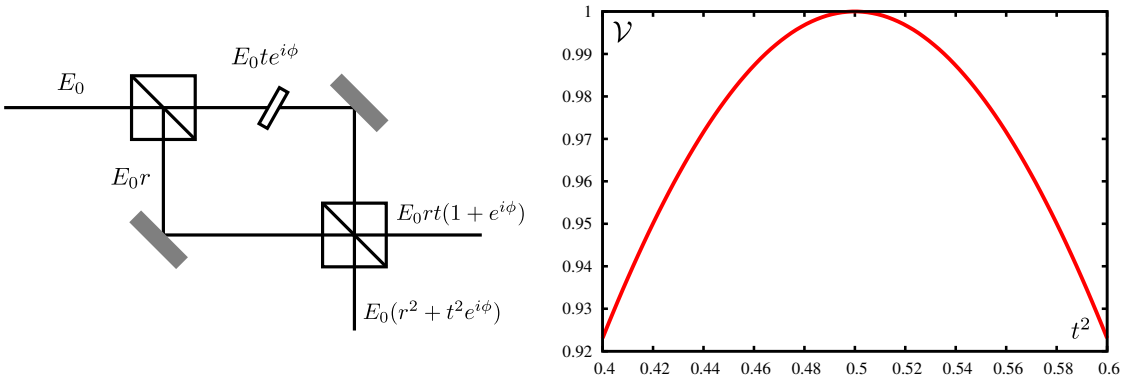

Figure 3.11: Schematic of a Mach-Zehnder interferometer, the field at each arm and the fields at the outputs. The graph shows the visibility for such an interfeometer for transmitivity t^2 near 50%.

real time on a normal photo-diode because the power of this auxiliary laser was high enough. This is much faster and easier than doing it with a photon counter which, for the amount of single heralded photons we had, a couple of seconds of integration time was needed to show a stable and representative value.

Beam splitter reflectivity must be exactly 50% to obtain perfect visibility on both output ports of the interferometer. Our beam splitters varied in reflectivity from 45 to 50%. The relation between visibility and reflectivity is obtained the following way: consider, as in Figure 3.11, a simple Mach-Zehnder interferometer. There is only a field of value E_0 entering through one of the sides. The first and second beam splitters are similar with reflectivities r and transitivities t such that no energy is lost ($t^2 + r^2 = 1$). Then the output fields are

$$E_a = E_0 rt(1 + e^{i\phi}) \text{ and } E_b = E_0(r^2 + t^2 e^{i\phi}) \tag{3.15}$$

The intensity in the a side will then modulate between 0 and $|4E_0rt|^2$ which reaches its maximum when $r^2 = t^2 = 1/2$. On the b side, it will oscillate with the same amplitude and an offset. If the beam splitters are not perfectly 50:50 then side a will suffer from amplitude degradation while side b will see a degradation of its visibility. For the b side the visibility is then:

$$\begin{aligned} \mathcal{V} &= I_0 \frac{|r^2 + t^2|^2 - |r^2 - t^2|^2}{|r^2 + t^2|^2 + |r^2 - t^2|^2} \\ &= I_0 \frac{1 - |1 - 2t^2|^2}{1 + |1 - 2t^2|^2} \end{aligned} \tag{3.16}$$

This relation is plotted in Figure 3.11 for transmitivity t^2 values from 0.4 to 0.6. In setting up the experiments of this thesis care was taken to use beam splitters whose visibility was 0.98% or higher. This, in turn, implied selecting beam splitters with transitivities in the $0.45 - 0.55\%$ range.

Beam-splitters and polarization.

When storing and manipulating path and polarization qubits on a same photon, beam-splitters used for path gates must not alter the polarization of the qubits. If they depended on polarization then they would not act as a single qubit gate but a gate which mixes both degrees of freedom. One will need to do such things to implement controlled gates between both kind of qubits, but it is convenient to keep things apart: on one side, single qubit gates for each degree of freedom and; on the other, controlled gates. To keep things apart beam-splitters must have transmitivities which do not depend on polarization. This can be achieved fairly good with dielectric beam splitters. Figure 3.12 shows the transmission for each polarization for two different beam splitters bought at Thorlabs (www.thorlabs.com) both with order code BS017 but from different production batches. One fulfils the necessary characteristics while the other one does not.

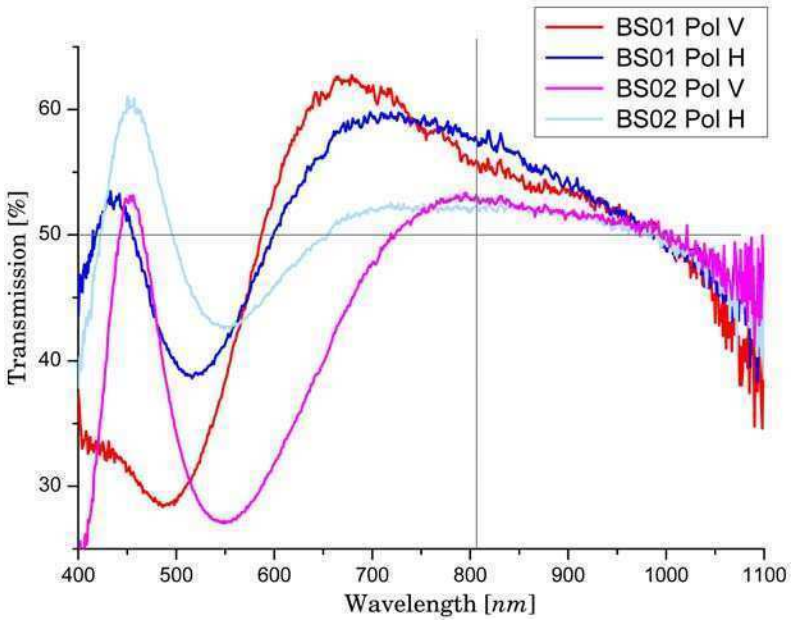

Figure 3.12: **Non polarizing beam splitter transmittances.** Measured non polarizing beam-splitter transmission as a function of the wavelength for each polarization. For our working wavelength (810nm) BS01 shows too high and unbalanced tranmisions while BS02 is adequate. These beam-splitters were bought with the same order code but came from different production batches.

3.2 Controlled Gates

There is little use to qubits if one can only do single qubit rotations. Most interesting and useful quantum information tasks require controlled gates. Controlled gates are physical processes in which the final state of a qubit depends not only its initial state but also on the initial state of another one. This can be achieved through carefully designed interaction.

Controlling qubits in different degrees of freedom in a same photon is relatively straight forward. However controlling qubits stored in different photons is a bit trickier. In the next sections these possibilities are explored for qubits in the polarization and path degrees of freedom of photons.

3.2.1 Within a Photon

Controlling the polarization state of a photon depending on its path or vice-versa can be done with linear optical elements. The states of photons with these two qubits in them will be described by the physical and logical states:

$$\begin{aligned} |\psi\rangle &= (\alpha\hat{a}^\dagger_{aH} + \beta\hat{a}^\dagger_{bH} + \gamma\hat{a}^\dagger_{aV} + \delta\hat{a}^\dagger_{bV})\,|0\rangle \\ &= \alpha\,|aH\rangle + \beta\,|bH\rangle + \gamma\,|aV\rangle + \delta\,|bV\rangle \end{aligned} \tag{3.17}$$

Where now the creation operators have two labels indicating both its polarization and path content.

Control path, target polarization

Creating a gate that modifies the polarization depending on the path is the simplest of the controlled gates for qubits in a same photon. By placing different wave plates on each path one can modify the polarization qubit depending on which path it is in. For example, as in Figure 3.13, consider placing a HWP in one path, say path b, and nothing in the other. Then the evolution will be a controlled HWP. A general input state will then be transformed as:

$$\begin{aligned} C_{H_\theta}\,|\psi\rangle &= C_{H_\theta}(\alpha\,|aH\rangle + \beta\,|bH\rangle + \gamma\,|aV\rangle + \delta\,|bV\rangle) \\ &= \alpha\,|aH\rangle + H_\theta\beta\,|bH\rangle + \gamma\,|aV\rangle + H_\theta\delta\,|bV\rangle \end{aligned} \tag{3.18}$$

A special case is of particular interest. If $\theta = \pi$ then, up to a global phase, the gate H_π is a NOT gate which inverts the input. In such a case the controlled gate is then, up to a (now local) phase, a controlled-NOT (CNOT). This gate inverts the the polarization qubit only if the path qubit is in the b mode and does nothing otherwise.

$$C_{H_\pi}\,|\psi\rangle = \alpha\,|aH\rangle + i\beta\,|bV\rangle + \gamma\,|aV\rangle + i\delta\,|bH\rangle \tag{3.19}$$

The extra i phase appearing on the path b qubits could be eliminated by a phase plate if it were necessary.

A general control and anti-control gate can be constructed with a series of quarter and half wave plates as described before and shown in Figure 3.13. Such gates have been used several times throughout this thesis.

Special care must be taken to match path lengths. In the CNOT gate just described, the path which does not have the plate is optically shorter than the one that does. This must be compensated either by making this path geometrically longer or by placing some kind of plate in its way. We found the best solution was always to design symmetric gates where on both path the beam encounters the same optical elements but at different angles. This is easier to align and does not cause intensity imbalances because of different optical interfaces on each path.

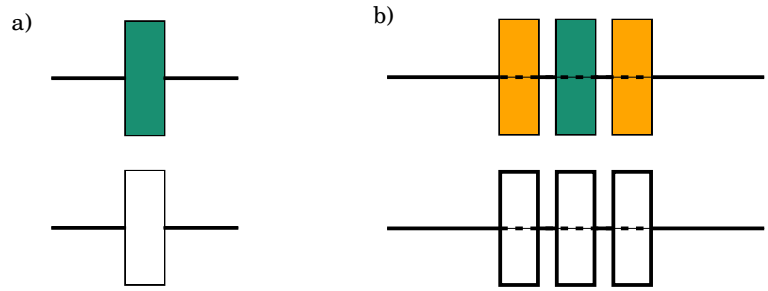

Figure 3.13: **Controlled Path - Target Polarization gates**. In a) A just a HWP (green) is placed in one of the paths and a glass plate is placed on the other to compensate optical paths. In b) a sequence of QWP (yellow) and a HWP do an arbitrary controlled operation; again glass plates on the other path must be inserted to compensate for path differences.

Control polarization, target path

This kind of gates were not used in the experiments presented in this thesis but are reviewed for completeness. The path of a photon can be changed depending on its polarization content by using polarizing beam splitters (PBS). PBSs are layered dielectric interfaces are designed so as to completely reflect one polarization and transmit the other one.

A simple but unstable CNOT gate can be constructed by just making both paths meet at a PBS as shown in Figure 3.14. If Vertical polarization is transmitted and Horizontal reflected then a general input state is then transformed, up to tunable phases, as:

$$\begin{aligned} PBS\,|\psi\rangle &= PBS(\quad \alpha\,|aH\rangle + \beta\,|bH\rangle + \gamma\,|aV\rangle + \delta\,|bV\rangle) \\ &= \qquad \alpha\,|bH\rangle + \beta\,|aH\rangle + \gamma\,|aV\rangle + \delta\,|bV\rangle \end{aligned} \tag{3.20}$$

The paths are exchanged depending on the polarization. If the polarization is H the path changes if the polarization if V then it does not. However, this configuration does not provide stability for the phases of the path qubtis. A stable, Sagnac-like, configuration was proposed by Fiorentino and Wong [FW04]. Although it is a bit more involved it is stable against thermal fluctuations. The idea, shown in Figure 3.14, uses a dove prism to rotate the paths of the beams in the interferometer in different directions depending on the entrance direction. Alternatively a couple of cylindrical lenses can be used to provide this rotation[WRD+06, WRD+07].

3.2.2 Between Photons

Photons interact very little with each other. In fact, in free space, there is no photon photon interaction. However, quantum gates which affect information stored in a photon depending on the information carried by another one can be implemented. There are two strategies: using photon statistics or using some intermediary medium. This kind of gates were not used in the experiments of this thesis.

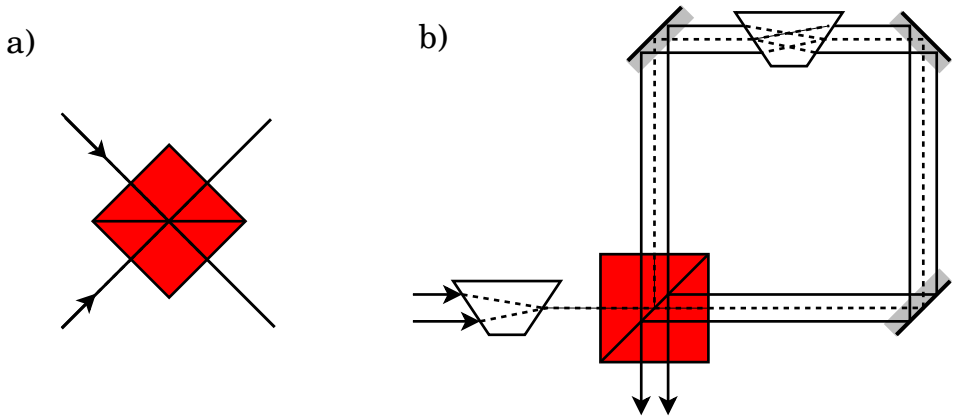

Figure 3.14: **Controlled Polarization - Target Path gates**. In a) A PBS as acts as CNOT gate however this configuration is interferometrically unstable. The configuration of b) also does as CNOT gate but is stable due to its Sagnac-type design.

They are reviewed here for completeness and because they are needed for one of the proposed experiments presented in Appendix A. Also, an original extension of one of these gates to include photons with path and polarization qubits is presented in Appendix B.

Schemes have been proposed using intermediary medium such as the nonlinear Kerr effect in crystals to perform controlled gates. The Fredkin[Mil89] gate, for example, does a CNOT in dual rail qubits. However all known materials have a Kerr effect which is too small to implement single photon gates. No gates like these have been implemented so far.

On the other hand many gates relying on the Bosonic statistics of photons have been proposed and experimentally realized. Some of these act on Path qubits and others on Polarization. The downfall with this kind of gates is that results must be post-selected to ensure proper gate operation. In what follows we explore some of the basic concepts underlying this idea and give details on how to implement specific gates.

HOM Interference

Two photon (or HOM) interference is the basic physical phenomenon behind probabilistic gates between photons. It was first observed by Hong, Ou and Mandel in [HOM87]. It is different from first order interference which is caused by phase terms in two possible trajectories of a same photon, as is the case in, for example, double slit, Michelson and Mach-Zehnder interferometers. HOM interference, on the contrary, is purely a two photon effect and it occurs because of the statistics involved with indistinguishable Bosonic particles.

Photons obey Bose-Einstein statistics therefore their field mode operators commute if they are distinguishable and don't if they are not (omitting the hats over the operators): $[a_i, a_j^\dagger] = \delta_{ij}$ and $[a_i, a_j] = [a_i^\dagger, a_j^\dagger] = 0$. These relations must be preserved even after mode transformations as in a beam-splitter. In fact, in a 50:50

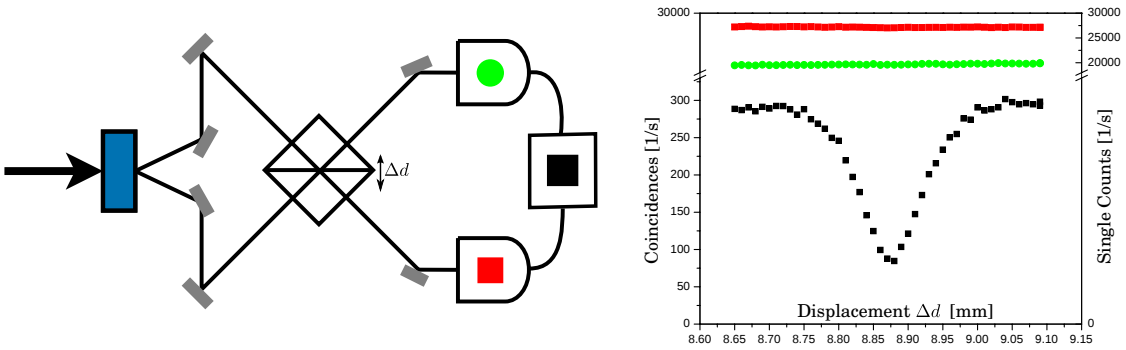

Figure 3.15: **A two- photon interference experiment**. Pairs of photons generated by SPDC interfere in a 50:50 bean splitter. Photons are collected at each of the outputs and coincidences are recorded as a function of the path difference. When both paths are equal the coincidences are reduced because both photons exit the beam-splitter together. The width of the dip depends on the coherence length. These results are part of Julian Dajczgewand's undergraduate thesis experiments.

beam splitter the modes are transformed as described in 3.1.2 which in terms of modes is:

$$a'^{\dagger} = \frac{a^\dagger + ib^\dagger}{\sqrt{2}} \quad \text{and} \quad b'^{\dagger} = \frac{ia^\dagger + b^\dagger}{\sqrt{2}} \tag{3.21}$$

These new modes also fulfill the Bosonic commutation relations. Now if one considers two indistinguishable photons arriving at such a beam-splitter at the same time the initial state $a^\dagger b^\dagger |0\rangle$ will be transformed in the output in a remarkable way.

$$\begin{aligned} |1_a, 1_b\rangle = a^\dagger b^\dagger |0\rangle \quad &\rightarrow \quad \frac{a'^\dagger - ib'^\dagger}{\sqrt{2}} \frac{-ia'^\dagger + b'^\dagger}{\sqrt{2}} |0\rangle \\ &\rightarrow \quad \frac{1}{2}(-ia'^\dagger a'^\dagger + a'^\dagger b'^\dagger - ib'^\dagger(-i)a'^\dagger - ib'^\dagger b'^\dagger) |0\rangle \\ &\rightarrow \quad \frac{1}{2}(-ia'^{\dagger 2} - ib'^{\dagger 2}) |0\rangle \\ &\rightarrow \quad \frac{-i}{\sqrt{2}}(|2_{a'}, 0_{b'}\rangle + |0_{a'}, 2_{b'}\rangle) \end{aligned} \tag{3.22}$$

The output is a superposition of both photons either on one path or the other, but never one on each side. This effect is also called photon bunching, for indistinguishable photons "stick together" when meeting at the beam splitter. It is the basis of all statistical gates between photons.

The extent to which photons will interfere in this way depends on how indistinguishable they really are. Different effects such as imperfect spatial mode matching, polarization differences or timing differences (among others) may reduce this effect. Figure 3.15 shows results from a HOM interference experiment.

Statistical Gates

Statistical gates for two photons can be performed using HOM interference. The basic idea of a statistical gate is as follows. First, the input photons interfere in such a way that the output will be in a superposition of the desired transformation and others which will be ruled out. Then, upon measurement, it will collapse "correctly" with a fixed probability. Some of these gates use ancilla photons and confirm their "correct" collapse, indicating successful gate operation, by measuring ancillas in a given way. Alternatively, if no ancillas are used, successful operation is checked by coincidence detection of the photons involved.

There have been many proposals to build gates this way. The seminal proposal by Knill Laflamme and Milburn [KLM01] was followed by several other proposals which use the polarization degrees of freedom (DOF) of the photons instead of the the momentum DOF [KYI01, PJF01, RLBW02, HT02, SKK01]. The many proposals can also be divided into those which require ancillas [KLM01, GC99, KYI01, PJF01, RLBW02] and those which don't [HT02, SKK01]. All these proposals center their attention on controlled gates between photons having qubits in only only one of their degrees of freedom. It is interesting however to explore the possibility of doing these kind of gates with photons carrying qubits in more than one of their degrees of freedom. This is done in Appendix B.

The rest of this Section will focus on the gate proposed by Hofmann and Takeuchi [HT02] which was later simplified and realized experimentally by three different groups at the same time [LWP$^+$05, KSW$^+$05, OHTS05].

The Hofmann and Takeuchi Gate

The original proposal can be summarized as follows. A CPhase acts on the computational basis performing the following transformation

$$\begin{aligned} |00\rangle &\rightarrow |00\rangle \qquad |01\rangle \rightarrow |01\rangle \\ |10\rangle &\rightarrow |10\rangle \qquad |11\rangle \rightarrow -|11\rangle \end{aligned} \tag{3.23}$$

When using polarization qubits it is common to assign vertical and horizontal polarizations as the computational basis. Unlike ideal qubits, which are distinguishable, photons are not. Moreover this indistinguishability is at the heart of the gate's operation which relies on bosonic interference. We must therefore address it correctly, the easiest and most elegant to do so is with Fock operators. This will simplify notation of state representation as well as that of the transformation of photon modes at linear optical media.

For example, the computational state $|00\rangle$ is not the physical state $|h_a h_b\rangle$ where a and b denote the spatial mode (path) in which each photon is. As photons are indistinguishable bosons the physical state is $(|h_a h_b\rangle + |h_b h_a\rangle)/\sqrt{2}$, which is symmetric upon their permutation. As before, these states can be more compactly expressed with creation operators as $\hat{a}_h^\dagger \hat{b}_h^\dagger |0\rangle$. We can simplify notation even further by just specifying the state by its annihilation operators as $a_h b_h$ and by omitting the hats over the operators. Later on one can recover the ket notation. With this compact

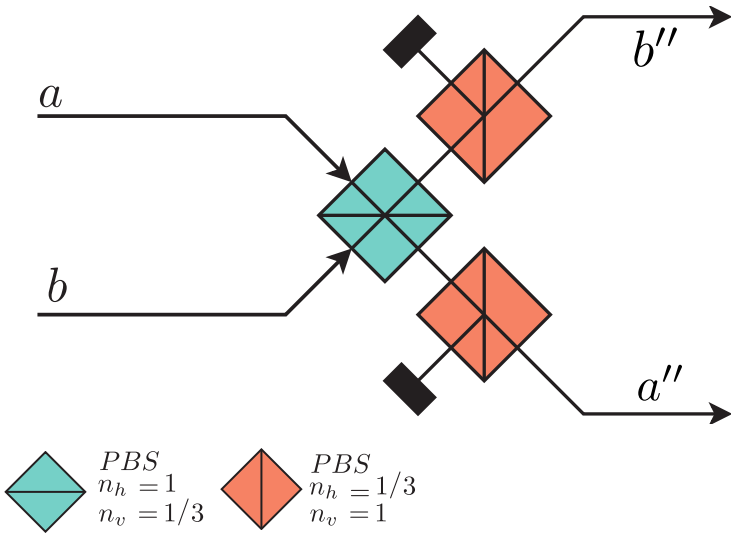

Figure 3.16: **The Hofmann Takeuchi CPhase gate.**

notation the CPhase gate is written as:

$$\begin{aligned} a_h b_h &\rightarrow a''_h b''_h \quad ; \quad a_h b_v \rightarrow a''_h b''_v \\ a_v b_h &\rightarrow a''_v b''_h \quad ; \quad a_v b_v \rightarrow -a''_v b''_v \end{aligned} \tag{3.24}$$

The physical implementation of the CPhase is as indicated in Figure 3.16. The first polarizing beam splitter (PBS) has horizontal transmitivity $n_h = 1$ and vertical transmitivity $n_v = 1/3$. It transforms the input and output modes as.

$$\begin{aligned} a_v &\rightarrow \tfrac{1}{\sqrt{3}}\left(a'_v + \sqrt{2}b'_v\right) \quad a_h \rightarrow a'_h \\ b_v &\rightarrow \tfrac{1}{\sqrt{3}}\left(-\sqrt{2}a'_v + b'_v\right) \quad b_h \rightarrow b'_h \end{aligned} \tag{3.25}$$

The relevant input states are those with only one photon per mode. The action of the first PBS on the computational basis transforms states as

$$\begin{aligned} a_h b_h &\rightarrow a'_h b'_h \\ a_h b_v &\rightarrow \frac{1}{\sqrt{3}}\left(a'_h b'_v + \sqrt{2}a'_h a'_v\right) \\ a_v b_h &\rightarrow \frac{1}{\sqrt{3}}\left(a'_v b'_h + \sqrt{2}b'_v b'_h\right) \\ a_v b_v &\rightarrow \frac{1}{3}\left(-a'_v b'_v + \sqrt{2}(b'_v b'_v - a'_v a'_v)\right) \end{aligned} \tag{3.26}$$

The first term of each line is the only one that has to be taken into account. The others will be ruled out by postselection as they contain more than one photon per path. As required for the CPhase gate, the $a_v b_v$ term undergoes a sign change while the others don't. However, the weight of these terms is different. To compensate this, a second PBS is placed on each path with the vertical on horizontal transmitivities interchanged $n_h = 1/3$, $n_v = 1$ (alternatively the same kind of PBSs can be

used with a half wave plate at $\pi/4$ before and after them [RLBW02]). After these PBS the output states are:

$$\begin{aligned} a_h b_h &\rightarrow \frac{1}{3} a''_h b''_h + \psi_q \quad ; \quad a_h b_v \rightarrow \frac{1}{3} a''_h b''_v + \psi_q \\ a_v b_h &\rightarrow \frac{1}{3} a''_v b''_h + \psi_q \quad ; \quad a_v b_v \rightarrow -\frac{1}{3} a''_v b''_v + \psi_q \end{aligned} \tag{3.27}$$

Where ψ_q has the undesired terms with either two photons in one mode or photons on the unwanted modes c and d. Now it is clear that, when one photon is detected at each of the output ports, this configuration performs the the CPhase gate. This occurs with with probability 1/9.

Chapter 4

Photon Generation and Detection

Availability of single photon sources is one of the big issues currently holding the development of scalable quantum computing. Several methods exist for generating single or small amounts of photons in a controlled fashion but still there are no scalable solutions.

For the last decade or two, spontaneous parametric down conversion (SPDC) at non linear crystals has provided an excellent tool for few photon experiments. The experiments presented in this thesis also use photons generated this way. Anyway, by this method, experiments with more than 4 photons are extremely difficult to perform and have very low photon generation rate [KWO+10].

Other sources such as excitons in semiconductor nano posts[MKB+00, KBKY99] or Nitrogen vacancies in diamond crystals[KMZW00] might lead in some years to deterministic sources of on demand photons with good enough spectral and timing characteristics for optical quantum information. Still, nowadays, these sources are at a very preliminary stage and the road to scalability is not totally clear.

This chapter describes in detail the physics of SPDC as well as technical laboratory aspects and their use as photon sources paying special attention on those used in our lab.

4.1 Spontaneous Parametric Down Conversion

In a non linear medium one photon can be converted into two photos. This physical phenomenon is called Spontaneous Parametric Down Conversion (SPDC).

It is called that way for several reasons. Spontaneous refers to the fact that these events occur in a random unpredictable way with certain probability. It is called parametric because it resembles electrical parametric amplifiers. Down conversion indicates that photons with higher frequencies are converted into photons with lower frequencies.

4.1.1 Physics

Spontaneous parametric down conversion occurs due to a non-linear interaction of electromagnetic waves with matter. When electromagnetic waves travel through matter their field moves the medium's charges polarizing it. Depending on the way

atoms are arranged in this medium the polarization response will be different. In most transparent solids (crystals or amorphous) charges move in the material very little so their movement can be approximated as a harmonic oscillator. In such cases the polarization response to an external field will be linear. The polarization and the electric field will then be related by the polarizability χ, by $P = \chi E$. However, at high fields or in media where the potentials felt by the particles the are not harmonic, non linear behavior appears. That is, the polarization of a solid, is, in general, a non linear function of the electric field which can be expressed as a series $P = \chi^{(1)}E + \chi^{(2)}E^2 + \chi^{(3)}E^3 + \ldots$. These effects are generally not isotropic so to correctly describe them one must characterize the polarization response through nonlinear tensors $\chi^{(i)}$ as:

$$P_i = \chi^{(1)}_{ij} E_j + \sum_{jk} \chi^{(2)}_{ijk} E_j E_k + \sum_{jkl} \chi^{(3)}_{ijkl} E_j E_k E_l + \ldots \tag{4.1}$$

Materials which have high non linear coefficients are called simply non-linear materials or $\chi^{(2,3)}$ materials depending on which coefficient is high. High $\chi^{(2)}$ is the non-linearity responsible for SPDC and is characteristic of uniaxial crystals such as BBO (Beta Barium Borate), KTP (Potassium titanyl phosphate) and many others[DGN99].

The energy associated to this interaction is $H = \vec{E} \cdot \vec{P}$ so for second order ($\chi^{(2)}$) materials one has $H = \sum \chi^{(2)}_{ijk} E_i E_j E_k$. This cubic dependency on the electric field is responsible for SPDC as well as other non linear phenomenon such as frequency doubling, squeezing generation, optical parametric amplification, etc. Although this analysis could be continued with this classical wave picture we now switch to a second quantization description where we will describe the fields in terms of their elementary excitations; i.e. photons. This change provides a clearer insight on some of the possible processes that can occur in this kind of crystals. To do so we replace the electric field vector by its operator

$$\vec{E} = \sum_k \hat{\epsilon}_k \xi_k \left(a_k e^{-i\omega_k t + i\vec{k}\cdot\vec{r}} + a_k^\dagger e^{i\omega_k t - i\vec{k}\cdot\vec{r}} \right). \tag{4.2}$$

Where a and $a^\dagger$ are photon annihilation and creation operators in a mode labeled by k. Then ω_k is the frequency of the field, $\vec{k}$ its wave vector, $\hat{\epsilon}_k$ it polarization direction and ξ_k a number with units of electric field.
The Hamiltonian of the system, which determines the photon's time evolution in the crystal, will then have terms of the kind:

$$a_i^\dagger a_j a_k \ , \ a_i a_j^\dagger a_k^\dagger \ , \ a_i^\dagger a_j^\dagger a_k^\dagger \ , \ etc. \tag{4.3}$$

Some of these terms will be relevant or not in the description of the evolution of the system depending on the initial state and on the set of final states explored. The time evolution of the system in the interaction picture will be given by $U = e^{-itH_{int}}$. Where H_{int} is the interaction Hamiltonian but without the harmonic time dependence.

Parametric down conversion is a process in which photons from a strong pump beam are converted into pairs of photons in two other modes called, for historical reasons, signal and idler. The initial state can be described then by the state

$|N_p, 0_s, 0_i\rangle$ which has N photons in the pump mode, and 0 in the signal and idler modes. The final state will be then one in which one pump photon is converted into a signal and an idler photon: $|(N-1)_p, 1_s, 1_i\rangle$. The term in the Hamiltonian responsible for this interaction is $a_s^\dagger a_i^\dagger a_p$. It destroys a photon in the pump mode and creates one in each of the output modes. Naturally, all the other terms are also present, but if we restrict our observations to the above initial and final modes the evolution of the system will be correctly characterized by an evolution operator of the form $U = e^{-i\alpha a_s^\dagger a_i^\dagger a_p}$. Here we are collapsing all parameters into the symbol α. Also we are not writing it as a unitary evolution by not including the Hemitian conjugate of $a_s^\dagger a_i^\dagger a_p$. Moreover, the pump mode has a large number N of photons so the operator a_p may be replaced by the number $\sqrt{N}$ which is proportional to the value of the square root of the intensity[1]. Then, the evolution operator has the form $U = e^{-i\sqrt{N}\alpha a_s^\dagger a_i^\dagger}$. Also one may drop the identification of the amount of photons on the pump beam from the state vector. The time evolution under these conditions may be approximated as a series expansion of the exponential acting on the initial state as

$$\begin{aligned} |\psi_f\rangle &= U|0_s, 0_i\rangle = e^{-i\alpha a_s^\dagger a_i^\dagger}|0_s, 0_i\rangle \\ &= (1 - i\sqrt{N}\alpha a_s^\dagger a_i^\dagger - (\sqrt{N}\alpha)^2 a_s^{\dagger 2} a_i^{\dagger 2} + \cdots)|0_s, 0_i\rangle \\ &= |0_s, 0_i\rangle - i\sqrt{N}\alpha|1_s, 1_i\rangle - (\sqrt{N}\alpha)^2|2_s, 2_i\rangle + \cdots . \end{aligned} \tag{4.4}$$

The first term accounts for nothing happening, the second one for the generation of one pair of photons, the third one for the generation of two pairs, etc. This expansion is valid because the value of $\sqrt{N}\alpha$ is typically very low. In our experiments, for example, we pump a $3mm$ BBO crystal with a $405nm$ laser at a power of $40mW$; this accounts for $N_{sec} \approx 10^{16}$ photons per second in the pump mode[2]. By selecting output modes with interference filters of $\Delta\lambda \approx 5nm$ and collecting light into multi-mode optical fibers we register pair generation at a rate of $(\sqrt{N_{sec}}\alpha)^2 \approx 10^4 pairs/second$.

The N appearing in the expressions above should not be expressed in terms of photons per second, but rather, in terms of photons per total interaction time τ. For continuous wave pumps it is reasonable to assume that the interaction time is in the order of the coherence time of the pump beam. For the pump used this was $\tau \approx 10^{-12}$. This way $N_{sec}\tau = N$[3]. Then, the amount p_n of pairs of photons per second can be expressed in terms of the amount of photons per second as

$$p_n = \tau^{n-1}(N_{sec}\alpha^2)^n. \tag{4.5}$$

These arguments show the difficulty in generating many pairs of photons by this method. If we were to look at generation of two pairs of photons, in the same conditions as motioned above then the generation rate would be $p_2 = \tau(N\alpha^2)^4 \approx 1 \times 10^{-4}$

[1]Replacing the operator a_p is valid when the number of photons N in that mode is so large that extracting a photon from the field makes no difference $a_p|N\rangle \approx \sqrt{N}|N\rangle$. This is property is also exactly fulfilled by coherent states $a_p|\nu\rangle = \nu|\nu\rangle$. The pump field is the output of a laser which is coherent. The replacement can thus be understood from both point of views.

[2]The relation between the laser power P its frequency ω and the average amount of photons per second N_{sec} is given by $P = \hbar\omega N$

[3]This estimates an expansion parameter to be $\sqrt{N}\alpha \approx 10^{-4}$ which justifies approximating the time evolution by the first terms in its Taylor series.

$double\ pairs/second$; for three pairs the probability is $p_3 = 10^{-16} triple\ pairs/second$. Increasing power and collinear configurations help increasing this rate but it is always at the expense of having many more pairs too, which in turn lowers the signal to noise ratio.

Other $\chi^{(2)}$ nonlinear phenomena

This type of nonlinear interaction is responsible for many other well known physical phenomena. Each one of these are caused by different terms and input-output observed states. For example:

- **Frequency doubling** is an effect whereby two photons are "upconverted" into a photon of higher energy. The Hamiltonian term responsible for this has the form $a^\dagger_{2\omega} a_\omega a_\omega$ and it acts on an input state with lots of photons in the ω mode: $|0_{2\omega}, n_\omega\rangle$. This is a widely used technique to obtain lasers at frequencies where there are otherwise unavailable.

- **Frequency mixing** is the name given to the process where two photons with different energies combine into another photon in an analogue fashion to frequency doubling. Third harmonic generation is a particular example of this process where two photons of frequency ω and 2ω are combined into one with frequency 3ω.

- **Sqeezing** can be produced on coherent states, when the pump field can be treated as classical, by the terms $\alpha a^{\dagger 2} + \alpha^* a^2$.

- **Optical parametric oscillation and amplification** are very similar to SPDC but the input states have non null photon numbers in the signal and/or idler modes. In parametric amplification the process in enhanced by introducing an extra input beam while in optical parametric oscillation the output of SPDC is resonant in a cavity which "stores" these photons further enhancing the oscillation.

Phase Matching

The above description is correct but by collapsing too much information into the parameter α relevant physics has been left aside. SPDC only occurs if a set of "selection rules" known as *phase matching conditions*, are met. These two conditions are that the energy and momentum must be conserved inside the crystal:

$$\begin{aligned} \omega_p &= \omega_s + \omega_i \\ \vec{k}_p &= \vec{k}_s + \vec{k}_i \end{aligned} \tag{4.6}$$

The momentum conservation relation refers to the $\vec{k}$ vectors inside the crystal which are normally both frequency and direction dependent; it must only be approximately fulfilled in the case of thin crystals[4]. In negative uniaxial crystals

[4]The converted states probability amplitude has a factor $sinc[l(\vec{k}_p - \vec{k}_s - \vec{k}_i)]$ which forces perfect momentum conservation for crystals with lengths l much larger than the wavelength involved and only approximate momentum conservation if the crystal's length is small.

these conditions can be met with two different polarization combinations which can fulfill the phase matching conditions. These conditions are called Type I and Type II phase matching.

Type I The polarization of the signal and idler beam are parallel to each other and perpedicular to the pump. The pump is polarized along the crystal's extraordinary axis. $e \rightarrow oo$.

Type II The polarization of the signal and idler beam are perpendicular to each other, one of them is parallel to the pump. The pump is polarized along the crystal's extraordinary axis. $e \rightarrow oe$.

Also, apart from the polarizations, the output angles will depend on the crystal orientation. Two distinct configurations are worth mentioning. In collinear phase-matching both signal and idler have the same direction as the pump beam. On the contrary in non-collinear phase matching signal and idler have directions different from the pump beam. Figure 4.1 shows a schematic view of non-collinear type I and II SPDC as well as images of the visible output of these two processes on BBO crystals pumped at $405nm$.

Degenerate SPDC. The phase matching conditions allow a continuous family of output states to be generated. The special case where both output photons have the same frequency is called degenerate. It is specifically important because photons in these conditions are indistinguishable and therefore will be subject to two photon interference of the HOM kind. Though not necessary in many other cases, it is also a convenient condition to work with because all the optical setup works on only one wavelength. In the experiments of this thesis, this was the working condition.

Angular Spectrum

The properties of the incoming pump field will be mapped into the bi-photon probability distribution. Following the treatment by Monken et. al.[MRP98] and Walborn's Thesis[Wal04], in the paraxial approximation, the electric field of the pump beam with angular distribution $\vec{v}(\vec{k}, z)$ is written as

$$\vec{E}(\rho, z) = \frac{1}{2\pi^2} \iint \vec{v}(\vec{k}, z) e^{i\vec{k}\cdot\vec{\rho}} d\vec{k}. \tag{4.7}$$

Under the assumption that the output angles of the signal and photon beams are small, the wave function of the photon pair generated by parametric down conversion will be

$$|1_s, 1_i\rangle = \sum_{\vec{s}_s, \vec{s}_i} C_{\vec{s}_s, \vec{s}_i} \iint \vec{v}(\vec{k_s} - \vec{k}_i, z) \left| \vec{k}_s, \vec{s}_s; \vec{k}_i, \vec{s}_i \right\rangle d\vec{k}_s d\vec{k}_i. \tag{4.8}$$

Where the $\vec{s}$ indicate polarization directions and the coefficients $C_{\vec{s}_s, \vec{s}_i}$ determine the polarization state of the output. The angular information of the pump is transfered to the bi-photon state in a non separable way: $\vec{v}(\vec{k_s} - \vec{k}_i, z) \neq \vec{v}(\vec{k_s}, z)\vec{v}(\vec{k}_i, z)$. This non separability is responsible for many of the non-local effects in twin photons generated by parametric down conversion.

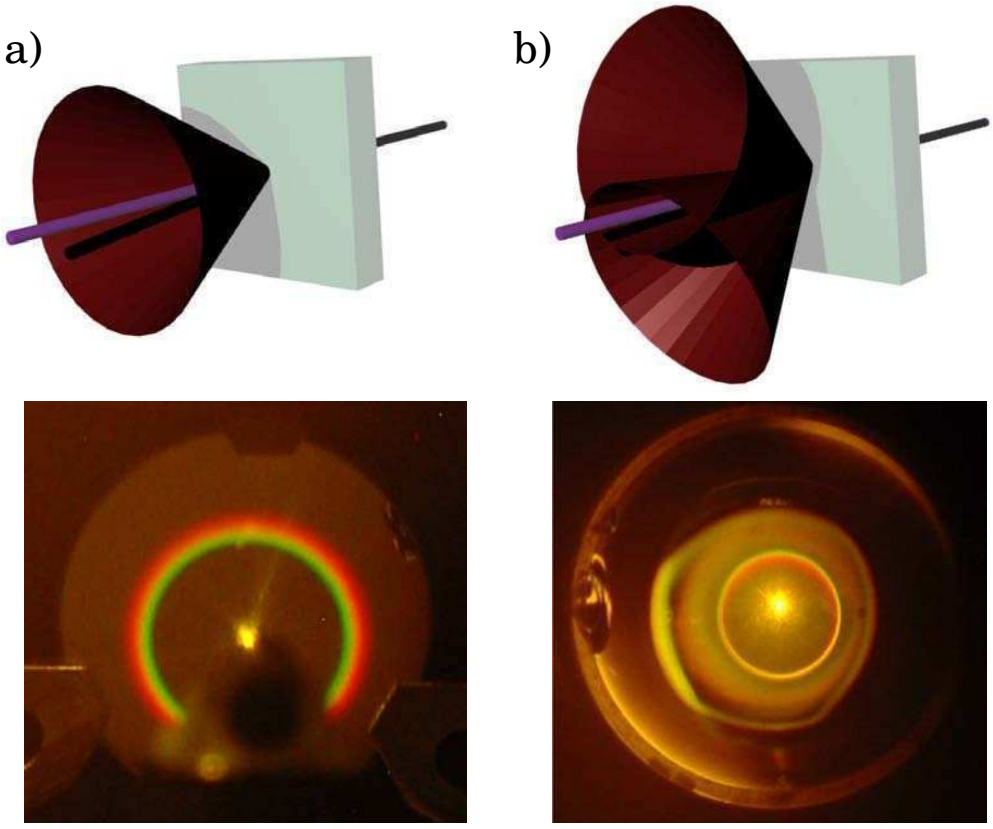

Figure 4.1: **Schematic view and images of SPDC at BBO crystals pumped at** $405nm$. a) shows Type I and b) shows Type II SPDC. The scheme illustrates the pump beam hitting the crystal and the generated light cones of one certain wavelength. Other cones will also be generated at other wavelengths, but are not shown. In Type I photon pairs are generated diametrically opposed on the same cone. In Type II photons pairs are generated one in each cone symmetrically opposed with the pump as center of symmetry. The images taken in our lab show SPDC for both types of phase matching. In Type II only the bottom cone is seen, the other cone emits only in the infrared region which was not visible with the camera used. Also the characteristic cone asymmetry of Type II can be compared to the more symmetric case of Type I SPDC. Images were recorded by placing a $25cm$ lens at its focal distance from the crystal and recorded with a commercial digital photo camera $1m$ away from the lens; the intense 405nm beam was blocked only by a filter in b) and by a filter and a beam dump in a). Image a) was taken by Nahuel Freitas and Sabrina Sacerdoti and image b) was taken by Griselda Mingolla.

4.1.2 Heralded Photons

SPDC can be used to generate heralded single photons. In fact in the main two experiments of this thesis single photons were generated this way. A heralded, or announced, photon source is called that way because it produces photons in a random way whose presence can be determined by the existence of another photon.

As described above, by pumping a uniaxial nonlinear crystal, one will probabilistically generate pairs of photons. By detecting one of these photons one can assert that in the other mode its "twin" will be present. Then, the first detection, say in the idler mode, announces the presence of another photon in the signal mode. Naturally, detection and collection efficiency together with photon loss at optical elements will account for many detections on both sides which are not corresponded by a twin detection, i.e. a coincidence detection. These events are ruled out and not considered in the final results. Only coincidence detections are counted as valid events.

Single Photons

Single photon generation by this method can be confirmed by measuring second order correlation function $g^{(2)}(0)$ on the signal beam conditioned or not to the detection of a photon on the idler ("herald"). This has been done many in the past[TND$^+$04] and was confirmed in our lab in an undergraduate project carried out by Sabrina Saceroti and Nahuel Freitas. They measured the second order correlation function to be $g^{(2)}(0) = 0.004 \pm 0.006$ when conditioned to a signal in the herald and $g^{(2)}(0) = 0.9 \pm 0.3$ when not. This clearly shows anti-bunching statistics as expected from a single photon source when conditioning the results to the appearance of the herald.

Timing Coincidences

How good photon timing coincidences are, is determined by the spectral bandwidth of the photons. This bandwidth is in turn determined by both the geometric overlap of the outputs with the detectors and the filters placed before the detectors. In any cases we worked on conditions where we tried to match the spectral selectivity of these two, obtaining a final collection bandwidth of about $\Delta\lambda \approx 2nm$ at a center wavelength of $810nm$. This implies a coherence time $\tau_c = \lambda^2/c\Delta\lambda$ of $\approx 2ps$. This is in fact what is observed in two photon interference experiments as discussed below.

Any detection window above the coherence time is good for heralding single photons. However it must not be made too big so as to record coincidences from events that are not. We worked with coincidence windows in the order of $10ns$ mainly limited by electronics. Coincidence circuits and other considerations on detecting single photons are discussed in Section 4.2.

4.1.3 Entangled Photons

There are several ways to generate entangled photons with SPDC. Moreover, photons can be entangled in many degrees of freedom (hyper-entangled states). Entanglement in the polarization of two photons can be achieved by either Type I

[KWW+99] or Type II [KMW+95] spontaneous parametric down conversion. Moreover, both these methods were explored in our lab by Mónica Aguero and Griselda Mingolla. Hyper-entangled states were observed and measured in polarization-momentum[BLPK05, BCMDM05], polarization-time[BLPK05], and other combinations [MQK+09].

In the experiments of this thesis entanglement within qubits of a same photon was used, but not entanglement between photons.

4.1.4 Experimental techniques

Apart from the above generalities about SPDC, many details are relevant for the realization of experiments. This subsection describes how we took care of most of them in the construction of a heralded photons source with a BBO crystal and a 405nm laser diode.

Phase Matching

All phase matching conditions were calculated using free software available from the physical measurement laboratory at NIST[5]. The first thing that has to be decided is the crystal angle $\theta_{crystal}$ with respect to the pump beam. That is, the angle between the crystal's optical axis and the beam. This angle is critical in determining whether phase matching is possible and at which angles different wavelengths exit the crystal. The possible phase matching angles for the degenerate down conversion of photons from $405nm$ to $810nm$ in BBO crystals are found to be from $40.9°$ to $139.1°$. The behaviour of $\theta_{crystal}$ between $40.9°$ and $90°$ is symmetric to the one between $90°$ and $139.1°$. Figure 4.2 shows the phase matching function for the generation of photons at $810nm$ as a function of the output angles for several different angles between the crystal's uniaxial axis and the pump. Light from the signal and idler beams are emitted in two cones. As the crystal's angle increases the cones get larger. This in turn means that light is more dispersed in different directions making it more difficult to collect.

There are several things to take into account when choosing the crystal angle. While for generating heralded photons the optimal configuration might seem to be in the limit of $\theta_{crystal} = 40.9°$ where all the generation collapses to one point this is not the case. Unfortunately near the allowed limit angle the conversion efficiency lowers so this is not a good working condition, this situation is depicted in the top left corner of Figure 4.2. Conversely, in collinear generation, as in the top right corner of Figure 4.2, both cones "touch" at the center of the pump beam and is a very good configuration for it has a high conversion efficiency. This configuration however has two downfalls: the two photons generated can't be spatially distinguished and the intense pump beam must be separated by the use of several filters. To avoid these complications a small angle, close to collinear, configuration can be adopted. Choosing such a small angle makes the spread of the signal and idler beam to be small as well. This way not so many photons are lost and still one can spatially distinguish both photons and separate them from the pump beam without the use

[5] http://www.nist.gov/pml/div685/grp03/phasematching.cfm

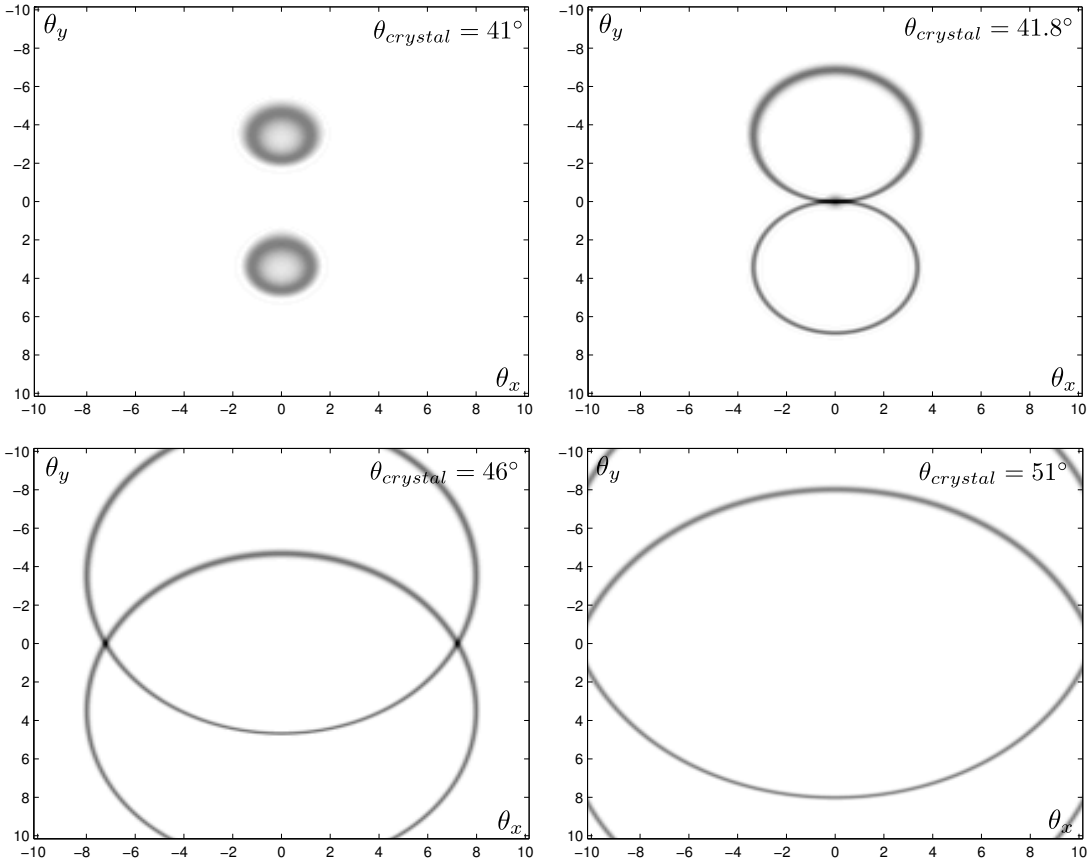

Figure 4.2: **Phase matching functions**. Phase matching functions are shown as a function of the output angles for the conversion of $405nm$ light into degenerate pairs at $810nm$ for different angles of the crystals optical axis with respect to the pump beam.

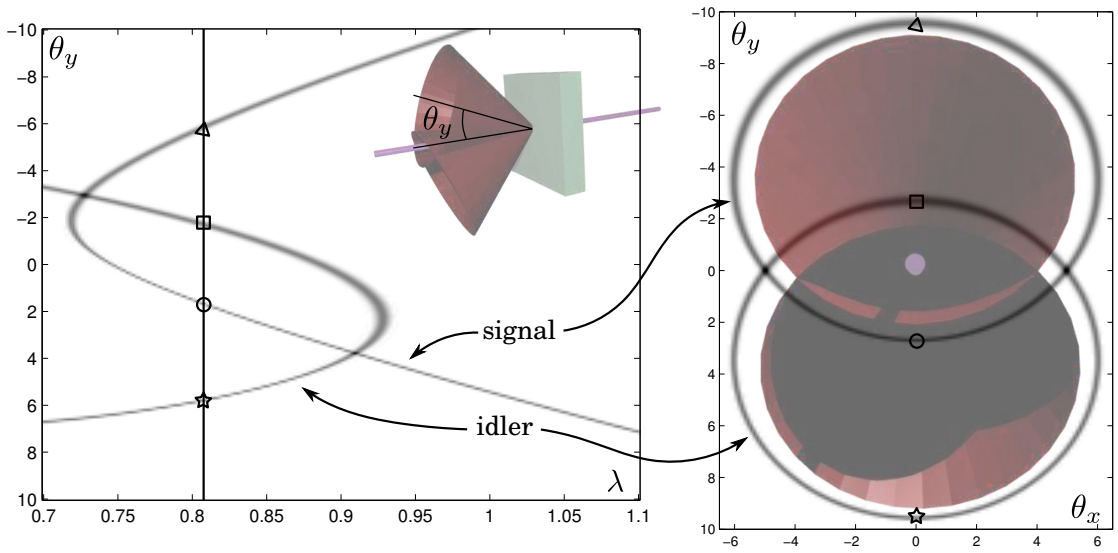

Figure 4.3: **Phase matching functions for the configuration used** $\theta_{crystal} = 43.9°$. The signal and idler beams are identified in both plots. The $\theta_x - \theta_y$ plot corresponds a cut at $810nm$ in the $\lambda - \theta_y$ as shown. Also, the marked points $\triangle, \square, \circ, \star$ on one plot and the other correspond to the same places on each. Shown in color are $3D$ sketches of the crystal and down conversion angles and directions. For the experiments of this thesis light is collected in the intersection of the cones.

of filters. In our case we chose this angle to be $\theta_{crystal} = 43.9°$. Figure 4.3 shows the phase matching function as a function of the output angles for the generation of photons in $810nm$ as well as the phase matching function as a function of the wavelength and the vertical output angles.
Both the collinear configuration and the one we chose can be used to generate heralded photons or polarization entangled photons.

The comparison of the the λ-θ_y phase matching plot of Figure 4.3 with the image of type II SPDC shown in Figure 4.1 reveals the explanation given before in the caption of that Figure. The only cone seen is the one corresponding to the idler photons which continues in the visible spectrum $\lambda < 750nm$. The signal photons are not seen because they have wavelengths $> 710nm$ which are almost outside the visible spectrum and are not recorded by the camera used. Also seen in the picture is that green photons are on the outside of the cone while red ones are inside. This can be confirmed by the phase matching function: at smaller wavelength top and bottom coordinates of the cones get larger.

Crystal Length and focusing

In general the amount of photons generated by SPDC depends linearly on the crystal length and does not depend on focusing. In a real experiment the crystal length cannot be made arbitrarily long and focusing of the pump beam must be taken into account.

As seen before, photon pair generation by SPDC is proportional to the intensity

of the field. In contrast to the inverse process (frequency doubling), the efficiency is not affected by focusing the pump. However, as will be described in detail below, phase matching does depend, at second order, on focusing parameters, which when optimized can lead to much higher count rates.

Crystals can not be made arbitrarily long, specially when working with non-collinear phase matching. If the crystal length is longer than the coherence length of the laser then photons generated at one part of the crystal will add up incoherently with those generated somewhere else. This is specially a problem when constructing sources aimed to produce pure states and critical when producing pure entangled states. Also, one must take into account that the "cones" describing the emission are in fact a superposition of continuous set of cones along the pump beam. If the crystal is very long then these cones will smear out and thus the generated pairs will spread in space too.

Pump Astigmatism

Output modes of laser diodes are normally astigmatic. If this is not corrected then the photons generated will copy this spatial mode which is specially undesirable if coupling to single mode fibers. Mode astigmatism can be corrected by cylindrical lenses. We used a simple scheme where a slightly unbalanced cylindrical lens telescope compresses and collimates the direction which was larger and worst collimated at the laser output.

Photon Collection

Photons may be detected by placing a raw detector right on its path. However it is convenient to couple photons into optical fibers and then send them to the detectors. This has two main advantages: fiber couplers are easier to move around and align than the whole detector and, more importantly, mode filtering can be done if single mode fibers are used.

For optimal mode collection and filtering we used an idea presented by [KOW01]. The main point is that optimal collection at a given wavelength range can be achieved by matching the divergences of the beam with the phase matching divergences of SPDC and then matching these to the fiber's numerical aperture. Moreover, if this is correctly done, the interference band pass filters normally used to select photons from a given wavelength can be replaced by low pass filters so that the real, more stringent, filtering is done spatially. This way, frequency filtering is transfered to the transverse spatial domain and frequency selection can be achieved through spatial filtering.
This is advantageous because off-the-shelf interference band pass filters have low transmitivities of about 50%. Removing them can increase detection probability significantly. Anyway some filtering, to get rid of ambient and pump light, is needed. Low pass filters, as the ones used (Schott RG-715), can have transmitivities in the near infrared of more than 90% while providing very good extinction for visible and near-UV wavelengths.

Several relations of Gaussian beams are useful to have in mind in order to understand how this spectral-gaussian mode maching works. The divergence of a

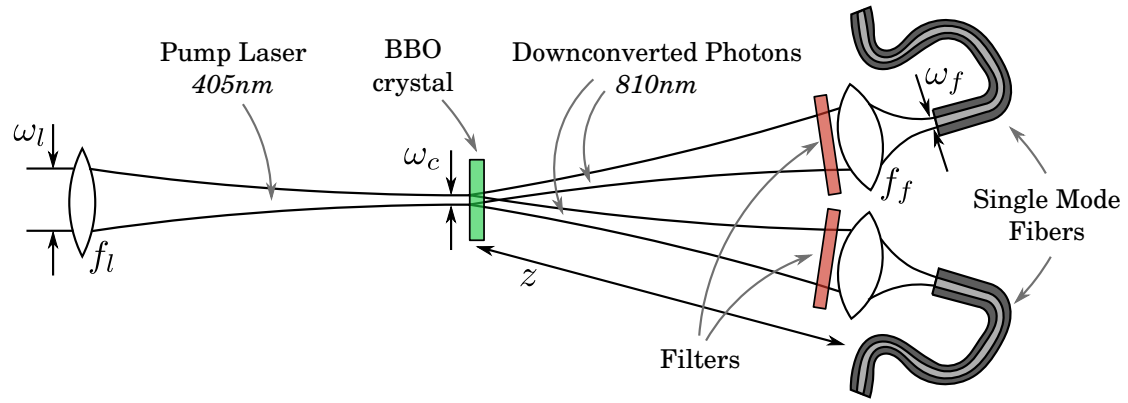

Figure 4.4: **Sketch of the collimation angles and distances.** (Not to scale.) The Gaussian divergences are matched to the spectral divergences to spatially select a collection bandwidth (see text). Single mode fibers are sent either to detectors or further stages of the experiment.

Gaussian beam α and and its beam width ω are related by $\alpha = \lambda/\pi\omega$. A collimated beam with width ω on a lens of focal distance f will be focused to the size $w_{focus} = \lambda f/\pi\omega_{lens}$ at a distance f from the lens. Finally, a lens of focal distance f at a distance z_1 from a focus of width ω_1 will refocus with size $\omega_2 = f\omega_1/(z_1 - f)$ at a distance such that $1/z_1 + 1/z_2 = 1/f$.

With the above in mind the correct parameters can be chosen for optimal collection into single mode fibers. Figure 4.4 shows a sketch of the beam collimation distances and sizes. We aimed at a spectral bandwidth of $\Delta\lambda \approx 10nm$. Using the phase matching software by NIST described above the angular spread of wavelength can be calculated; for the working parameters we obtained $d\alpha/d\lambda \approx 0.33mrad/nm$. Then the divergence of the wanted photons is $\alpha = \Delta\lambda(d\alpha/d\lambda) \approx 3.2mrad$. This divergence must be matched to the Gaussian beam divergence. To do so the mode size of the pump must be focused at the crystal with a width $\omega_c = \lambda/\pi\alpha \approx 80\mu m$ (where $\lambda = 810nm$). The laser beam radius ω_l must then be focused by choosing the right lens to $\omega_c = \lambda f_l/\pi\omega_l$ (where here $\lambda = 810nm$).
On the fiber side the the single mode fibers used had mode field diameters of $5.6\mu m$ so that the beam with in the fiber is half of that $\omega_f = 2.8nm$. Our fiber collimators had lenses with a focal distance of $f_f = 11mm$ so that the distance they had to be placed from the crystal was $z = f_f(\omega_c/\omega_f - 1) \approx 300mm$.
One last thing has to be taken into account. The lens size must be at least as large as the beam that one wants to collect. This is indeed our case since $\alpha z \approx 1mm$ is smaller than the lens size $\approx 3mm$.

Collection efficiencies

With the above taken into account, in one of our experiments we had collection efficiencies of about 24%. We calculate this the following way. We measured $S_1 = 100.000$ and $S_2 = 60.000$ single counts on each channel and $C_{12} = 9.500$ coincidence

counts. The overall efficiency η is then calculated to be

$$\eta = \frac{C_{12}}{\sqrt{S_1 S_2}} = 0.12 \tag{4.9}$$

Then if one assumes that the efficiencies are symmetric on both collection arms and taking into account that detector efficiencies are of 50% for the working wavelenth one obtains an approximate collection efficiency of 24%.

The collection efficiency was not very high because of remaining astigmatism and improper Gaussian mode matching. Also the imbalance of the single counts is due to not perfectly symmetrically chosen collection angles. This was not a problem however for heralded photon generation but it is something to take closer care when using SPDC as an entangled photon source. These efficiencies could be improved by better correcting the astigmatism of the pump beam as well as better matching of the spectral-gaussian modes.

4.2 Photon detection

All current photon detection techniques are destructive. That is, in all available methods the photon whose presence one wants to record must be absorbed in some medium in order to generate an electrical signal which gives count of the existence of that photon. The three main single photon detection techniques available are: photomultiplier tubes, avalanche photon diodes (APDs) and superconducting circuits.

Photomultiplier tubes and APDs are the only two well established technologies that have reached commercial products. They have different benefits and downfalls depending on the application. For experiments with SPDC normally APDs are preferred because they have much higher efficiencies in the near infrared part of the spectrum ($\approx 50\%$ compared to $\approx 10\%$ or less for photomultiplier tubes). They also have very low dark counts going from as low as $25 counts/s$ to up to $500 counts/s$ depending on how much one is willing to pay. Some photomultiplier tubes can get this low, but getting the right electrode combination which gives a high efficiency and low dark counts might not always be possible, specially in the near infra red. On the negative side APDs have a big dead time of about $50ns$ and they have no possibility to resolve photon number (they will produce the same signal either if one or 10 photons arrived at the same time).

Superconducting circuits are a very promising as detectors with high efficiency, high bandwidth and photon number resolving characteristics. Anyway they are still at the development level and require cryogenic cooling.

In the experiments presented in this thesis photon detection was done with APDs. This Section reviews APD technology as well the peripheral software and electronics needed to do photon counting, coincidence detection and statistics. Also some remarks on the physics of photon detection which must be taken into account to estimate errors is reviewed.

4.2.1 Photon counting

Depending on the light source, photons will be detected with different statistical properties. Also the detection resolution time might limit the observed statistics. In the next subsections the physics and some technical details involved in photon counting are described.

Physics

Coherent light sources, as those produced by lasers, are described by a Poissonian distribution on the photon number. That is, the probability of measuring n photons in a time interval T will obey a Poissonian distribution:

$$p(n) = |\langle n|\alpha\rangle| = e^{-|\alpha|^2}\frac{|\alpha|^{2n}}{n!} \tag{4.10}$$

It has mean value $\langle n\rangle = |\alpha|^2$ and variance $\langle \Delta n\rangle = \sqrt{\langle n\rangle}$. Its second order correlation function $g^{(2)}(\tau)$, which expresses the probability of detecting a second photon a time τ after the detection of the first one, is flat ($g^{(2)}(\tau) = 1$). That means that in a coherent beam the detection of one photon poses no conditions on the detection of a subsequent photon.

Thermal light behaves very differently. Upon the detection of a photon there exists a higher probability to detect a second one just afterwards. This is quantified by the second order correlation function which is $g^{(2)}(\tau) = 1 + \exp(\pi\tau/\tau_c)$. This expresses that there is a probability twice as big of detecting two events separated by a time shorter than τ_c than there is to detect two events separated by a time much larger than the coherence time τ_c. This effect is also sometimes referred as photon bunching for photons are more often detected "bunched" up in time.

For such a thermal light source the probability to detect n photons of frequency ν in a given time window is

$$p(n) = \frac{\exp(-nh\nu/k_Bt)}{(\exp(-h\nu/k_Bt) - 1)^n} = \frac{\langle n\rangle^n}{(1 + \langle n\rangle)^n} \tag{4.11}$$

where the mean value is $\langle n\rangle = (\exp(-h\nu/k_Bt) - 1)^{-1}$ and the variance is $\langle \Delta n\rangle = \sqrt{\langle n\rangle^2 + \langle n\rangle}$. However when detecting photons one does so in a frequency range $\Delta\nu$ so the above single mode description might not be valid. It will only be valid if the detection statistics are well resolved by the measurements. This will happen when the detection time is much shorter than the coherence time: $t_d \ll t_c \sim 1/\Delta\nu$. If this is not the case then no correlation will be registered between subsequent events and the photon detection statistics can be effectively described by a Poissonian distribution as is the case of coherent beams.

In experiments with photons generated by SPDC we detected with spectral bandwidths of $5 \sim 10nm$, which imply correlation times of $\tau_c \approx 1ps$. This is much shorter than our detection time. When using one detector its dead time ($\approx 50ns$) limits time resolution[6]. Then for calculating the statistical error in a

[6]The output could be split by beam splitters into different detectors therefore reducing the limit posed by dead time. However in the rage of a few nanoseconds electronics start to limit again detection time.

given measurement it will be fair to assume that it will obey Poissonian statistics $\langle \Delta n \rangle = \sqrt{\langle n \rangle}$.

It is very difficult to measure statistical properties of thermal light. This is mainly due to the stringent condition on the detection times and and spectral bandwidths. If one were to filter $810nm$ light with a fairly good spectrometer, enabling filtering a bandwidth of $\approx 0.001nm$ then one would need detection times of $\approx 2ns$. Thought this is not impossible nowadays it is more or less at the limit of current technologies. Historically, to see thermal beam statistics, pseudo thermal light sources with tunable coherence time were studied[AGS66, Are65]. While setting up the laboratory we did such an experiment and explored the possibilities to use such an effect to transmit "ghost images"[BBB02]. The details and results are discussed in Appendix C.

Accidental Coincidences

Even when two detectors receive light from different sources, every now and again, a pair of unrelated photons will trigger a coincidence; these coincidences are called accidental. They occur just by chance and are proportional to the light arriving at each detector and the window gate. Given a window time of Δt and single count rates of S_1 and S_2 (of light from an uncorrelated light source) one expects the amount of coincidence counts C_{acc} to be all accidental and have a value

$$C_{acc} = S_1 S_2 \Delta t. \tag{4.12}$$

If detectors receive light from uncorrelated sources then the coincidences recorded will be linear in the amount of counts received in one of the detector. This linearity was checked to evaluate the coincidence circuit behaviour as mentioned above.

In any experiment there is always some uncorrelated light reaching both detectors. When generating entangled pairs or when using SPDC as a heralded photons source one always detects some unexpected coincidences due to this effect. This amount can be calculated with the formula above and subtracted from the measured value to estimate a better value for the "real" amount of coincidences coming from the experiment.

In good working conditions these values are, however, a small correction the values directly measured. For typical working values the ratio of "real" to accidental coincidences was of $100 \sim 200$ depending on the losses, the background light and the alignment.

4.2.2 Hardware and Software

Counts were tallied using a NI6602 adquisition board. This board has 6 counters which can work up to a rate of 80MHz. The inputs and outputs of the counters can be programmed by software to do perform different tasks such as counting transitions or generating pulse sequences. All programming and data collection was done via the LabView programming platform by National Instruments.

Photon counting was done the following way. One of the counters was feeded by the $80MHz$ internal clock. It was configured in such a way that it would produce an output pulse pulse every $0.1s$. These pulses were used as a time basis. The other

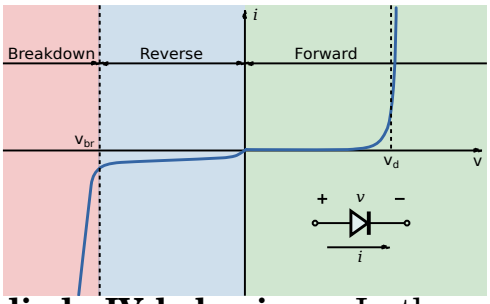

Figure 4.5: **Sketch of diode IV behaviour.** In the reverse voltage region the current is proportional to the light absorbed while in the breakdown voltage region proportionality is lost but single photon sensibility can be achieved. (Image from [Wika]).

counters were used for the actual counting. Triggered by the time basis pulse they would synchronously count pulses for $0.1s$, then report their value and reset for a new cycle. By software, larger addition times could be selected by adding as many $0.1s$ intervals as wanted. Though there is a short dead time between cycles this does not compromise the measurements. Some of the counters recorded the single counts while others recorded the coincidence outputs coming from the coincidence electronics.

Another detection technique, known as time stamping, is possible with this board. It was not used for the experiments in this thesis. Manly because it is very slow. Anyway, it is worth mentioning. The counters can all be fed by the clock as a source and the input signal as a gate. The clock increments the counters while the input signal tells the counter to inform its value. The arrival times are marked on a common timebase which is then continuously stored and periodically sent to the computer. Then the time series can be analyzed extracting single counts and coincidence rates from them. This method does not require the extra coincidence electronics described below. The $80MHz$ clock provides time stamping with time bins of $12.5ns$.

4.2.3 Avalanche photodiode

Avalanche photo diodes (APDs) are photodiodes which allow operation close to and even slightly above the breakdown voltage. In this regime they become very sensitive and can be used to detect single photons.

In a normal photodiode the current produced, when polarized with a negative voltage, is proportional to the light received. This happens because the photons, when hitting the diode, create free electrons by the photoelectric effect, which are then dragged across the junction producing a current. (This will happen if the photon energy is larger than the material's work function.) So the intensity of the current depends mainly on the amount of free electrons created and not on the voltage applied. Finally, as the amount of free electrons generated by the photoelectric effect depends only on the intensity of the light. The current is proportional to the intensity of the light hitting the diode.

If a large enough reverse voltage is applied on the photodiode (as in any other

diode) it will start to conduct. This voltage is called *reverse breakdown voltage*. APDs work at this voltage. When biasing an APD with a voltage very close to the breakdown, the diode becomes very sensitive to small amounts of light. A hand waving argument for this goes as follows: free electrons are accelerated in the diode because of the reverse voltage. If this voltage is large enough, then electrons will gain sufficient kinetic energy to extract other electrons when colliding with them. When this happens an avalanche of electrons is generated. This is similar to what happens in photomultiplier tubes. The current generated is not limited to one electron per photon, it is multiplied by this avalanche mechanism. However, this avalanche does not generate a big enough current to detect single photons. To detect single photons the reverse voltage must be pushed beyond the breakdown voltage. In such a case a single photon can trigger a self sustainable avalanche large enough to be detected. To stop the avalanche, and prevent damage one the photo diode, one has to reduce the voltage below the breakdown. This way the photodiode is "quenched" and left ready for a new detection.

Quenching can be done passively with a capacitor or actively by reducing the bias voltage. Modern APDs, as those sold by Perkin-Elmer, come with built-in electronics which takes care of reverse biasing, active quenching and pulse discrimination. The quenching mechanism is the main cause of detector dead time. In Perkin Elmer's AQRH model, which we used in the experiments presented in this thesis, the dead time is approximately 50ns.

4.2.4 Coincidence detection

Coincidences were detected by specially made electronic circuits. There were two approaches: a first one uses flip-flops[DM02] and a second one uses fast TTL integrated circuits[BBB09]. The second one was preferred to the first one mainly because its response remained linear for very high count rates ($> 10^6$).

As explained below in Section 4.1.2 pairs of photons generated by SPDC will coincide in times of the order of the ps. Recording coincidences at this speed is a challenging electronics issue. We worked with coincidence electronics with windows of $\approx 10ns$.

The main idea of both coincidence detection schemes is similar. The single photon counting modules used produce a TTL pulse of $35ns$ every time a photon is detected. Coincidence signals could be generated just by sending the pulses of both detectors into an AND gate and monitoring the output. If pulses overlap the AND gate will testify this by generating a pulse at the output. The coincidence window would then be of $35ns$. The first method, in fact, uses this pulse width as a time window. The second one, improves this by shortening the output pulses of the APDs.

The first method uses series of flip-flops to generate the output coincidence signal[DM02]. One of the signals is delayed with respect to the other one. This is done using a flip-flop as a monostable vibrator. Its pulse propagation time is set to approximately half the incoming pulse duration. Then a last flip-flop is used to detect the coincidence by sending the delayed signal to the CLOCK and the non delayed one to the DATA inputs. This last flip-flop will produce a coincidence signal whenever a signal arrives at the CLOCK and the DATA port was previously

on. The chips used were 74ACT74. This circuit would work very well for low single photon counts (< 100.000). At higher count rates it produced more counts that expected. This was checked by studying the accidental coincidences as explained below.

The second method used variable delays and an AND gate to produce a shorter pulse[BBB09]. The input pulse is split and one of the lines is delayed and negated. Then both lines are sent to an AND gate. A positive pulse with a size equal to the delay is produced. With this configuration all pulses generated are referred to the rise slope of the original pulses thus reducing extra errors due to jitter in the length of the pulses generated by the detectors. Delays were produced by propagating the signal through a series of AND gates with its other input set to $+5V$. Each gate had an approximate propagation time of $\approx 5ns$. The coincidence time was limited by the logic's family minimum pulse lengths. We used the 74F00 family and obtained pulses of $\approx 9ns$. These coincidence detectors were found to behave linearly up to more than 1.500.000 single counts. They were build by Nahuel Freitas as part of his laboratory training in 2008.

Part II

Experimental Quantum Process Tomography

Chapter 5

Quantum Process Tomography

Quantum process tomography is an experimental task by which one determines parameters which describe the evolution of a quantum system. Here quantum processes are studied in the context of quantum information where physical systems are described by qubits. Extensions to higher dimensional states (qudits) as well as continuous variable systems exist but are beyond the scope of this thesis[LR09].

An unknown quantum process affecting a physical system composed of n qubits can be represented as a linear map (a quantum channel) taking initial states ρ_0 into final states $\rho = \mathcal{E}(\rho_0)$. The amount of parameters characterizing such a map scale exponentially with the amount of qubits $O(2^{4n})$ making its full description and reconstruction a technically impossible problem even for more than a couple of tens of qubits. All current available methods, such as those reviewed in this chapter, present different problems if there were to be used to tomograph large systems. Either they require the inversion of exponentially big matrices or they require clean ancillary qubits which are normally not available or not as good as one would need. The next chapter presents a new method that solves these problems.

One can quickly picture the difficulty in characterizing an arbitrary quantum process the following way. First, characterizing a general classical n bit evolution is already a difficult task. The most general description involves up to 2^n rules each of size n. That is, 2^n possible input states for which the output state is a n bit result. In quantum mechanics it gets even more difficult for both the input and output state can be any superposition of all the classically allowed combinations. Moreover, to determine the output state in a quantum system one needs to do different measurements repeated times in order to determine approximately the output state. That is, one must do state tomography on the output. In fact, this is the spirit of the standard tomography method developed by Nielsen and Chuang[NC00] and described below.

Fortunately, the kind of channels one is normally interested in can be described with much less information; the trick comes in finding methods to efficiently extract this information. This chapter presents the main ideas behind quantum process tomography. It reviews the main aspects in the description of general quantum processes as well as the existing methods available for quantum process tomography.

5.1 The χ matrix representation

As described in the introduction, a quantum channel can be described, under very general assumptions, as a completely positive linear map acting on the space of density matrices, i.e. $\rho_{out} = \mathcal{E}(\rho_{in})$. Then, one can always choose a basis of the space of operators $\{E_i, i = 0, \ldots, D^2 - 1\}$ and write the channel as

$$\mathcal{E}(\rho) = \sum_{ij} \chi_{ij} E_i \rho E_j^\dagger \tag{5.1}$$

The coefficients χ_{ij} are D^4 complex numbers that completely characterize the quantum channel. Of course, all these coefficients are not independent. Reasonable physical restrictions on the kind of possible channels impose constraints on the χ matrices. Hermitivity will be preserved in the states of the system if and only if the χ matrix is hermitian. The channel described will be completely positive if and only if the χ matrix is completely positive. And last, the trace preserving condition implies that $\sum_{ij} \chi_{ij} E_j^\dagger E_i = I$. This last requirement is, in principle, not a physical restriction. Non trace preserving channels can account for loss or gain of particles in open systems. In Section 5.4 these conditions are analyzed in relation to handling real experimental data.

The choice of the basis E_i is in principle entirely arbitrary but it will be very convenient to choose the so-called Pauli basis in which operators E_i are all tensor products of Pauli operators acting on individual qubits[Ben06]. Conventionally, we will choose $E_0 = I$. For the rest of the operators we choose the following ordering convention: in the one qubit case I,X,Y,Z, in the two qubit case II,IX,IY,IZ,XI,XY,... and analogously one could continue for even more qubits.

5.1.1 Choi–Jamiołkowski isomorphism

There exists a very useful duality between process $\mathcal{E}$ defined over a given Hilbert space $\mathcal{H}$ and density matrices $\rho_{\mathcal{E}}$ corresponding to states in an extended Hilber space $\mathcal{H}\otimes\mathcal{H}$. This relationship was found by Choi and Jamiołkowski[Cho75, Jam72]. The connection between any process $\mathcal{E}$ and its corresponding density matrix $\rho_{\mathcal{E}}$ can be found as the evolution of the maximally entangled state $|\psi\rangle = \frac{1}{\sqrt{D}} \sum_i |ii\rangle$ the following way:

$$\rho_{\mathcal{E}} = (\mathcal{E} \otimes I) (|\psi\rangle\langle\psi|) , \tag{5.2}$$

That is, the isomorphic state is obtained by acting on only one of the parts of a maximally entangled state.

5.1.2 Relation of off-diagonal elements.

Another useful relation which is crucial in extracting information efficiently about channels when one has no information about it was derived by Lopez et. al. [Lóp09, LBPC10, Ben11]. It sets a bound for the size of the off-diagonal elements of a χ matrix of in terms of the values of the diagonal ones. Namely:

$$|\chi_{mn}|^2 \leq \chi_{mm}\chi_{nn}. \tag{5.3}$$

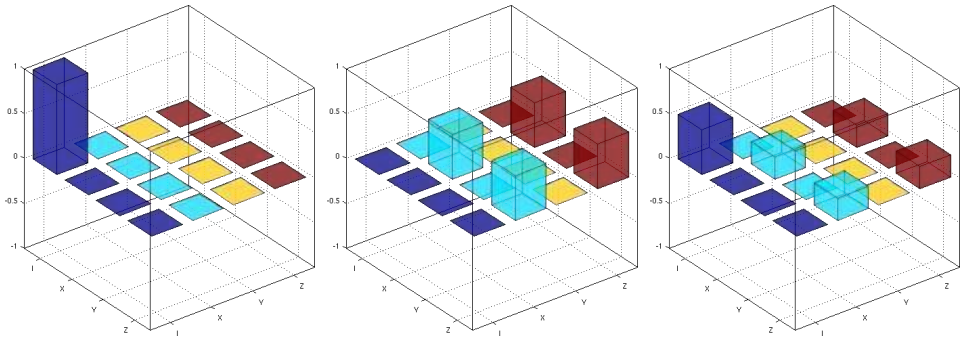

Figure 5.1: **Examples of one-qubit χ matrices.** Shown are the real part of the χ matrices of the Identity, a Hadamard gate and a mixture with equal weight of the Identity and the Hadamard.The imaginary parts of these matrices are null.

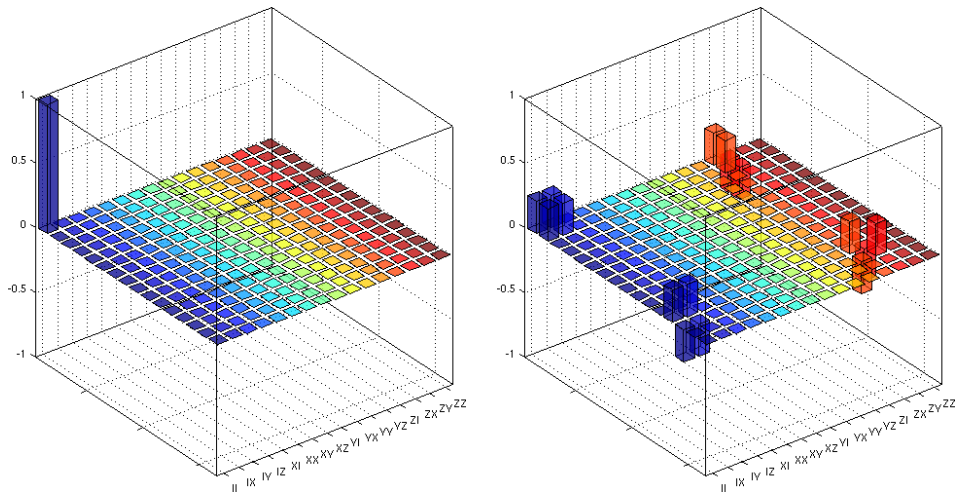

Figure 5.2: **Examples of two-qubit χ matrices.** Shown are the real part of the χ matrices of the Identity, a controlled NOT gate. The imaginary parts of these matrices are null.

This relation is valid for completely positive channels. A more general version of it can also be obtained for positive channels[Lóp09].

5.1.3 Examples

Folowing are some illustrative examples for systems of one and two qubits of several quantum channels and their relations to the χ matrices. For simplicity only channels with null imaginary parts are shown.

The simplest example to consider is the identity channel. In such a case the only nonvanishing coefficient is $\chi_{00} = 1$, while all other χ elements are null. The leftmost plots of Figures 5.1 and 5.2 show the real part of the χ matrices for the identity channel on one and two qubits respectively.

Following in complexity the center panel of Figure 5.1 shows a unitary gate on one qubit. The gate show is the Hadamard gate ($H = (X + Z)/\sqrt{2}$). The rightmost panel of Figure 5.1 shows the χ matrix corresponding to a process which is either

the Identity or the Hadamard with equal probability. That is, a special case (with $p = 1/2$) of the evolution:

$$\mathcal{E}(\rho) = (1-p)I\rho I + pH\rho H. \tag{5.4}$$

Finally, the right panel of figure 5.2 shows the emblematic controlled NOT (CNOT) gate which can be written in terms of Pauli operators as

$$U = \frac{I+Z}{2} \otimes I + \frac{I-Z}{2} \otimes X. \tag{5.5}$$

5.2 Existing Algorithms for Quantum Process Tomography

This section reviews the standard algorithm for Quantum Process Tomography which was developed by Nielsen and Chuang[NC00]. It is the "industry standard" in determining the evolution of small quantum systems[MKH$^+$09, BSS$^+$10, BAH$^+$10, NAB$^+$08, WGP$^+$07]. This algorithm is used in this thesis as a standard to compare the performance of our new algorithm in the full determination of processes. Other QPT methods are reviewed and discussed in Appendix E.

5.2.1 Standard - Nielsen & Chuang QPT

The standard and most straight forward version of QPT was proposed by Nielsen and Chuang [NC00]. The basic idea is to choose a set of input states, evolve them through the channel, perform state tomography on them and then use that information to reconstruct the χ matrix. The problem with this scheme, though straight forward, is that it requires resources that scale exponentially with the number of qubits. It is also a method that enables only full process characterization, needing all the information to be collected before anything about the process can be said. It is, anyway, the standard method to which many other algorithms are compared. In the experiments of this thesis, when characterizing a process by a new method, we compared our performance to that of the Nielsen and Chuang method.

Following White et. al. [WGP$^+$07], to perform Standard QPT one must do the following steps:

1. Choose a fixed basis $\{\rho_j\}$ of D^2 operators for the density matrices of the system, evolve them through the channel $\mathcal{E}$ and do state tomography on the output states obtaining all the information about the channel in a λ_{jk} matrix such that
$$\mathcal{E}(\rho_j) = \sum_k \lambda_{jk}\rho_k. \tag{5.6}$$

2. Define the coefficients β_{jk}^{ab} relating the operators E_a of the χ representation and the $\{\rho_j\}$ basis chose for the states such that $E_a\rho_j E_b^\dagger = \sum_k \beta_{jk}^{ab}\rho_k$. Then the χ matrix can be obtained by inverting the system of equations
$$\sum_{ab} \beta_{jk}^{ab}\chi_{ab} = \lambda_{jk} \tag{5.7}$$

For a small amount of qubits this inversion can be performed very easily. The details for the one qubit case can be found in the book by Nielsen and Chuang [NC00] and for the two qubit case in a paper by White et. al. [WGP+07].

In all cases non entangled bases are used for state preparation and measurement. In the language of polarization states, we used the bases $\{\rho_\alpha\}$ constructed with the density matrices corresponding to the $\alpha \in H,V,D,R$ pure states. For two qubits we used as a basis the direct tensor product $\{\rho_{(\alpha\beta)}\} = \{\rho_\alpha \otimes \rho_\beta\}$. Naturally, for path qubits the states used are the ones which have the same representation in the computational basis as the H,V,D,R. The polarization notation is, however, maintained for simplicity.

5.3 Selective Efficient Quantum Process Tomography

The chapter presents a general method for quantum process tomography which works in a selective and efficient manner even in systems with a large number of qubits. Both characteristics (selectivity and efficiency) are crucial if one is to characterize systems of many qubits. Efficiency means that the amount of work that has to be done to characterize a quantum channel does not scale exponentially with the number of qubits. In this context work includes: quantum operations, measurements and classical computation. This, in turn, imposes selectivity as a necessary condition because the complete description of a general quantum channel is always an inefficient task. As outlined in Chapter 5 the amount of parameters characterizing a general quantum channel of n qubits scales as $O(2^{4n})$. Then, procedures that allow accessing partial information about a channel regardless of its size are crucial. This partial information must also be accessed with resources that scale polynomially with the number of qubits.

The method of selective and efficient quantum process tomography was initially developed by Juan Pablo Paz, Fernando Pastawsky and Ariel Bendersky[BPP08, BPP09]. The first two experimental verifications of this method are the core of this thesis and are presented in the following chapters. This section presents the general mathematical tools and algorithms associated with this method leaving the details of each implementation for the chapters describing the experimental setups in a photonic environment.

In essence the method maps any relevant parameter of a quantum process onto the average transition probabilities between a special set of quantum states through a quantum process. Such states can be efficiently prepared, sampled and detected. Several strong theoretical results about quantum channels and Hilbert spaces are the keys that make this method powerful.

5.3.1 Generalized Fidelities

First there is a connection between the average fidelity of a modified quantum channel and the coefficients χ_{ab}. This can be established using a result which can be obtained using the invariance of the Haar measure under unitary transformations.

Indeed, it can be shown[ESM+07, Dan05, Ben11] that if one defines the functional $G(M,N)$ as the average over the Haar measure of the product of the expectation value of M and N then

$$\begin{aligned} G(M,N) &= \int d\left|\psi\right\rangle \left\langle\psi\right| M \left|\psi\right\rangle \left\langle\psi\right| N \left|\psi\right\rangle \\ &= \frac{1}{D(D+1)}(\mathsf{Tr}(M)\mathsf{Tr}(N)+\mathsf{Tr}(MN)). \end{aligned} \tag{5.8}$$

Using this result one can then show that any element of the χ–matrix can be interpreted as a fidelity of a modified map [BPP08, BPP09, Ben11]:

$$F_{ab} \equiv \int d|\phi\rangle\ \langle\phi|\mathcal{E}(E_a^\dagger|\phi\rangle\langle\phi|E_b)|\phi\rangle = \frac{D\chi_{ab}+\delta_{a,b}}{(D+1)}. \tag{5.9}$$

This is the average over the entire Hilbert space of the survival probability of a map $\mathcal{E}_{ab}$ defined as $\mathcal{E}_{ab}(\rho)=\mathcal{E}(E_a^\dagger\rho E_b)$. That is, a new map obtained by first transforming ρ into $E_a^\dagger\rho E_b$ and then applying the channel $\mathcal{E}$. At this point the efficient estimation of F_{ab} is equivalent to that of χ_{ab}. This allows for selectivity: if one can estimate the modified fidelity F_{ab} then one has information about χ_{ab} and not about other χ matrix elements. One can then extract selectively information about the quantum channel.

Selectivity is a crucial ingredient in any scalable QTP method. As described below, in Subsection 5.4.5, being able to find any χ_{ab} element selectively will allow for a method of *quantum process identification*. By this method different channels can be efficiently identified between each other and from a ideal target channel.

So the next step is to be able to efficiently estimate the modified fidelities F_{ab}. Two main obstacles are apparent impediments for the efficient estimation of F_{ab}. The first is that ***integrating over the entire Hilbert space*** apparently requires preparing and measuring a infinite number of quantum states. The second obstacle is ***implementing*** $\mathcal{E}_{ab}$. This effective channel $\mathcal{E}_{ab}$ is not physical (it is generally not a CP map unless $E_a=E_b$). Both of these obstacles can be resolved.

5.3.2 Integrating over the Hilbert space

The first obstacle can be surmounted by using the concept of 2-designs. One can transform the integral over the entire Hilbert space into a sum over a finite set of states that form a so-called 2-design, which exist for any dimension [DGS77, RBSC04, Dan05, MG07, DCEL09, KR05]. In fact, if the set $S=\{|\phi_j\rangle, j=1,...,K\}$ is a 2-design then

$$G(M,N)=\frac{1}{K}\sum_j \left\langle\phi_j\right| M \left|\phi_j\right\rangle \left\langle\phi_j\right| N \left|\phi_j\right\rangle, \tag{5.10}$$

where K denotes the number of states $|\phi_j\rangle$. The modified fidelities can then be calculated as a sum over the states of the 2-design.

$$F_{ab}=\frac{1}{K}\sum_j \langle\phi_j|\mathcal{E}(E_a^\dagger|\phi_j\rangle\langle\phi_j|E_b)|\phi_j\rangle. \tag{5.11}$$

Thus, if one is able to find a set of states with this property then the task of evaluating average fidelities reduces to estimating the average survival probabilities of such states $|\phi_j\rangle$.

Mutually Unbiased Bases and 2–designs

The theory of 2-designs was developed over the last couple of years[DCEL09, Dan05]. It is known that the set of states belonging to $D+1$ Mutually Unbiased Bases (MUBs) form such a 2-design (which therefore has $D(D+1)$ elements).

A highly efficient description of MUBs can be done by associating each bases with a complete set of commuting operators selected from the Pauli basis E_m[Ben11]. Thus, one can show[PR04, PRS05] that the set of D^2 Pauli operators can be split into $D+1$ disjoint commuting subgroups each one of which consists of $D-1$ operators (plus the identity, the only operator belonging to all subsets). In turn, every element of each of the subgroups can be obtained as the product of n generators (thus, the n generators entirely define each bases providing an efficient description of it). Also constructive ways of preparing the states of the MUBs also exist and can be done efficiently [Dan05, Ben11].

The coefficients χ_{ab} are related to the average fidelity of the channel $E_a\mathcal{E}E_b^\dagger$ which, considering MUBs are 2-designs and the state i from the basis k is $\left|\psi_i^k\right\rangle$, may be written as:

$$F_{ab}(\mathcal{E}) = \frac{1}{D(D+1)} \sum_{ik} \left\langle \psi_i^k \right| E_m^\dagger \mathcal{E} \left(\left|\psi_i^k\right\rangle \left\langle \psi_i^k \right| \right) E_m \left|\psi_i^k\right\rangle \tag{5.12}$$

Estimating F_{ab} with fixed precision

With the tools of 2-designs the continuous integral over the Haar measure is reduced to a finite sum. Still, the exact computation of χ_{ab} involves finite but exponentially large resources since $K = D(D+1) = O(D^2)$. However, one can approximately obtain the value of any χ_{ab} with a fixed precision that does not depend on the size of the Hilbert space. By randomly sampling (without repetition) over a subset of the 2-design, after M experiments one will estimate F_{ab} with an error that scales as

$$\Delta F_{ab} \propto \sqrt{\frac{1}{M}\left(1 - \frac{M-1}{K-1}\right)}. \tag{5.13}$$

In Appendix F a derivation of this formula is given. Figure 5.3 shows this a plot of this function for the two qubit case ($K = 20$). The error scales roughly as $1/\sqrt{M}$ for $M \ll K$ and vanishes for $M = K$. If sampling is done with repetition then the error scales as $1/\sqrt{M}$ for any value of M. In any case, the precision fixes the required number of experiments, not the size of the Hilbert space. This solves the problem of sampling over an infinite or exponentially large set of states.

Implementing $\mathcal{E}_{ab}$.

For the strategy to be viable one needs to be able to implement efficiently the modified channel over a set of states forming a 2-design $\mathcal{E}_{ab}(|\phi_j\rangle\langle\phi_j|) = \mathcal{E}(E_a^\dagger|\phi_j\rangle\langle\phi_j|E_b)$.

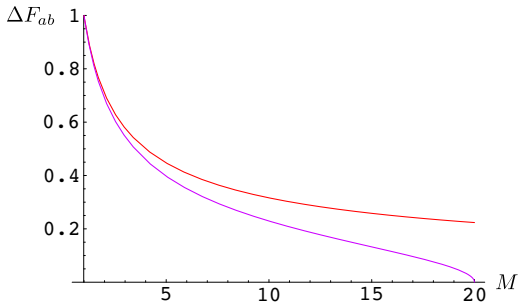

Figure 5.3: **Statistical errors.** Average error in the statistical estimation of F_{ab} after making M measurements of a total of $K = 20$ as is for two qubits. Purple: without repetition. Red: with repetition.

As it is, the operator $\mathcal{E}_{ab}$ is not necessarily an allowed physical process. There are, however a couple of ways around this problem.

5.3.3 Extracting diagonal elements.

Evaluating diagonal elements is the simplest task to do. This is because the evolution $\mathcal{E}_{aa}$ is, in fact, a valid physical evolution. The diagonal elements χ_{aa} are obtained as average fidelities of the map $\mathcal{E}_{aa}$, realized by composing the original map $\mathcal{E}$ with the unitary operation E_a: $\mathcal{E}_{aa}(|\phi_j\rangle\langle\phi_j|) = \mathcal{E}(E_a^\dagger|\phi_j\rangle\langle\phi_j|E_a)$. This is a physically possible operation so no extra tricks have to be used. Then, to estimate diagonal elements this way involves first preparing an arbitrary state $|\phi_j\rangle$ of the 2-design, then applying the gate $E_a^\dagger$ followed by the unknown quantum channel $\mathcal{E}$ and finally projecting into the state $|\phi_j\rangle$ and recording whether or not one has this state after the process. In circuit notation this reads:

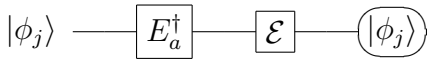

This must be repeated for several input states and then the average survival probability will be the estimator of the fidelity F_{aa}.

Extracting more information from projective measurements

There are actually two tricks that can boost a bit the efficiency and applicability of such a scheme for diagonal elements. The first one is noting that channel $E_a^\dagger\mathcal{E}(|\phi_j\rangle\langle\phi_j|)E_a$ with the E_a applied after the unknown channel $\mathcal{E}$ has the same fidelities as $\mathcal{E}_{aa}$ so the application of the operator can be "pushed" to the the end of the circuit:

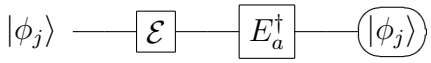

Then, if as states of the 2-design one uses the MUBs associated with the eigenvectors of the Pauli operators, the application of E_a can be omitted at all. This is the case because all the operators E_a will transform any state $|\psi_i^k\rangle$ into another state $|\psi_{i'}^k\rangle$ which belongs to the same k-th bases, $E_m\left|\psi_i^k\right\rangle = \left|\psi_{i'}^k\right\rangle$(up to a phase). This

is a consequence of the fact that given two Pauli operators they either commute or anti-commute with each other. Therefore, the commutation pattern between E_a and the generators of the k–th basis determines the image of state $|\psi_i^k\rangle$ under the action of E_a. It is therefore sufficient to randomly sample initial states $\left|\psi_i^k\right\rangle$ and measure the transition probability $p_{i,i'}^k$ that it will end up in the state $\left|\psi_{i'}^k\right\rangle$ for all the i, i' and k satisfying the relation:

$$\left|\left\langle\psi_{i'}^k\right| E_m \left|\psi_i^k\right\rangle\right| = 1 \tag{5.14}$$

In circuit notation this reads:

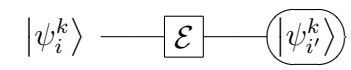

This mapping can be done efficiently and if one measures the output in the basis k instead of just the projection into the state $\left|\psi_{i'}^k\right\rangle$, which is what one normally does in experiments, then more information can be extracted from each trial. Further details are given in the description of the experiment performed on a two-qubit processes in Chapter 7.

5.3.4 Off diagonal elements using an ancilla.

Evaluating off diagonal elements χ_{ab} requires a different strategy that at first sight seems to be rather different than the one used for diagonal coefficients. However, the main point in this strategy, again, is to realize that any off diagonal coefficient χ_{ab} is related with the average fidelity of the map $\mathcal{E}_{ab}$. This map is not completely positive but can be obtained as the difference between two completely positive maps.. For this reason, as shown in [BPP09], the off diagonal coefficients can be obtained as the mean value of an ancillary qubit conditioned to the survival of the state $|\phi_j\rangle$ and averaged over the 2–design. Using control and anti-control gates connecting ancilla and system[NC00] the desired evolution can be obtained. The complete algorithm can be applied with the following circuit

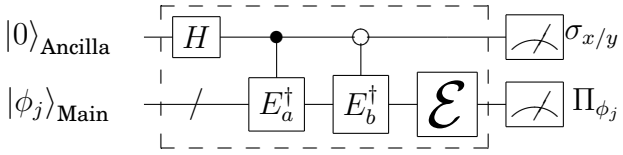

Real and imaginary parts of χ_{ab} are obtained by conditionally measuring the mean values of σ_x and σ_y of an ancillary qubit that interacts with the system with controlled $E_{a,b}$ operations. In fact, it is straight forward to see that the state just before measurement is

$$\begin{aligned}\rho_f = \ & \tfrac{1}{2} \ \Big(|0\rangle\langle 0| \otimes E_b |\psi\rangle\langle\psi| E_b^\dagger + \\ & + \ |0\rangle\langle 1| \otimes E_b |\psi\rangle\langle\psi| E_a^\dagger + \\ & + \ |1\rangle\langle 0| \otimes E_a |\psi\rangle\langle\psi| E_b^\dagger + \\ & + \ |1\rangle\langle 1| \otimes E_a |\psi\rangle\langle\psi| E_a^\dagger \Big) .\end{aligned} \tag{5.15}$$

so that by measuring the mean value of σ_x and σ_y conditioned to the survival of the state $|\psi\rangle$ one obtains the real and imaginary values of the χ matrix elements.

$$\begin{aligned} \int \mathsf{tr}(\rho_f\,(\sigma_x \otimes |\psi\rangle\,\langle\psi|))d\psi &= \frac{D\mathbf{Re}\,(\chi_{ab}) + \delta_{ab}}{D+1} \\ \int \mathsf{tr}(\rho_f\,(\sigma_y \otimes\ |\psi\rangle\,\langle\psi|))d\psi &= \frac{D\mathbf{Im}\,(\chi_{ab})}{D+1}. \end{aligned} \tag{5.16}$$

This method allows to estimate any χ matrix element with a fixed precision but uses an extra ancillary clean qubit. That is, a qubit which one must be able to prepare and measure well and which suffers from almost no decoherence. This is normally a strong restriction for not only this qubit has to be clean but it must be able to interact in a controlled fashion with all the other qubits.

The first experiment done and presented in Chapter 6 uses this method. Following, a newer method in which the ancilla qubit can be removed was developed and tested in the laboratory. These later experimental results are detailed in Chapter 7.

5.3.5 Off diagonal elements without an ancilla.

There is another way to surpass the obstacle that $\mathcal{E}_{ab}$ is not a physical map. Again the idea is established by noticing that it can be obtained as the difference between two CP maps. The efficient estimation of the real part of χ_{ab} can be obtained by exploiting a connection between the real part of F_{ab} and some new fidelities $F_{ab}^{\pm}$ of two efficiently obtainable completely positive maps defined as:

$$F_{ab}^{\pm} = \sum_j \langle\phi_j|\mathcal{E}(\{E_a \pm E_b\}^\dagger|\phi_j\rangle\langle\phi_j|\{E_a \pm E_b\})|\phi_j\rangle. \tag{5.17}$$

The desired real part of the fidelity is obtained by measuring $F_{ab}^{\pm}$ and using that $2Re(F_{ab}) = F_{ab}^{+} - F_{ab}^{-}$. For the imaginary part of an off-diagonal element, a slight modification of the real part scheme does the job. First, we one must consider the following two completely positive channels:

$$\tilde{F}_{ab}^{\pm} = \sum_j \langle\phi_j|\mathcal{E}(\{E_a \pm iE_b\}^\dagger|\phi_j\rangle\langle\phi_j|\{E_a \pm iE_b\})|\phi_j\rangle. \tag{5.18}$$

Then it is straightforward to obtain the imaginary part of one of the fidelities from equation 1 by measuring $\tilde{F}_{ab}^{\pm}$ and considering $2Im(\tilde{F}_{ab}) = \tilde{F}_{ab}^{+} - \tilde{F}_{ab}^{-}$.

The estimation of F_{ab} can then be done by measuring the above channels. The procedure can be summarized in a couple of steps. 1) Randomly choose an element of the 2–design $|\phi_j\rangle$; 2) Prepare the state obtained by acting with $(E_a \pm E_b)^\dagger$ on the state chosen in the first step; 3) Apply the channel $\mathcal{E}$ to the resulting state; 4) Estimate the probability to detect $|\phi_j\rangle$ as the output state. By repeating this process M times one estimates $F_{ab}^{\pm}$ with an accuracy scaling as $1/\sqrt{M}$. The $\tilde{F}_{ab}^{\pm}$ values can be estimated in a similar fashion.

The above steps are applicable because both the states of the 2–design, $|\phi_j\rangle$ and the states obtained by acting with $(E_a \pm (i)E_b)^\dagger$ on $|\phi_j\rangle$ can be efficiently prepared and detected.

Efficient state preparation

One needs to prepare states of the form $(E_a + e^{i\beta}E_b)|\phi_i^{(\alpha)}\rangle$, where β is a multiple of $\pi/2$ (odd multiples are required for the measurement of the imaginary part of χ_{ab}) and $|\phi_i^{(\alpha)}\rangle$ is one of the states from the 2–design. To do this, one must first fix an ordering of the states within each basis. On the computational basis ($\alpha = 0$), it is convenient to choose lexicographic ordering. For any other basis we will use the convention $|\phi_i^\alpha\rangle = V_0^\alpha |\phi_i^\alpha\rangle$, where V_0^α is the corresponding change of basis operator which is described in detail in[BPP08, BPP09]. The states one must prepare are then of the form

$$\left(E_a + e^{i\beta}E_b\right) V_0^\alpha X^{(i)} \left|\phi_0^{(0)}\right\rangle \tag{5.19}$$

where $\left|\phi_0^{(0)}\right\rangle$ is the vector of the computational basis that has all zeros and $X^{(i)}$ is an operator that has X on each qubit where the binary decomposition of i has a one[1].

Since V_0^α is a Clifford group operator it can be built with $O(n^2)$ Hadamard, CNOT and phase gates. That is, with resources scaling polynomially with the number of qubits. As shown in [BPP08] it is efficient to compute how E_a and E_b transform into $\tilde{E}_a$ and $\tilde{E}_b$ under conjugation via V_0^α. This yields:

$$V_0^\alpha \left(\tilde{E}_a X^{(i)} + e^{i\beta}\tilde{E}_b X^{(i)}\right) \left|\phi_0^{(0)}\right\rangle. \tag{5.20}$$

And since the application of a Pauli operator on a computational basis state yields another state from that basis, the required state can be restated as

$$V_0^\alpha(\left|\phi_m^0\right\rangle + e^{i\gamma}\left|\phi_n^0\right\rangle) \tag{5.21}$$

which is the change of basis circuit acting on a state that is efficiently prepared via a Hadamard gate, $O(n)$ CNOT gates and at most three phase gates. The normalization constant is readily obtained from (5.21) as the norm of the state prior to the application of the change of basis.

5.4 More tools for Experimental Quantum Process tomography.

This section presents some useful tools for analyzing quantum process tomography data. The first two subsections deal with issues regarding imperfect channel reconstruction due to inherent or systematic statistical errors. The last three subsections present three tools which are used to characterize channels. All of these tools were used in the experiments of this thesis.

5.4.1 Positivity and Complete Positivity

Any map describing the physical evolution of a system must transform density matrices into density matrices. That is, it must preserve their positivity. Such a

[1]For a reference on this way of writing Pauli operators see [Ben11].

kind of channel is called a *positive channel*. This should also be true if the input state is entangled with some other system not directly affected by the channel. In other words, the most general input state for a general channel is not just a system of the dimension of the channel, but it is all the possible extensions to larger systems of which only one of its parts interacts with the channel. If one wants maps to represent the evolution of physical systems in this more general case then they must be *completely positive*.

Complete positivity and χ matrices

The complete positivity of a quantum channel implies the positivity of its χ matrix. The demonstration of this fact can be done via the connection of the χ matrix representation with the Kraus operator representation[NC00].

Complete positivity and experimental process tomography

Any method of process tomography will determine the parameters characterizing the quantum channel by doing many measurements. The results will invariably be subject to statistical deviations which can be due to the inherent statistical nature of quantum measurement as well as uncontrolled parameters in the laboratory. In any case the information collected will most surely reconstruct a channel which is neither positive nor completely positive.

One may wish to know which is the completely positive map which best represents the measured data. There are many approaches to this problem. One may for example, choose a matrix distance measurement, and find the closest positive matrix to the χ matrix experimentally determined. Or one may diagonalize the χ matrix, erase the negative values in that base and then undo the diagonalization. Or, as it was done to analyze some of the data of the experiments presented in this thesis, one may use the Choi-Jamiołkowski isomorphism[Cho75, Jam72]. One first uses the isomorphism to map the channel into a state and then uses standard state normalization methods. In our case we diagonalized the resulting state, nulled the negative eigenvalues and then transformed back the operation to its representation in the original base. (Alternatively methods such as maxLik (maximum likelihood) could be used[BDPS99].) Finally using the isomorphism again one reconstructs the process obtaining a physical one. Also, to get trace preserving channels when nulling the negative eigenvalues one can normalize them so that they add up to one. Some papers published on this topic are: [Sac01, FH01].

Correction methods as those just mentioned are only useful when one does full process tomography. Actually, when reporting a channel, sometimes it is best not to correct the measured data because the type of method implemented might be better or worse depending on which information one wants to get from the channels determination. However, sometimes one must choose a positive version of the matrix to extract information about it. For example, comparing channels, with the quantity described below (fidelities between channels) one must use positive normalized channels. If one does not do so, then these fidelities could even be bigger than 1!, which is clearly wrong.

5.4.2 Normalization

The same arguments just presented also apply for normalization of a channel. If one is to account for losses, a normalized trace preserving channels should not be expected. However if one wants to give a description of the quantum evolution of a system not considering losses then it is customary to renormalize the reported channel to erase errors due to statistical deviations.

5.4.3 Process Fidelity

As special case of the generalized fidelity, described above, is the average fidelity of a quantum channel $\mathcal{E}$. It is a measure which quantifies how much a channel preserves its input states. It is defined as

$$F(\mathcal{E}) = \int \langle\psi| \mathcal{E}(|\psi\rangle\langle\psi|) |\psi\rangle \, d|\psi\rangle \,, \tag{5.22}$$

where the integration over the Hilbert space is done with the invariant Haar measure[Sam80, Mel90]. It is an average of the overlap between all the possible initial pure states with the final ones.

For processes described with a χ matrix representation, with the convention that $E_0 = I$, the average fidelity can be related to the χ_{00} matrix element[DCEL09]:

$$F(\mathcal{E}) = \frac{D\chi_{00} + 1}{D + 1}. \tag{5.23}$$

5.4.4 Fidelities between channels

A quantity which is very useful in comparing how close two quantum channels $\mathcal{E}_1$ and $\mathcal{E}_2$ are is the fidelity between channels[GLN05, ABJ$^+$03]. Its definition is based on a fidelity measurement for states averaged over all the possible output states given pure input states.

The fidelity between two states can be defined as

$$f[\rho_1, \rho_2] = \left(\mathsf{Tr}(\sqrt{\sqrt{\rho_1}\rho_2\sqrt{\rho_1}}) \right)^2. \tag{5.24}$$

Then the fidelity between channels will be the average over the Haar measure, of this fidelity, for output states corresponding to the same input state

$$F[\mathcal{E}_1, \mathcal{E}_2] = \int f(\mathcal{E}_1(\rho), \mathcal{E}_2(\rho)) \, d|\psi\rangle \,, \tag{5.25}$$

where $\rho = |\psi\rangle\langle\psi|$. It is important to note that for this fidelity to give reasonable values it must be calculated with processes which are completely positive and trace preserving. To do so, on experimental data, it will be crucial to use a normalization mechanism such as those presented in Section 5.4.1.

5.4.5 Quantum Process Identification.

Quantum process identification is one of the key tools which makes SEQPT a useful scalable method. Suppose one is interested in determining how close a given measured process is to a target unitary process $\mathcal{E}^T$. A good measure of such distance is provided by the average fidelity of the channel obtained by composing the inverse target operation $\mathcal{E}^{T^{-1}}$ and the measured channel $\mathcal{E}^M$. In a way, this measure is like a Lochschmidt echo[Per84, PLU95] where one first evolves with the measured channel and then evolves backwards with the inverse of the expected target channel

$$\rho' = \mathcal{E}^{T^{-1}}(\mathcal{E}^M(\rho)). \tag{5.26}$$

The fidelity of this composite channel, as explained above, can be calculated as the average survival probability over the Haar measure:

$$F_{TM} = \int \langle\psi|\, \mathcal{E}^{T^{-1}}(\mathcal{E}^M(|\psi\rangle\langle\psi|))\, |\psi\rangle\, d\,|\psi\rangle \tag{5.27}$$

Using tools explained in Section 5.3 it can be show that if the both $\mathcal{E}^T$ and $\mathcal{E}^M$ are trace preserving channels and if the E_i base used is self adjoint then the above fidelity can be expressed in terms of the χ matrices for each process as

$$F = \frac{D\mathsf{Tr}(\chi^{T^{-1}}\chi^M) + 1}{D+1}. \tag{5.28}$$

Such inverse matrices, $\chi^{T^{-1}}$, can be obtained analytically and are typically small: For example, for the identity channel the only non-vanishing element is $\chi^{T^{-1}}_{00} = 1$. Therefore to estimate the fidelity of the identity we only need to estimate χ^M_{00}. For other more complicated processes one will need to estimate more than one matrix element. For example for a controlled operation such as $U_c = (I - Z) \otimes Z/2 + (I + Z) \otimes X/2$, the $\chi^{T^{-1}}$ matrix has 16 non-vanishing elements (4 diagonal and 12 off-diagonal ones). Therefore, to measure the fidelity to such channel one only needs to estimate 16 elements of the χ–matrix[2].

What is interesting about this idea is that it allows to assert information about channels without the need of knowing the whole χ matrix. This will be a crucial technique in demonstrating the power of a selective and efficient method for quantum process tomography.

[2]This controlled U_c operation was used in one of the experiments presented in this thesis.

Chapter 6

Ancilla Assisted SEQPT

This chapter presents experimental results on ancilla assisted selective efficient quantum process tomography (SEQPT). The results are compared to those obtained with the standard Nielsen and Chuang method. Two one-qubit channels were studied by using the polarization and path qubits of single heralded photons as system and ancilla, respectively. The results show that even for a Hilbert space of such a small dimension the new selective and efficient method can be a better strategy than the standard method. Though full process reconstruction is done more easily with the standard method, if only partial information is required, our method requires far less measurements to assert the value of a given χ matrix element. Moreover, a good estimation of these elements can be done with even less measurements.

Testing this new method with such a small system, where performing the standard method is not a problem, was enlightening for it provided a test to its robustness against systematic and statistical experimental errors in state preparation and detection. It turned out to be that with both methods the full reconstruction of the processes led to very similar results, with fidelities over 95%. This showed that, although state preparation and measurement is more complicated and requires more gates than in the standard method, our new method is fairly robust. As suspected, determining quantities by averaging over states of a 2-design is not very much affected by small experimental errors. This suspicion, which comes from the fact that the states are uniformly distributed over the Hilbert space, should extend to higher dimensions where the method here presented is crucial in the determination of relevant parameters characterizing a quantum channel.

6.1 Experiment

Ancilla assisted selective and efficient quantum process tomography was performed on the polarization qubit of single heralded photons. As the ancilla, the path qubit on the same photon was used. As explained in Chapter 3, this choice enabled performing arbitrary unitary gates deterministically on any of the qubits and, also, applying controlled gates between them. Single heralded photons were generated by parametric down conversion at a non-linear BBO crystal cut for type II phase matching as described in Chapter 4.

The full implementation of ancilla assisted selective and efficient quantum process tomography is schematically represented by the circuit:

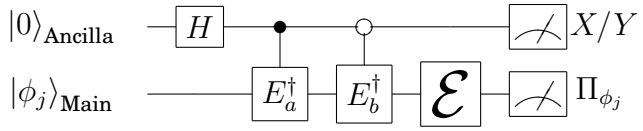

The circuit can be divided into three steps:

1. ***State preparation.*** The initial states belonging to the 2–design $|\psi_j\rangle$ must be prepared. The ancilla initially in the $|0\rangle$ state must be rotated with a Hadamard gate to $H|0\rangle = (|0\rangle + |1\rangle)/\sqrt{2}$. Then the controlled operations $E_a^\dagger$ and $E_b^\dagger$ between ancillary qubit and target qubit must be done. This will prepare an entangled or product state between the ancilla and system qubit depending on $E_a^\dagger$ and $E_b^\dagger$.

2. ***Evolution.*** Irrespective of the ancillary qubit the polarization qubit evolves through the channel $\mathcal{E}$.

3. ***Measurement.*** The mean value of X or Y is measured for the ancilla qubit conditioned on the survival of the $|\psi_j\rangle$ states.

With these steps we implement the algorithm in the photonic setup illustrated in Figure 6.1 and pictured in Figure 6.2. Experimentally the above steps are performed the following way:

1. ***State preparation.*** The heralded photon is filtered with a polarizer and rotated to the a state $|\psi_j\rangle$ from the 2–design with the use of a half and a quarter wave-plate. Then, by placing a non-polarizing 50:50 beam splitter, a Hadamard gate is applied on the path qubit. Finally the controlled operations $E_a^\dagger$ and $E_b^\dagger$ are done with a sequence of quarter-half-quarter wave plates on each path.

2. ***Evolution.*** To make gates that affect equally both paths, the corresponding beams are steered so that they run parallel and close to each other. Then they can be sent though a common process $\mathcal{E}$ affecting the polarization of the photon irrespective of the path. The two channels studied were the identity and unitary gate done by a quarter wave plate at $0°$.

3. ***Measurement.*** Finally, measurement of X or Y in the path qubit is done by interfering both paths at a second non-polarizing beam-splitter with a phase ϕ previously set by tilting a glass on one of the paths. Projection on the desired polarized state is done by a quarter and half wave plate followed by a polarizing beam splitter and detection is done by multi mode fiber coupled avalanche photodiodes.

With this scheme we measure the quantities $p_{ab}(X, \pm; \Pi_{\psi_j})$, which are the probabilities of finding the ancilla in the $\pm$ state of the X basis conditioned on the survival of the input states $|\psi_j\rangle$ for each $\mathcal{E}_{ab}$. Similarly measures in the Y base. These probabilities are then used to obtain all the necessary data to determine the matrix element χ_{ab}. A note must be made about diagonal elements: in this case the scheme simplifies significantly because there is no need for an ancilla qubit so one then can look at only one arm of the interferometer by blocking the other one.

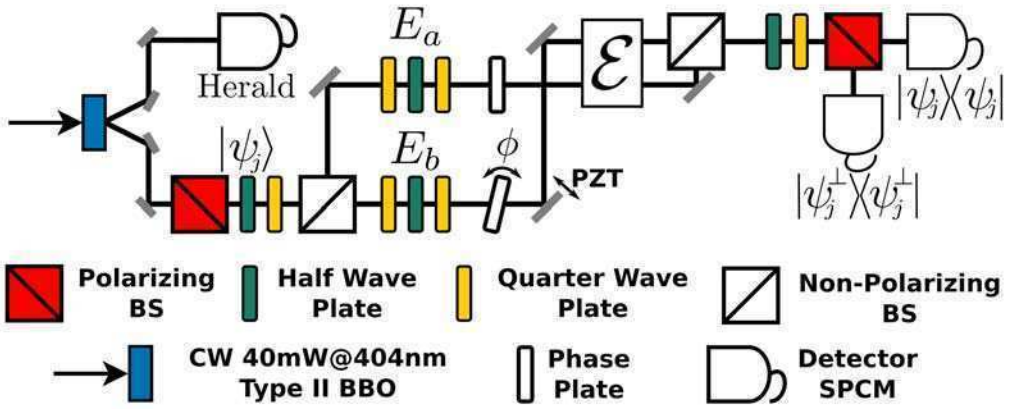

Figure 6.1: **Schematic representation of the experimental setup.** A continuous laser diode at 405nm and 40mW generates frequency degenerate twin photons on a BBO crystal cut for type II parametric down conversion. One photon is used as a herald while on the other a polarization and a path qubit are encoded.

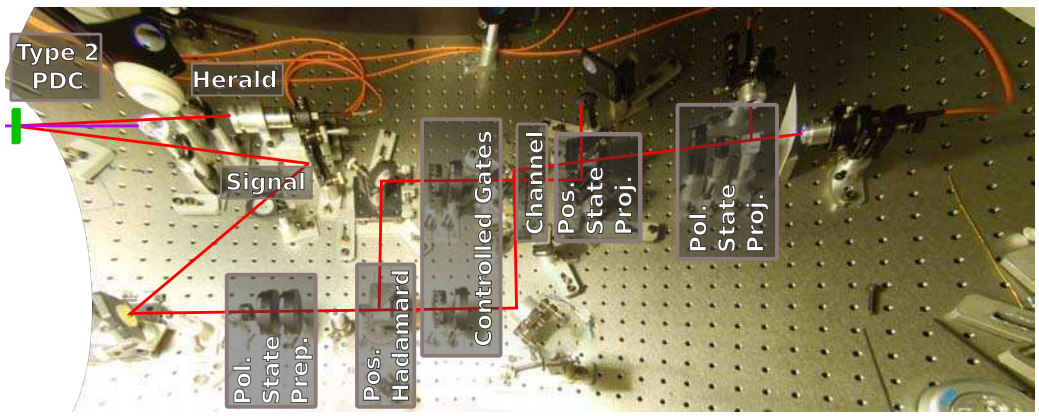

Figure 6.2: **Image of the experimental setup - I.** Pairs of photons are generated at the BBO crystal (green) and travel in the directions indicated by the red lines. Shaded areas indicate the operation performed at each step.

Interferometic Control

The correct performance of the path qubits relies on the control of the interferometer formed between the two non-polarizing beam splitters. The interferometer had an average visibility of 92%. Its stability was actively controlled by a PI loop. An intense beam counter-propagating in the interferometer was used to monitor and actively control the position of one of its mirrors with a piezoelectric disc. A stability of over $\lambda/30$ over all measurements was attained. Figure 6.3 shows the paths of the heralded photons as well as the intense beam used for stabilization. The beam used for stabilization was a portion of the $410nm$ pump beam. A "sider fringe" method was used for stabilization where a pre-set voltage is compared to the signal from the photodiode that monitored the interference signal form the reference beam. This error signal was then filtered by a PI loop which controlled the position of one of the mirrors of the interferometer with the piezoelectric disk. Details of the circuit used are presented in Appendix D.1.

The reference beam also went trough the wave plates used to do the $E_a^\dagger$ and $E_b^\dagger$ controlled gates as well as the channel. One would wish, that a change in the angles of these wave plates or of the channel would not modify the error stabilization signal. To do so the choice of $410nm$ as a stabilization beam was a crucial step. Half wave plates for the signal photons ($810nm$) are full wave plates for the reference beam ($410nm$), so they pose no problem. On the contrary, quarter wave plates act on the reference beam as half wave plates rotating its polarization. However there were only a couple of combination of these angles needed to do do all the relevant gates and the interferometers position could be re-calibrated for a change in these by monitoring a known reference input state. Then all other input states were measured with reference to this first one.

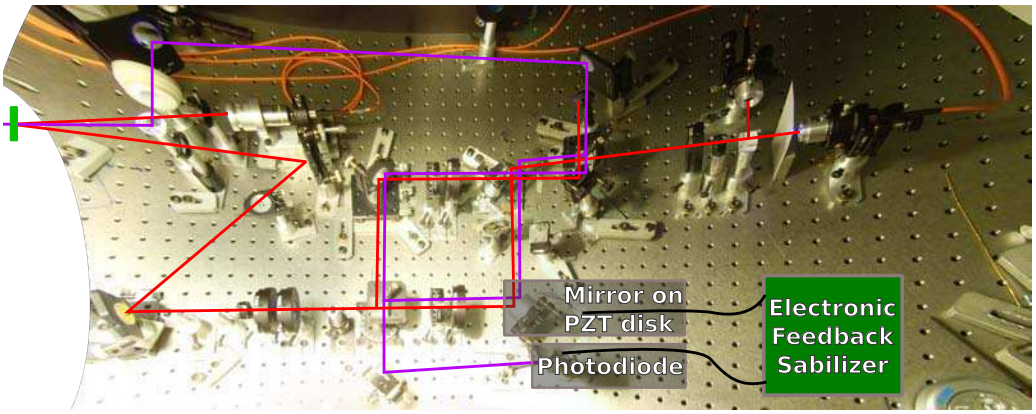

Figure 6.3: **Image of the experimental setup - II.** Indicated is the path of the heralded photons (red) and the path of the pump beam which is used for stabilization by a servo mechanism which controls the position of a mirror mounted on a piezoelectric disc.

Normalization

Overall photon generation and collection efficiencies vary slowly in time due to thermal and mechanical fluctuations. One must constantly normalize the probabilities measured. To do so, as indicated in Figure 6.1 we simultaneously measured both polarization projections. To normalize the measurements of the path qubit one should also measure both exits from the interferometer. This was not done due to lack of extra detectors and fiber collimating optics. To compensate for this lack we did the complementary measurement on the path qubit by adding a π phase on the interferometer by tilting the control glass plate. The measurements were done sequentially to avoid as much as possible long term fluctuations. Measurements had integration times of $15s$ and photon counts did not vary significantly over a period of a couple of minutes so this approach was found effective.

One qubit 2-designs

For the case of a single qubit it turns out that the 2-design is formed by the $D(D+1) = 6$ eigenstates of the three Pauli operators (which define three mutually unbiased bases). For the polarization of photons these are: two states with

vertical-horizontal polarization, two with diagonal (45-135 degrees) polarization and two with circular (right-left) polarization. The generation and detection of such states is done with the standard polarizer, half and quarter wave plate configuration. Applying the controlled gates of the algorithm is conceptually simple. One must apply the four Pauli gates I, X, Y, Z one one path or the other one after the photon is split by the first non-polarizing beam-splitter, which acts as the Hadamard gate in the ancillary qubit. This way the necessary gates can be done by rotating independently the polarization in each path using a quarter-half-quarter wave plate configuration as described in Chapter 3.

Nielsen and Chuang QPT

To perform process tomography by the standard method only some of the optical elements in the setup were needed. The polarization state preparation wave plates were used to prepare the states H,V,D,R. Then state tomography was performed on these states by projecting the outcome into the same set of states. This was done with the last quarter and half wave plate followed by the polarizing beam splitter and the detectors. Process tomography this way involves preparing 4 states and making 4 projective measurements for each preparation: a total of 16 measurements.

As the method does not require ancillas the path qubit was not important. However, to compare faithfully both methods the same experimental setup was used. Several possible combinations were tried, all giving indistinguishable results: i) blocking one of the paths and removing the wave plates inside the interferometer, ii) blocking one of the paths and setting the wave plates inside the interferometer to do the identity gate and iii) not blocking any path, setting the gates to do the identity and stabilizing the interferometer to transmit all photons. The results presented were taken with the last option. With that combination higher count rates were achieved making measurement time shorter.

6.2 Results

6.2.1 Full Process Reconstruction

The elements of χ_{ab} were detected for two different noisy processes affecting the polarization degree of freedom. The results are shown in Figure 6.4. It must be stressed that, although all the matrix elements characterizing both channels were measured, with the SEQPT method one can determine any χ_{ab} selectively and efficiently. This is not the case with the Nielsen and Chuang method where one must fully characterize the channel in order to determine a single χ_{ab} coefficient.

The measured processes correspond to the identity channel (i.e., free propagation through air) and to a quarter wave plate at 0°. Those processes were also fully characterized by means of the standard method of QPT. The results obtained by both methods are compared in Figure 6.4 and turn out to be in very good agreement. As a Figure of merit to compare both schemes we numerically calculate the fidelity between channels determined by each method, obtaining $F = 95,1\% \pm 1.5\%$

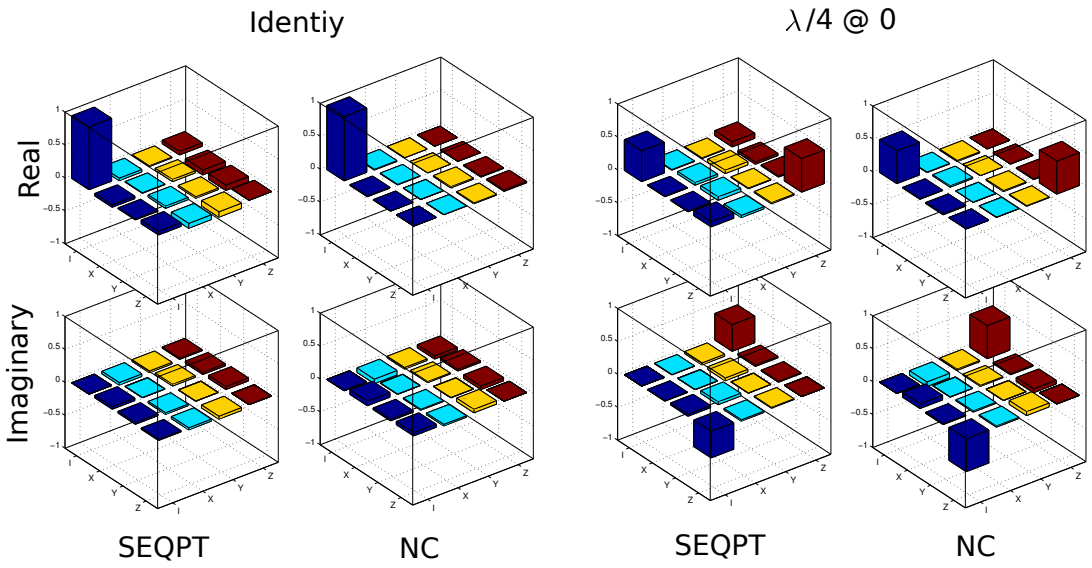

Figure 6.4: **Experimental results.** Results for SEQPT and standard Nielsen and Chuang (NC) process tomography are shown. The first row displays measured real part of the matrix χ_{ab}. The first two columns correspond to the characterization of the process corresponding to free propagation (identity channel) for both methods. Similarly the last two columns correspond to the matrix χ_{ab} measured for a process corresponding to a QWP at $0°$.

for the identity and $F = 96,3\% \pm 1.6\%$ for the half wave-plate at $0°$ The maximum fidelity attainable is mainly limited by interferometer visibility, which results in a not perfectly clean ancilla.

It is interesting to see that, although the visibility of the interferometer is 92% on average, we determine the whole channel with higher overall fidelities. This happened because in the determination of diagonal elements we avoided the unnecessary interferometer normalization step. By doing this, one has an effective visibility for these measurements of 100%. This explains why the measured fidelities are higher than the real interferometer visibility.

6.2.2 Single Element Extraction

SEQPT is a method that is suited to perform partial process tomography selecting the relevant parameters one wants to estimate and investing polynomial resources for such estimation. It is interesting to compare the resources required to implement this new tomographic method and previously existing ones. To do so we analyzed its performance on estimating single elements. To determine any single matrix element χ_{ab} using SEQPT, we measured $D(D+1) = 6$ survival probabilities. On the contrary, obtaining a single matrix element χ_{ab} using the standard QPT [NC00] requires estimating $D^2 \times D^2 = 16$ transition probabilities. This implies that even at the level of a single qubit the SEQPT is more "efficient". This comparison might seem somewhat unfair since after such number of experiments the standard method provides all the information required to estimate the full χ_{ab}

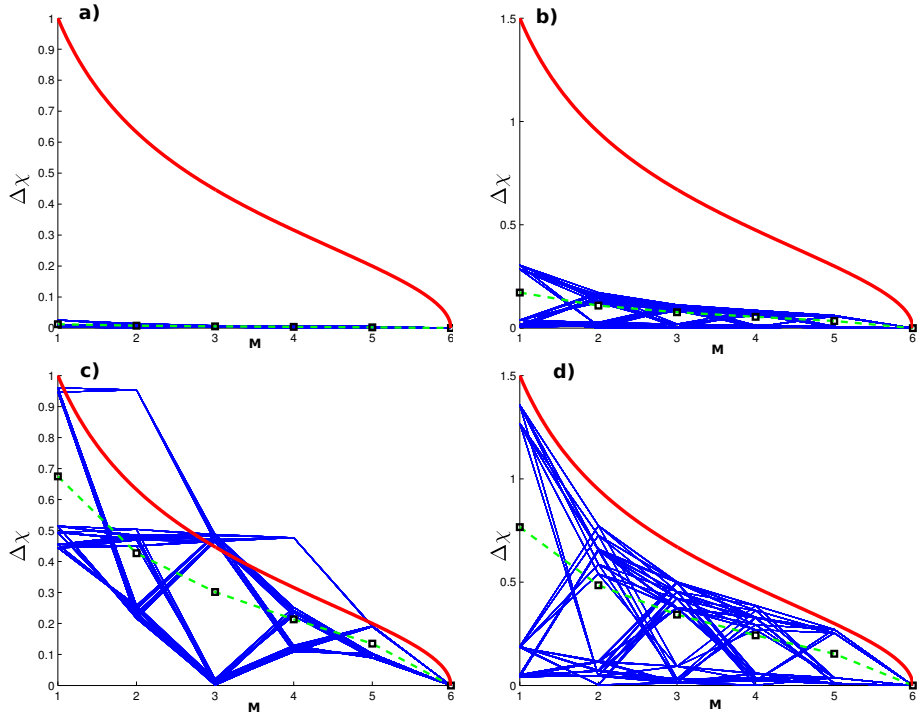

Figure 6.5: **Convergence for the chi matrix elements**. Shown are the errors in the estimation of some selected χ_{ab} the identity measured process. Panels show the error in the estimation of a) χ_{44}, b) χ_{43}, c) χ_{11}, d) χ_{12}. Each blue curve shows the error made in the estimation for each χ_{ab} if only M measurements were made. All possible choices of the first M states are plotted and they lie below the maximum theoretical bound (red curves) for all cases. Also shown in green dashed lines are the actual calculated estimation of the distribution.

matrix and not just a single element of such matrix. However, when working with larger system one would not measure the exact matrix elements χ_{ab} by performing the average over the entire 2-design but instead would only randomly choose M of these states and estimate the result with an error of the order of $1/\sqrt{M}$. In fact, sampling over the whole 2-design will always be exponentially hard (as the 2-design is a set containing an exponentially large number of elements). The main virtue of SEQPT is that it enables us to estimate any element with fixed accuracy by performing a number of measurements that only depends on such accuracy and is independent on the number of qubits.

As described in Chapter 5.3 the error in the estimation of the average after M experiments scales as $\Delta\chi \propto \sqrt{\frac{1}{M}(1-\frac{M-1}{K-1})}$ where $K = D(D+1)$ is the number of elements in the 2-design. With the experimental data at hand we tested the behavior of the estimation error. Using the raw data we split the 2-design in random samples of different (variable) size and computed the average over each of such samples. The results are shown in Figure 6.5. The behavior of the estimation error for the matrix element χ_{ab} obtained by sampling the 2–design in groups of increasing number of states (the size of the sample, M grows up to $K = D(D+1) = 6$, which is the cardinal of the 2–design). The panels show the theoretical curve of the maximum

error expected: a) and c) for diagonal elements and b) and d) for a non-diagonal elements. The bounds are different because of the δ_{ab} in the formula relating measurements and χ matrix elements: $\int \mathrm{tr}(\rho_f\,(\sigma_x \otimes |\psi\rangle\langle\psi|))d\psi = D(\mathrm{Re}(\chi_{ab})+\delta_{ab})/(D+1)$. So for diagonal elements the maximum error is 1 while for off diagonal the maximum value is 1.5.

As shown for two example cases in sub-panels a) and c) of Figure 6.5, the bound is statistically satisfied. Some possible paths lie outside the bound. The average on all the possible paths, however, gives a value which is within the bound.

Surprisingly it was found that for off-diagonal elements all possible errors on all possible choices of sample partitions lie below the analytical bound. This is exemplified with two cases in Figure 6.5 sub-panels b) and d). This is not expected for all possible random distributions, but the ones realized in the experiment strictly satisfy the bound. In fact, it is not hard to imagine possible values for the results of the experiment that would violate the bound for certain samples, but hold to it at the statistical level. However, such cases are not realized in the experiment, which suggests that it would be possible to find a tighter bound.

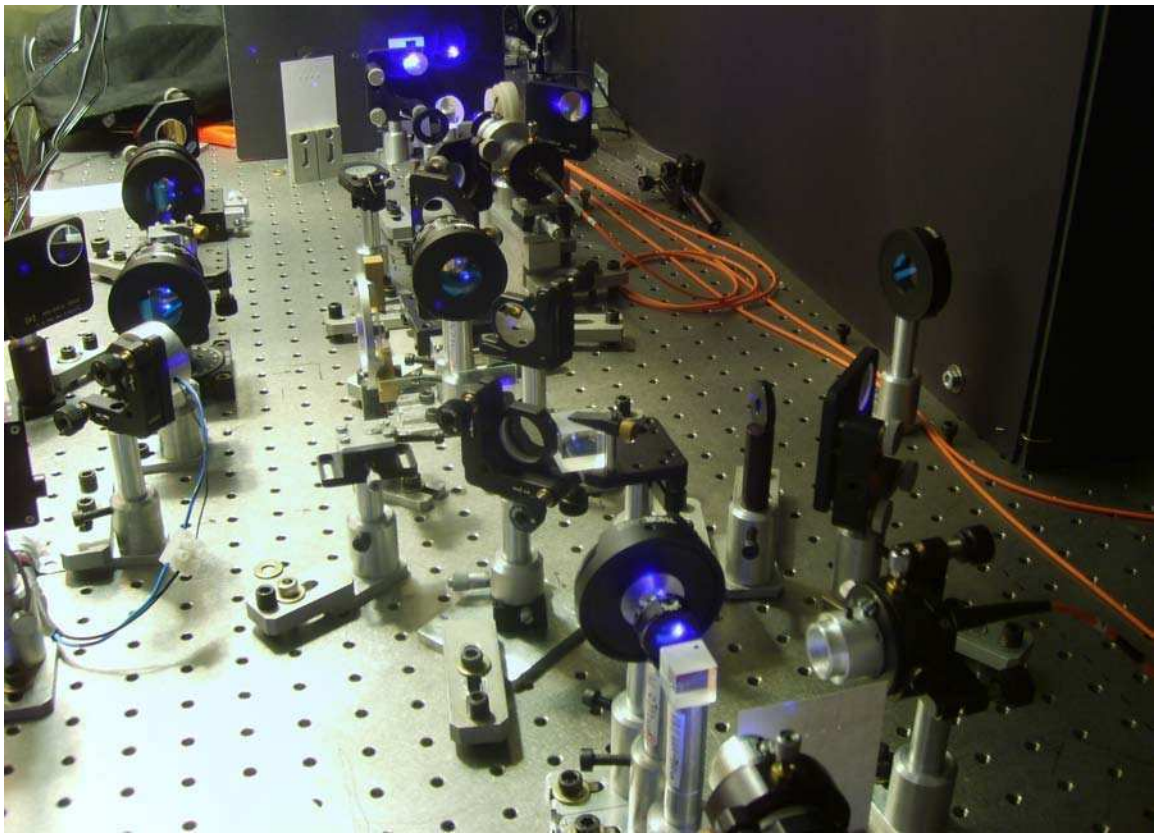

Figure 6.6: **Perspective image of the experiment**.

Chapter 7

Ancilla-less SEQPT

This chapter presents the experimental results on ancilla-less selective efficient quantum process tomography. Experiments were performed on a two qubit system composed of the polarization and path of a same heralded single photon.

Eliminating the need of a clean ancilla qubit is a crucial step in the development of a feasible quantum process tomography scheme. Having an extra clean qubit is normally such a difficult task that renders ancilla-dependent schemes unpractical in real situations. Quantum systems are very prone to interaction with their environment. Much of the effort in QPT is actually to be able to characterize and control these decoherence mechanisms. Relying, then, on a clean qubit is not a wise strategy. Moreover, experimentalists are currently trying to push the control of quantum systems above a few qubits, so adding an extra qubit which has to be able to interact with all the other ones is, most of the times, prohibitively difficult.

Two similar but different strategies were tested. One by which only the the diagonal elements of the χ matrix are extracted and another one by which any element can be found. For the channels studied all possible accessible information from the χ matrix was measured. When working with larger systems one would not do so. With larger systems two global strategies could be suitable depending on the amount of prior information available.

- ***No information.*** If one had no prior information about the channel one can proceed by first using the diagonal scheme to determine the largest diagonal elements[BPP08, BPP09]. Then one would use the full scheme to determine the values of the off-diagonal elements corresponding to diagonal elements that are larger than a desired bound[LBPC10].

- ***Some information.*** If one had some prior information about the channel then one might only need to check some χ matrix elements to confirm or not whether one has that channel or not. Or, for example, if certain decoherence mechanism is present or not.

For all processes studied, standard Nielsen and Chuang process tomography was also done. Measured fidelities between both determinations were above 90%. They were limited mainly to long term statistical errors in the interferometric setup. The whole determination of a process by both methods took about 8 to 10 hours. During this time the interferometers had to be realigned every hour or so

and every calibration was not exactly equal to the one before, smearing out the results. Even, if the same process was determined twice on different days by the same method, the results varied within a few percentage.

The four procesess studied were: the identity gate; a half wave plate on polarization and nothing on path; a controlled gate where the polarization was rotated depending on the path; and this last gate again but with random noise on the path qubit.

7.1 Experimental Setup

To perform both methods of ancilla-less selective and efficient quantum process tomography for 2 qubit processes the same experimental setup was used. In essence the experimental setup allows preparing and measuring a general set of states. In particular it allows preparing all the necessary states of the 2-designs and their associated rotations needed for full ancilla-less SEQPT.

To prepare and measure states a symmetric configuration with three programmable gates was constructed. State preparation is done by a combination of a general rotation U_1 on one of the qubits, followed by a controlled gate U_2 and a final rotation U_3 on the other qubit. Then the channel is applied and it is followed by an identical set of gates U_4, U_5 and U_6 which do the last transformation which sets the measurement basis. Schematically this can be represented as the circuit.

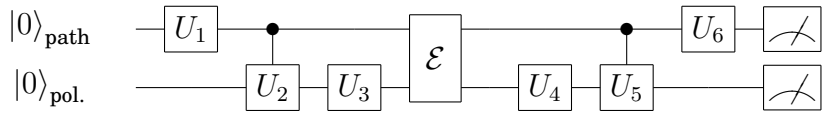

Gates U_1, U_3 , U_4 and U_6 are arbitrary unitary gates, but controlled gates U_2 and U_4 were simpler and only admitted real controlled rotations. This last choice was not due to a limit imposed by the experimental design but a simplification that was done because, in general, this set of gates can actually prepare any state of the Hilbert space starting from the $|0\rangle$ state.[1]

Experimentally this circuit was achieved on the polarization and path of single photons by a combination of interferometers and wave plates. Controlled operations are done with wave plates at different angles on each path. By appropriately combining a self-stable Sagnac interferometer, phase plates and wave plates we can prepare any desired state and measure any of the states of the 2–design as required [EKW01]. Polarization qubits are controlled with several wave plates while path qubits are controlled by three interferometers. Figure 7.1 shows a sketch of the setup and the circuit equivalence of each part.

- U_1. The first U_1 rotation is performed by controlling the phases of two paths inside and at the output of a Sagnac interferometer. This allows for a general unitary rotation on the path qubit initially in the state $|0_{path}\rangle$.

- U_2. Then polarization is filtered with a couple of polarization beam splitters in each path preparing the state $|0_{pol}\rangle\,|\psi_{path}\rangle$. (This is done at this step and

[1] This is not equivalent to saying that this set of gates can do any arbitrary unitary gate.

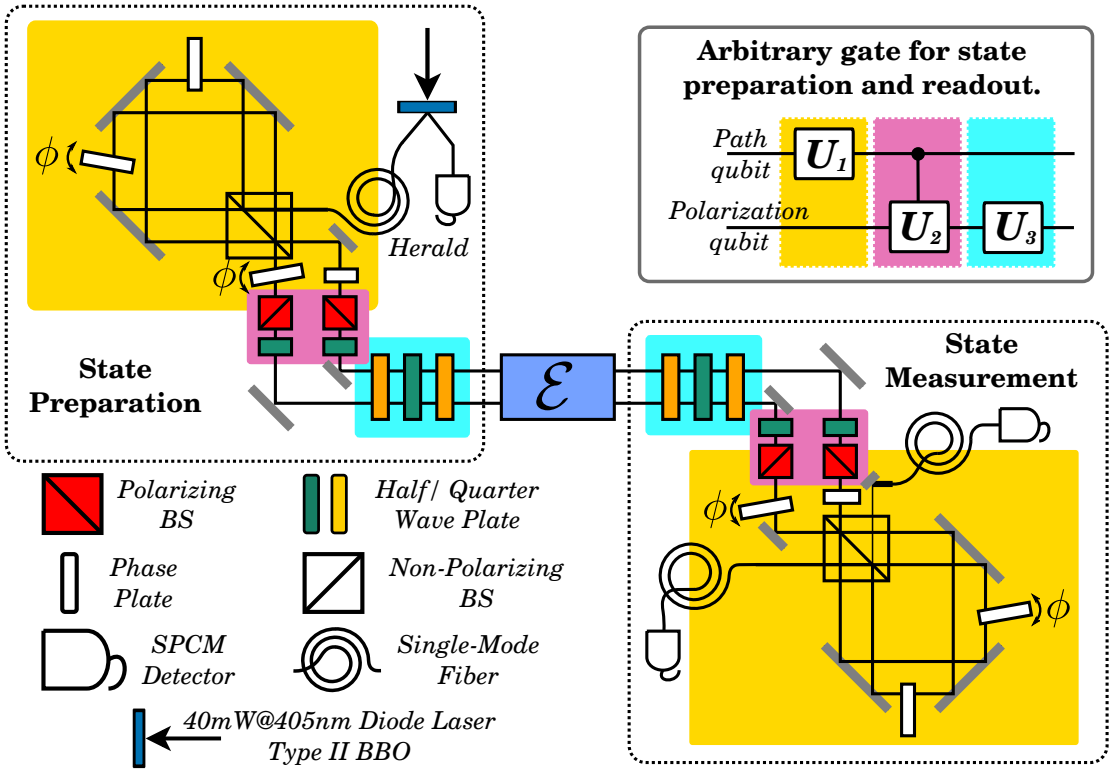

Figure 7.1: **Schematic experimental setup.** Single $810nm$ heralded photons are generated at a BBO cristal by Type II parametric down conversion. Arbitrary states are prepared and measured with a combination of single qubit unitary gates and a controlled operation as exemplified in the inset, colors show the correspondence between circuit and physical implementation. Path-qubit unitary gates are controlled with phase plates and Sagnac interferometers. Polarization-qubit unitary gates are achieved with a combination of wave plates affecting both paths. A controlled operation with control on path and target in polarization is implemented with wave plates at different angles in each path. The different processes studied were set up in the zone marked as $\mathcal{E}$. Single-Mode fibers clean the photon's spatial mode ensuring good interferometer visibility ($\approx 98\%$ in the Sagnacs and $\approx 94\%$ in the Mach-Zehnder). Not shown in the Figure is the Mach-Zehnder's active phase-sensitive stabilization mechanism.

not before to eliminate possible imperfections in the polarization due to slight off plane reflections in the Sagnac interferometer.) The controlled U_2 gate is then done by a couple of quarter wave plates which rotate the polarization of each path independently.

- U_3. Both paths are then steered close and parallel to each other so that by means of a combination of a common set of quarter-half-quarter wave plates the arbitrary U_3 gate is done on the polarization qubit.

- $\mathcal{E}$. The process is then done by placing wave plates either on one path or on both depending on which kind of process one wants to study.

- U_4, U_5 and U_6. Are done in a symmetric way as the first three gates. (Again, polarization is filtered before the Sagnac interferometer to avoid off plane reflection errors.)

- Measurement. Photons are coupled into single mode fibers and sent to avalanche photon counting diodes. Both outputs of the interferometer are continuously monitored. To project into both output polarizations, the last set of half wave plates are rotated to allow either H or V polarization to pass through the last polarizing beam splitters.

Interferometric Control

The Sagnac interferometers used in state preparation and measurement needed no active stabilization. Their robust design allowed for hours of continuous operation without need of readjustment. When filtering input and output modes with single mode fibers, visibilities of above 98% were obtained in the Sagnac interferometers. The tricky part of the interferometric setup of this experiment is the Mach-Zehnder interferometer that holds the controlled gates, the polarization unitary gates and the process. It connects the initial and final Sangac interferometers and has arms of more than 1 meter in length and several optical elements in each on of them. The visibility of this interferometer was of about 94%. Thermal and mechanical fluctuations were controlled by an active stabilization loop which worked with a lock-in method.

To avoid the problems associated with "sider fringe" stabilization used in the ancilla assisted SEQPT (see section 6.1) in this second experiment the technique was improved by implementing a phase loop lock method. This allowed to lock to a maximum of the reference interference signal which did not depend on the overall error signal amplitude. In this experiment this new stabilization technique was crucial since the error signal's amplitude varied a lot as a function of the wave plates angles.

The lock-in technique, described in detail in Appendix D.2, consisted in continuously beating the piezoelectric transducer with a small amplitude at a frequency of about $2kHz$. Then photodiode's signal was compared in a phase sensitive circuit to the reference modulation signal, producing an error signal proportional to the phase difference between these two. This signal was then sent to a PI loop which controlled the mean position of the mirror on the piezoelectric transducer. In a last

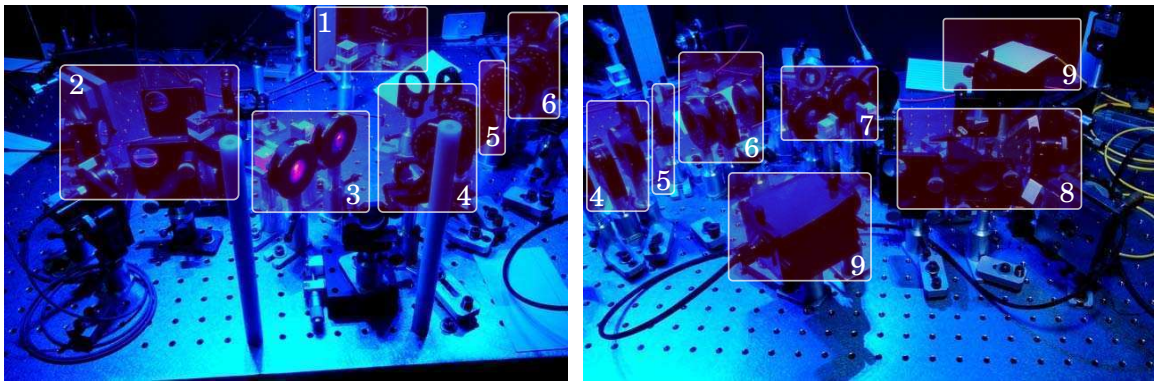

Figure 7.2: **Image of experimental setup**. Pictures overlap repeating parts of the experiment. In 1) the state $|00\rangle$ is prepared. Heralded photons are decoupled from a fiber and polarization is filtered with a polarizing beam splitter. Then in 2) the Sagnac interferometer performs an arbitrary rotation on the path qubit. At the output of the Sagnac interferometer polarization is filtered again to correct possible errors due to off-plane reflections. A controlled-path target-polarization gate is applied in 3) with a half wave plate in each path. Paths are then steered close together and in 4) an arbitrary rotation on the polarization qubits is made with a combination of quarter half and quarter wave plates. These first four steps are used to prepare the desired input state. In 5) the process is placed; a couple of holders, which were used to place plates for different processes studied are seen close but out of place. Then 6), 7) and 8) repeat the structure of 4), 3) and 2) but in inverse order to project the state into the desired measurement basis. 3), 4), 5), 6) and 7) lie inside the Mach-Zehnder interferometer which is actively stabilized. In 9 the photons are collimated into single mode fibers and sent to APD detectors.

stage the modulation signal is added to the mean control signal. The interferometer was then stabilized to its maximum with modulation of less than $\lambda/25$ for the signal photons.

Nielsen and Chuang QPT

To implement the Standard Nielsen and Chuang Quantum Process tomography we prepared the product states of the polarization and path qubits having all the combinations of H,V,D,R for each qubit[2] and then perform quantum state tomography by projecting into these same states. In total this accounts for 16 input states and 16 projective measurements on each input state. That is, a total of 256 measurements.

Of the above depicted experimental setup only, some of the optical elements are needed for this type of process tomography. In particular, the controlled gates, which are implemented with different wave plates in each path, are not needed for only product states must be prepared. Also, only the last two wave plates before the process and the first two after are enough to prepare and measure all the input

[2]As explained before, we abuse the H,V,D,R notation denoting polarization states to indicate the corresponding states of the path qubit.

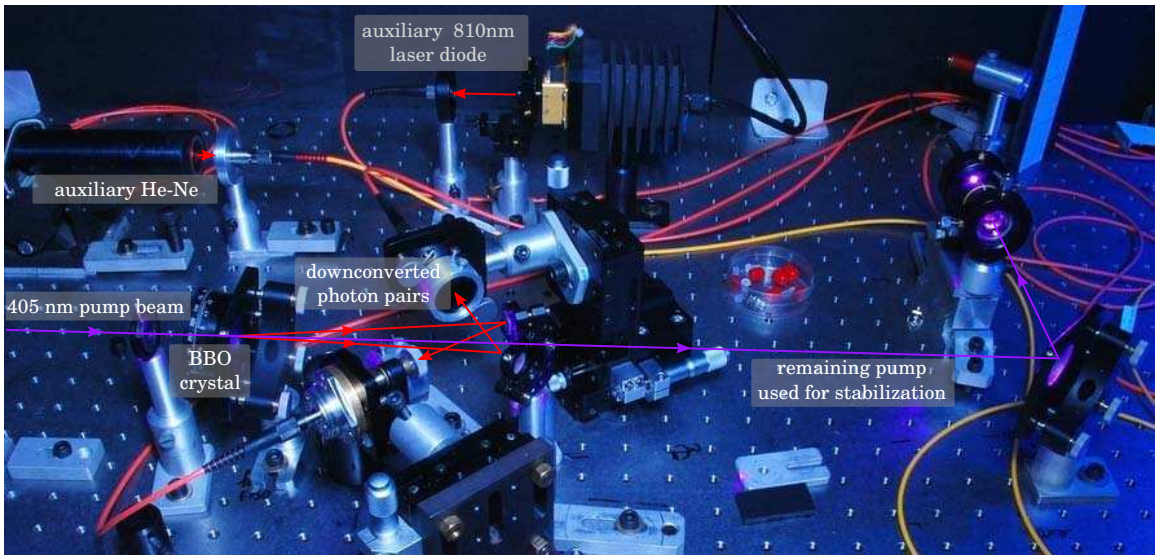

Figure 7.3: **Light sources.** Fiber coupled light sources used for this experiment. Bottom right is the BBO crystal and two fiber couplers to collimate the signal and herald photons into optical fibers. The remaining pump beam is also fiber coupled and sent to the experiment for interferometer stabilization. A He-Ne and a $810nm$ diode laser, used as axillary light sources, were also fiber coupled. The He-Ne light was used mainly for pre-aligning. The diode laser was used for path difference compensation, wave plate calibration, final interferometer alignment, fiber coupling optimization, etc.

and output states.

State tomography post processing was done with the use of Matlab routines provided by the Kwiat group [AJK] while the subsequent process tomography post processing was done with new Matlab routines developed for this experiment following the outline presented in [WGP+07].

7.1.1 Diagonal Efficient Quantum Process Tomography

Form an experimental point of view it is important to specify how to prepare and measure any of the states to perform diagonal quantum process tomography. In particular we should be able to prepare an arbitrary state in an arbitrary basis belonging to a MUB and measure its transition probability to any other states of the same basis. Preparing and measuring in an arbitrary MUB requires some consideration. In this Section the generalities on how to do it for any number of qubits as well as the details on how to do it for two qubits are presented.

It is normally easy to prepare states in the computational basis, which is formed by vectors $\left|\psi_i^{Z\cdots Z}\right\rangle$ (eigenstates of the Z Pauli operator for each qubit). One needs to be able to transform these states into any other MUB. That is, one needs to find operators V_k such that $V_k \left|\psi_i^{ZZ\cdots Z}\right\rangle = \left|\psi_i^k\right\rangle$. Constructive (and efficient) ways of doing so exist[Dan05, Ben06]. With this in mind, the circuit for diagonal process tomography presented in Chapter 5.3 can be mapped into an experimentally feasible one as:

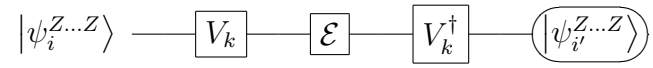

The V_k operators rotate the states from the computational basis to a basis k. Then initial preparation and measurement is then done in the computational basis which is what one normally does in an experiment.

With the above circuit in mind, the steps required for selective quantum process tomography to obtain the specific diagonal element χ_{mm}, with an error smaller than $1/\sqrt{M}$, are as follows:

1. Randomly choose M out of the $D(D+1)$ pairs of states such that $\left|\left\langle\psi_{i'}^k\right| E_m \left|\psi_i^k\right\rangle\right| = 1$ is satisfied for the E_m that is to be measured.

2. Measure the transition probabilities $p_{i,i'}^k$ for the states previously chosen. This is the probability that the state $\left|\psi_i^{ZZ\cdots Z}\right\rangle$ is prepared and the state $\left|\psi_{i'}^{ZZ\cdots Z}\right\rangle$ is measured when the basis transformation operation is set to V_k.

3. The average transition probability between those measured and prepared is the statistical estimator for the quantity $F_m(\mathcal{E})$ with standard deviation $\frac{1}{\sqrt{M}}$ if the random choosing is done with reposition, or $\Delta F_{ab} \propto \sqrt{\frac{1}{M}\left(1-\frac{M-1}{K-1}\right)}$ if the random choosing is done without reposition.

Two Qubit Case

We implemented this method in an experiment to fully characterize several quantum channels affecting $n = 2$ qubits. As a 2-design we used the $D(D+1) = 20$ eigenstates of $D+1 = 5$ mutually unbiased bases (MUBs). In particular we chose

the three separable bases whose generators are X, Y and Z for each qubit and two entangled ones generated by the operators $\{X\otimes Y, Y\otimes Z\}$ and $\{Y\otimes X, Z\otimes Y\}$. Table 7.1 shows this partition of the Pauli group into five disjoint commuting subgroups. These groups can be defined by their stabilizers which are also shown in the table. The stabilizers of a base are a set of operators which have the states defining the base as eigenstates. The table also includes the operator V_k that rotates the computational basis onto each of the other four bases. In this case, three basis are formed by separable states (eigenstates of X, Y and Z for each qubit) while the other two are entangled and were named Belle and Beau (to distinguish them from the now famous Bell basis: Bell, as opposed to Belle and Beau, is biased with respect to the computational basis).

Basis	**Stabilizers**	**V**
ZZ	ZI, IZ, ZZ	**I**
YY	YI, IY, YY	$R_1^x(\pi/2)R_2^x(\pi/2)$
XX	XI, IX, XX	$R_1^y(-\pi/2)R_2^y(-\pi/2)$
belle	YZ, ZX, XY	$R_2^{(1,1,1)}(2\pi/3)CNOT_{12}H_1$
beau	XZ, ZY, YX	$R_2^{(1,1,1)}(-2\pi/3)CNOT_{12}H_1$

Table 7.1: Mutually unbiased basis, stabilizers and generators for two qubits.

The average fidelity $F_0(\mathcal{E})$ can be determined exactly simply by measuring the survival probability $p_{i,i}^k$ for each of the 20 states of the MUBs. To evaluate the other fidelities one must then find which probabilities $p_{i,i'}^k$ are associated with each fidelity $F_m(\mathcal{E})$ via the relation $\left|\left\langle\psi_{i'}^k\right| E_m \left|\psi_i^k\right\rangle\right| = 1$. For this to be determined it is necessary to find the commutation pattern between the operator E_m and the generators of the k–th basis. Of course, one would need to do this for each of the $d^2 = 16$ operators E_m and for all the generators of the stabilizers associated with the $d+1$ MUBs. The details on how to do this for the two qubit case are presented next.

It is useful to introduce some notation first. The E_m will be numbered in the order they appear in table 7.1 with $E_0 = \mathbf{I}$. So that $E_1 = ZI$, $E_2 = IZ$ and so on up to $E_{15} = YX$. The label i which indicates the state $\left|\psi_i^k\right\rangle$ in a given basis k can also be represented by a binary vector: $i \equiv (i_1, i_0)$ with $i_1, i_0 \in 0, 1$, for example for any basis we have the states $\left|\psi_{0,0}^k\right\rangle$, $\left|\psi_{0,1}^k\right\rangle$, $\left|\psi_{1,0}^k\right\rangle$ and $\left|\psi_{1,1}^k\right\rangle$.

For each Pauli operator E_m there are 20 combinations of values i, i', k such that $\left|\left\langle\psi_{i'}^k\right| E_m \left|\psi_i^k\right\rangle\right| = 1$ is fulfilled. These are the 20 relevant probabilities $p_{i,i'}^k$ that will appear in the expression of each coefficient χ_{mm}. Each operator E_m permutes the states of the k–th basis in a certain way $E_m \left|\psi_i^k\right\rangle = \left|\psi_{i+p}^k\right\rangle$(up to a phase). This implies that equation $\left|\left\langle\psi_{i'}^k\right| E_m \left|\psi_i^k\right\rangle\right| = 1$ will be satisfied when $i + i' = p(mod\ 2)$ so that the permutation pattern induced by the operator E_m can be completely described by the vector $i + i'(mod\ 2)$ which depends only on E_m and k. For example, if one finds that for a given k and a certain E_m the value of $i + i'(mod\ 2)$ is $(0, 0)$, this means that the action of E_m, up to a phase, does not change the vectors in the k–th basis. Accordingly, if $i + i'$ is $(0, 1)$ it means that operator E_m exchanges the first vector $(0, 0)$ with the second $(0, 1)$ and the third $(1, 0)$ with the fourth $(1, 1)$. When the value of $i + i'$ is $(1, 0)$ or $(1, 1)$ the way in which the operator E_m permutes

	E_0	E_1	E_2	E_3	E_4	E_5	E_6	E_7	E_8	E_9	E_{10}	E_{11}	E_{12}	E_{13}	E_{14}	E_{15}
ZZ	0,0	0,0	0,0	0,0	0,1	1,0	1,1	0,1	1,0	1,1	0,1	1,0	1,1	0,1	1,0	1,1
YY	0,0	0,1	1,0	1,1	0,0	0,0	0,0	0,1	1,0	1,1	1,0	1,1	0,1	1,1	0,1	1,0
XX	0,0	0,1	1,0	1,1	0,1	1,0	1,1	0,0	0,0	0,0	1,1	0,1	1,0	1,0	1,1	0,1
Belle	0,0	0,1	1,0	1,1	1,0	1,1	0,1	1,1	0,1	1,0	0,0	0,0	0,0	0,1	1,0	1,1
Beau	0,0	1,1	1,0	0,1	0,1	1,1	1,0	1,0	0,1	1,1	1,1	1,0	0,1	0,0	0,0	0,0

Table 7.2: The values of $i + i'(mod\ 2)$ such that $p^k_{ii'}$ is a probability associated with the Pauli operator E_m for each of the five mutually unbiased bases (which can be labeled with an index k or denoted, as in the Table, with names ZZ, XX, YY, Belle and Beau). Equivalently: the values that $i + i'(mod\ 2)$ must have to satisfy $\left|\left\langle\psi^k_{i'}\right| E_m \left|\psi^k_i\right\rangle\right| = 1$.

the vectors in the basis can be simply deduced in the same way. The values of the $i + i'(mod\ 2)$ for all values of k and for all the operators E_m are given in table 7.2 which is constructed by analyzing the commutation (and anticommutation) pattern of E_m with the generators of the k–th bases.

Using the information in the above table it is then straight forward to see how to calculate any fidelity $F_m(\mathcal{E})$. Suppose wish to calculate it for the Pauli operator $E_2 = IZ$. Then the 20 relevant transition probabilities can read from table 7.2. For such case we have to take into account all transitions that satisfy $i + i' = (0, 0)$ in the computational basis and $i+i' = (1, 0)$ in all the other bases. Also, the procedure early mentioned for the fidelity $F_0(\mathcal{E})$ can be obtained from the table. Finally, in all cases, the corresponding fidelity is calculated as the average of all the transition probabilities associated to the corresponding E_m.

7.1.2 Full efficient selective quantum process tomography.

For full QPT one independently measures the values of χ_{ab} elements. To do so, for each element we prepared the 20 states in the 2-design and measured their survival (and non-survival) probabilities. A simple algorithm to prepare states $(E_a \pm (i)E_b)\left|\phi_j\right\rangle$ was developed.

It is important to use a special 2–design adapted to the basis of operators E_a. We choose E_a as generalized Pauli operators built as n–fold tensor product of the identity I or one of the three Pauli operators (X, Y or Z) on each qubit. These operators form the Pauli group that has D^2 elements (up to phases). This group can be partitioned into $D + 1$ commuting subgroups each of them containing D operators (including the identity), which are obtained as all possible products between n independent generators. Each commuting subgroup defines an orthonormal basis of the Hilbert space, formed by the eigenstates of the operators in the set. These $(D + 1)$ bases are mutually unbiased (MUBs)[BBRV08, LBZ02]. The set of all $D(D + 1)$ states belonging to the $(D+1)$ bases form a 2–design. This is the 2–design we used, and we will denote it as $S = \{|\phi^{(\alpha)}_i\rangle, \alpha = 0, ..., D, i = 1, ..., D\}$. The index α labels the different MUBs and the index i labels each state in each basis. This set of states fulfills the efficiency restrictions needed for this algorithm to be scalable:

1. Any state $|\phi^{(\alpha)}_i\rangle$ can be generated from any computational state (i.e. a joint eigenstate of all Z_i operators) by an efficient quantum circuit[BPP08, BPP09].

2. Any Pauli E_a is such that $E_a|\phi_i^{(\alpha)}\rangle = |\phi_{i'}^{(\alpha)}\rangle$, that is to say, Paulis are translations within each basis. The transition rule, i.e., the expression that determines i' as a function of (i, α, a) can also be efficiently obtained. In fact, such expression depends only on the commutation (or anti-commutation) relations between E_a and the n operators that are chosen as generators of the basis α.

3. Also the normalized state $|\Psi_{\pm,a,b,i}^{(\alpha)}\rangle = K(E_a \pm E_b)|\phi_i^{(\alpha)}\rangle$ can be generated efficiently from any computational state. The simplest way to do that is to prepare first a superposition of appropriately chosen computational states and later apply a change of basis. These tasks can be efficiently performed. The normalization constant K is also efficiently computable.

The calculation of the input and output states was done via specially designed Matlab routines which first calculated the necessary states and then traduced these to angles of wave plates and phase retarders in the experiment.

Full process characterization.

Full characterization of the 256 elements of the χ matrix involves $256 \times 40 = 10240$ transition probabilities. Fortunately many of them coincide and the number of different transition probabilities is much lower. In our case, a full characterization of a two qubit process required only 140 different initial states. Each had to be measured at the output in a certain base giving 4 probabilities. A total of $140 \times 4 = 560$ transition probabilities had to be measured.

It is no surprise that full process tomography requires an exponential number of probability measurements. Just for diagonal tomography, each single coefficient is an average of 20 probabilities. Since there are 16 such coefficients this would require on the order of 320 probability measurements for full diagonal tomography. However, many of these probabilities are repeated. For instance, if we were to measure the diagonal χ coefficients corresponding to the operators $X\otimes X$ and $Y\otimes Y$, it is straightforward to see that both operators acting on the state $\left|\phi_0^{(0)}\right\rangle$ yield the same state, up to a phase. When it comes to off-diagonal tomography, many more of those probabilities are repeated.

Since the χ matrix is defined by $O(D^4)$ real numbers and each each of those requires $O(D^2)$ probabilities to be obtained, it can be seen that full process tomography will require between $O(D^4)$ and $O(D^6)$ probability measurements, both exponential on the number of qubits.

7.2 Results

7.2.1 Diagonal Process Tomography

Diagonal process tomography was performed on two processes: the identity and an X gate on the polarization qubit. The identity gate was done by placing nothing in the zone reserved for the channel. The X gate on the polarization qubit was done by placing a half wave plate at 45° on both paths.

The results, showing the determination of the diagonal χ matrix elements, are displayed in Figure 7.4. This kind of tomography is particularly useful when one knows nothing about a channel. In such a case, if the process is not sparse in the chosen bases, it can be used to determine which are the largest diagonal elements characterizing the process. This, in turn, allows by means of the inequalities formulated by Lopez et. al. [LBPC10] and described in Chaprer 5, to bound the possible values of the off-diagonal elements for completely positive maps. For example, for the identity process shown in the left panel of Figure 7.4 one can assert that the only off diagonal element that could be bigger than 0.15 is the χ_{02} which corresponds to the elements II, IY. Similarly for the X gate on the polarization qubit one can say that no off-diagonal element is bigger than 0.16.

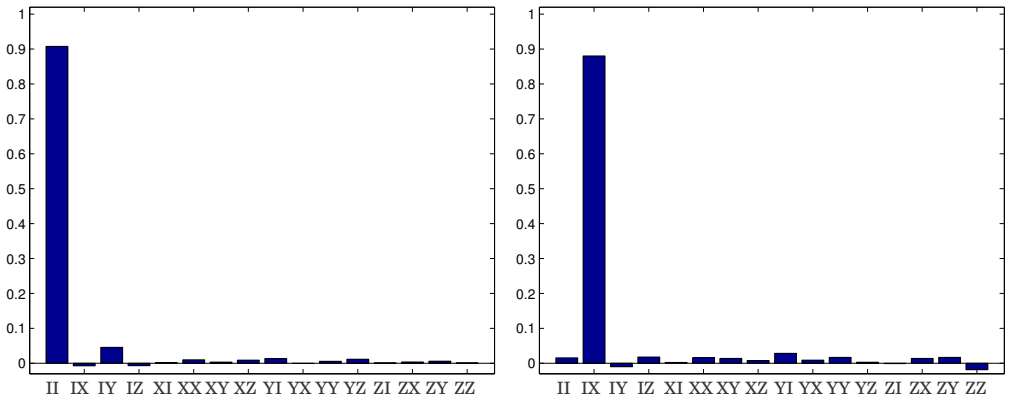

Figure 7.4: **Diagonal χ matrix elements for two processes.** On the left the process corresponding to the identity channel while on the right a process corresponding do an X gate on the polarization qubit. In both cases the fidelity of the process obtained is of about 90%.

7.2.2 Full Process Reconstruction

Four very different processes were fully reconstructed: the identity, a unitary gate on the polarization qubit, a controlled gate U_c and a noisy version of U_c. The identity and the unitary gate on the polarization qubit were done as in the case of diagonal element extraction: by placing nothing or a wave plate affecting equally both paths. In this case the unitary gate studied was a quarter wave plate at $0°$. The controlled gate was implemented with wave plates at different angles in each path. Specifically we used two half wave plates one at $0°$ and the other at $45°$. They act as a Z gate if the photon is in path $|0\rangle$ and an X gate if the photon is in path $|1\rangle$. This unitary gate can be written as $U_c = (I - Z) \otimes Z/2 + (I + Z) \otimes X/2$. the fourth channel studied was a noisy version of U_c. It was implemented by adding phase noise to the path qubit. This was done by sweeping the Mach-Zehnder's phase several times during the measurement integration time. The χ matrix expected for this last process will then be the same as the "clean" version of U_c but with the off diagonal terms, corresponding to the path qubit, missing.

Figure 7.5 shows the full reconstruction of the χ matrix for the identity, a QWP at $0°$, the controlled gate U_c, and the U_c with dephasing in the path qubit. In all

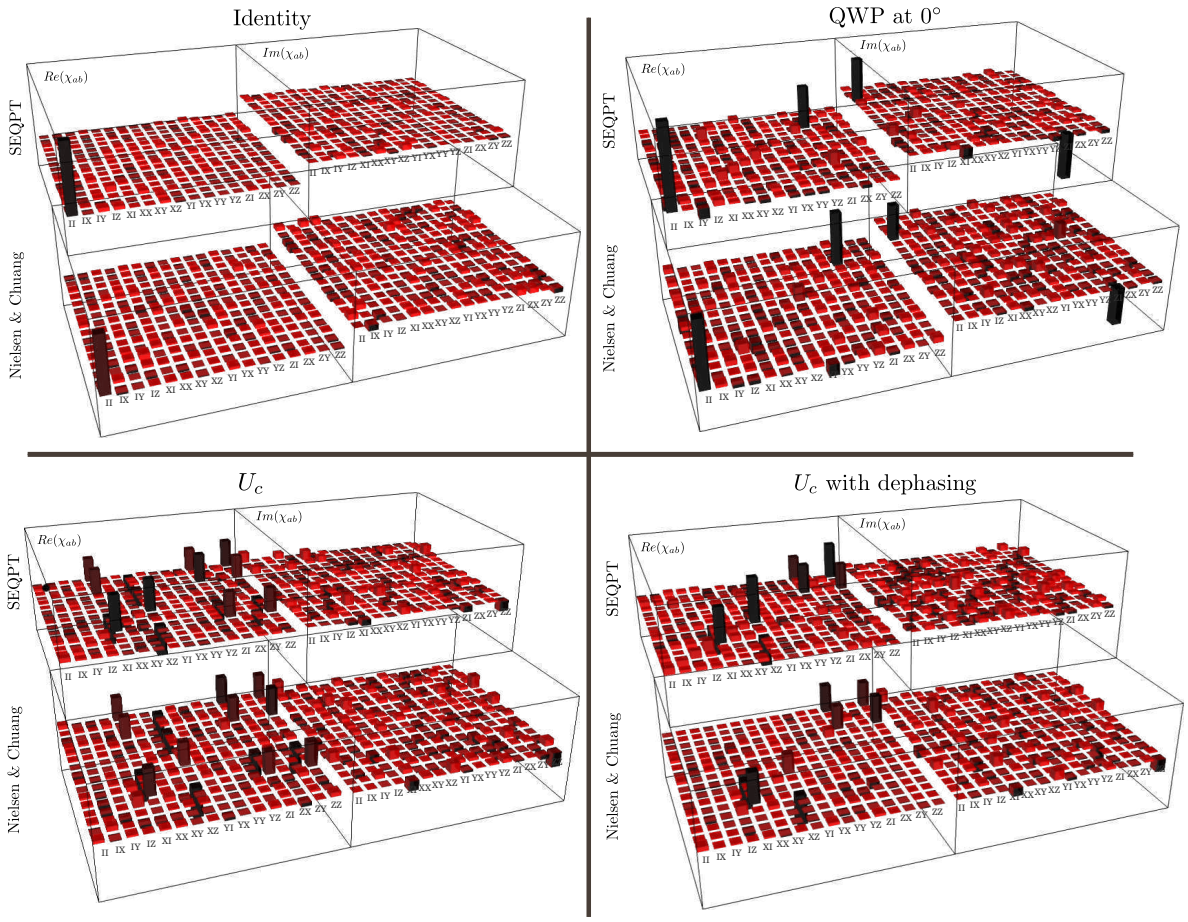

Figure 7.5: **Full reconstruction of two channels**. The χ matrices for a) the identity process and b) a controlled U_c process (see text). Shown are the real and imaginary parts of each one all in excellent agreement with the expected theoretical results. The fidelity between these reconstructed processes and the ones reconstructed by the standard inefficient Nielsen and Chuang method are for a) 91.8%, b) 90.1%, c) 93.1% and d) 94.0%.

measured processes we obtained excellent agreement with χ–matrix of the ideal process and with the one measured by the standard method [NC00]. We computed the fidelity between the χ matrix obtained with our method and the one measured using Nielsen and Chuang's method. As explained in Section 5.4.4, to obtain this fidelity one must renormalize the measured χ matrices so that they represent completely positive trace preserving channels. We obtained that for all the implemented channels such fidelity is above 90% (see Figure 7.5 for more details).

Even if the totality of measurements is not made, one can approximately reconstruct a full χ matrix. Figure 7.6 shows the full reconstruction of the χ matrices for the identity and the U_c gates done with partial information. As each element can be approximated, after M measurements with a precision scaling better than $1/\sqrt{M}$ so can the full chi matrix. On can see from the Figure that after 330 measurements the identity process can be clearly recognized. However for this same

amount of measurements the U_c gate is still not clearly recognizable from the statistical fluctuations. This is reasonable since the statistical fluctuations for 330 measurements should be of the order of 0.1 in each χ matrix element and the values of each non-null element of this process is 0.25 while in the identity the only non-null element has value 1. (Note the change in scale between the graphs of different processes.)

The previous analysis is qualitative but gives an idea of how channels can be estimated with a fixed amount of measurements which only sets the precision attained. If channels are sparser in the bases chosen then one will need more measurements to reach statistically significant values. However, the amount of measurements does not scale exponentially with the number of qubits but is only a function of the desired precision. In the next Section a new way of extracting information about channels in a quantitative way is introduced.

7.2.3 Quantum Process Identification

Full QPT does not take advantage of the most powerful aspect of this method: efficiency and selectivity. One can also perform efficient partial quantum process tomography measuring useful properties of the channel without fully determining the χ matrix. In doing so, the advantage of our new method over previous ones becomes very clear.

If one is interested in determining how close a given process is to a target process, the fidelity introduced in Section 5.4.5 is particularly useful. As detailed before, for the identity channel one needs to determine a single matrix element and for the U_c, only 16. In contrast to the total 256 elements this is already a substantial gain. Moreover, such coefficients can be estimated with increasing precision by increasing the size of the sample.

Figure 7.7 shows how these fidelities converge when the sample size is increased (curves correspond to different random choices for the order in which we sample over the 2–design). In all cases we see that it is possible to decide if the channel $\mathcal{E}$ is close enough to the target channel by making a number of measurements that is much smaller than the one required for full QPT. In such Figure we also show that the same method reveals the presence of noise in the controlled operation. With this method, exact answer to such questions can be given using fewer resources than before and good estimates can be given with a number of measurements that do not scale exponentially with the size of the system.

Many other estimators containing important information about channels can be extracted in this manner. For example, if one were designing error correction strategies it would be useful to know if a given type of noise is present or not, or whether it affects the qubits globally or individually. These kind of questions can be efficiently answered by choosing the appropriate χ matrix elements to sample.

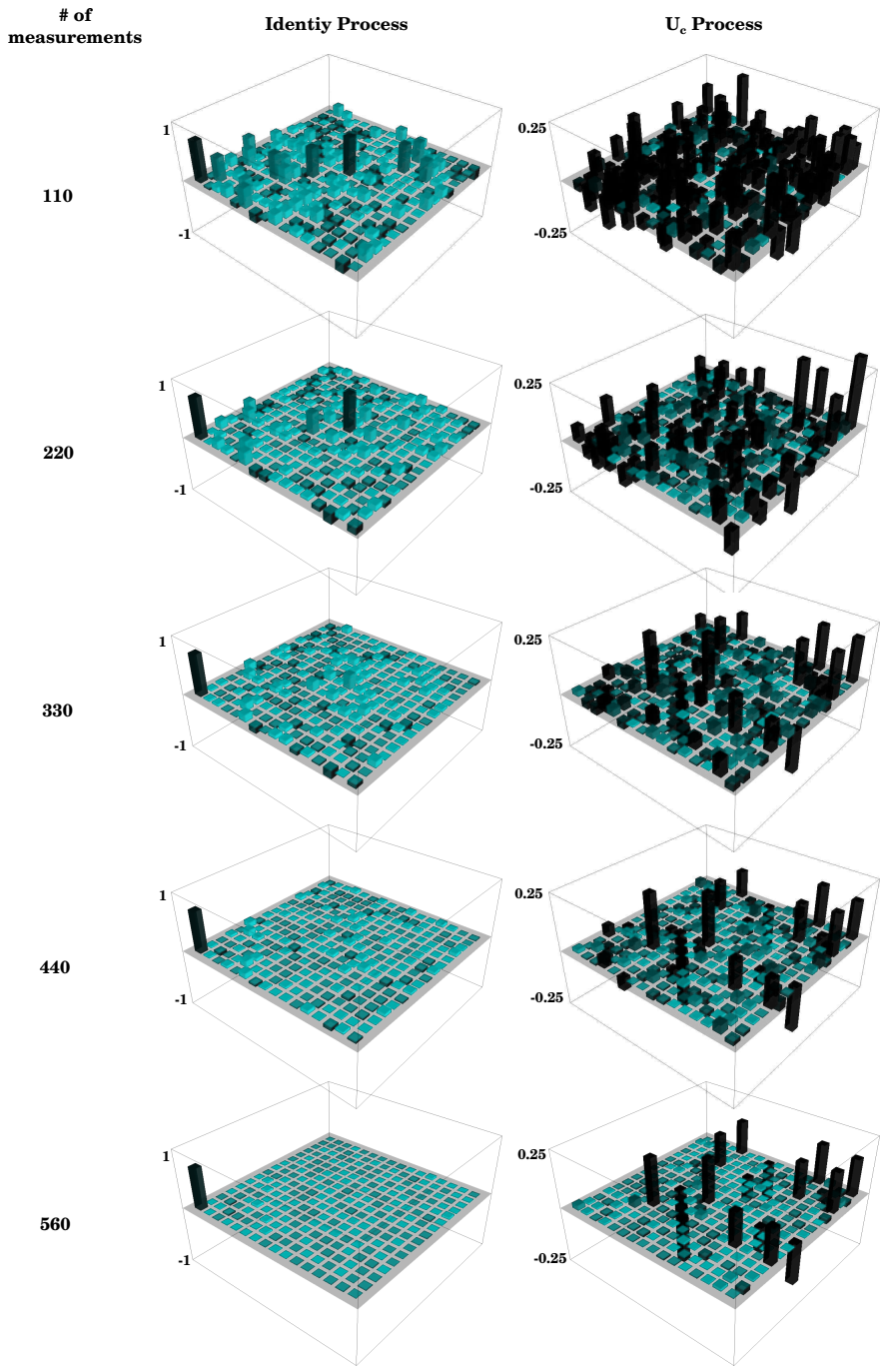

Figure 7.6: Determination of the full χ matrix after M measurements picked at random from the possible measurements on the 2-design for two of the studied processes. Even with an incomplete set of measurements the process can be distinguished with a precision that does not depend on the size of the Hilbert space. (Note the different in vertical axis scales.)

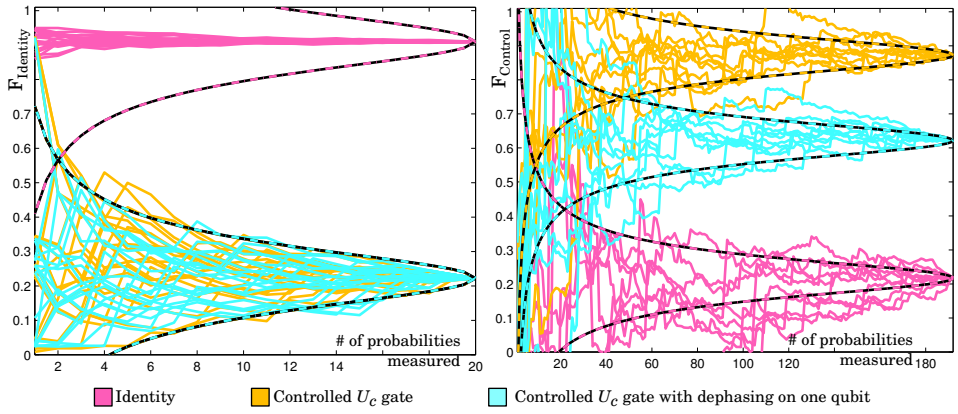

Figure 7.7: **Efficient parameter estimation.** By determining only some parameters characterizing a quantum channel different relevant questions can be answered. These parameters can be determined exactly or approximated by sampling over only some of the possible measurements needed to fully determine them. Depending on the complexity of the question more or less measurements are needed. In any case these values can be determined statistically with an error scaling with the amount of measurements better than $1/\sqrt{M}$, eliminating the need for exponential amount of measurements. Shown are the fidelities of the measured processes to two different target processes: the identity (left) and a controlled gate U_c (right) as a function of the amount of measurements done and for ten different choice of sampling order. Results for different channels show how quickly the estimation can differentiate between each one and converge to a value close to the exact one. Also shown in black and colored dashed curves is the statistical maximum deviation expected for each result.

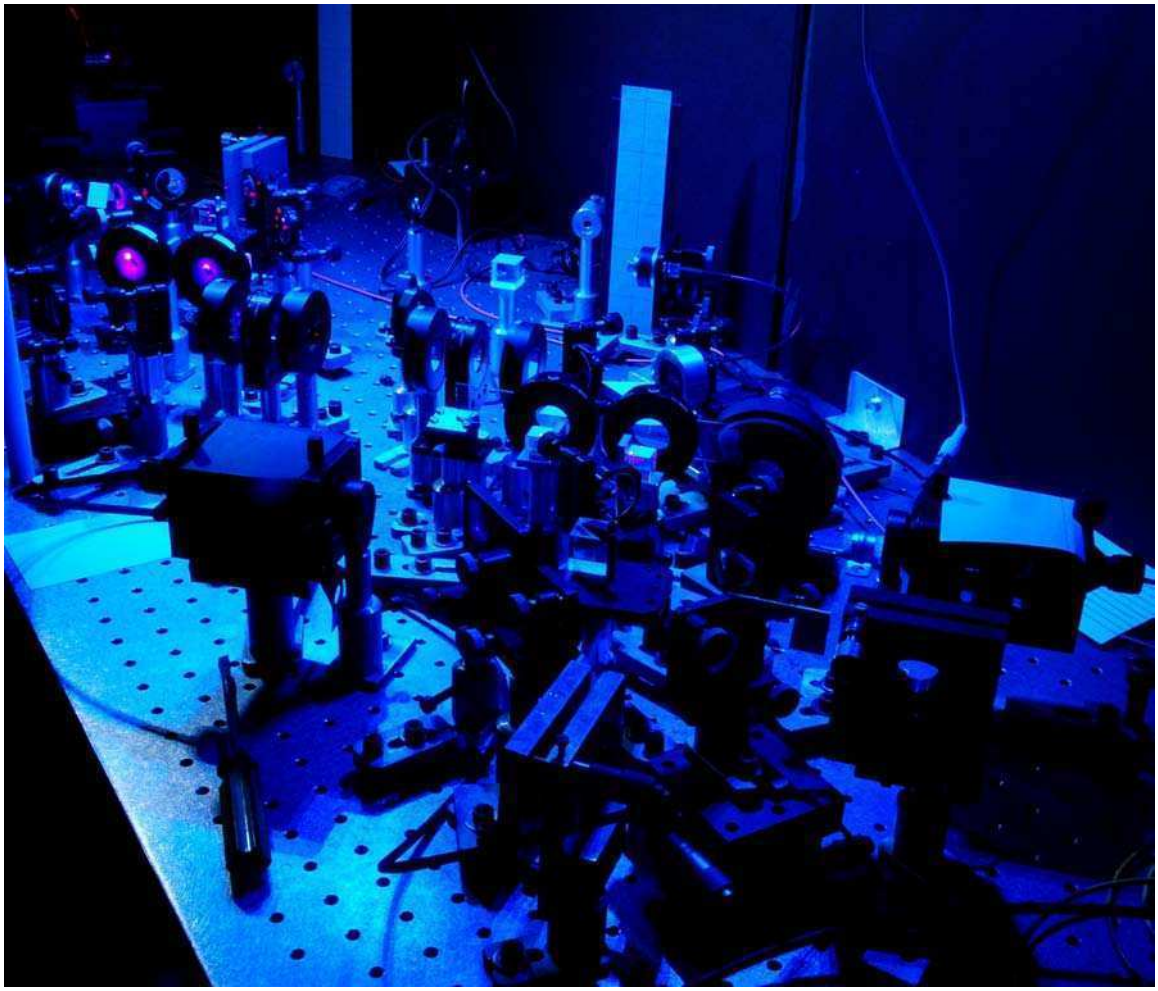

Figure 7.8: **Perspective view of the whole experiment.**

Chapter 8

Conclusion

The experiments presented in this thesis accomplish one of the fundamental tasks needed to build a general purpose quantum computer: it allows one to efficiently and selectively characterize any quantum process. The combined power of the 2-designs together with mutually unbiased bases allows an efficient and robust way of extracting selective information about quantum channels. Our photonic experiments confirm this by identifying crucial information determining the nature of different quantum processes in a selective manner. Different channels were discriminated from each other and specific properties characterizing a channel were extracted using less resources than needed for full standard quantum process tomography. Moreover, the experimental results confirm that with M measurements one can statistically find any of these values with errors scaling better than $1/\sqrt{M}$. These results hold even in an experimental setup where state preparation and projection is not perfect showing its robustness to these kind of errors.

The experimental results presented are the first experimental demonstration of the only known method capable to extract information about a channel in an efficient and selective manner regardless of the size of the system under study.

The quantum process tomography experiments presented in this thesis are the first original results produced in the Quantum Optics laboratory at CITEDEF. This laboratory was set up during the course of this thesis. Many techniques were developed and mastered. Generation of heralded single photons by parametric down conversion, single photon counting, active lock-in stabilization were central to the experiments on quantum process tomography. Also other techniques such as two photon interference and generation of entangled photons were investigated and will be central parts of future experiments that will be done in the laboratory. This next generation of experiments were planned during the course of the development of this thesis and are outlined in Appendix A.

Part III

Appendices

Appendix A

Other Proposed Experiments

Some other experiments with twin photons were designed and will be done in the near future. All of them encode qubits on the polarization and path of photons generated by spontaneous parametric down conversion (SPDC). In contrast to the experiments presented in this thesis, these future experiments use both photons generated by SPDC as carriers of quantum information.

The three proposals cover different areas of quantum information science, not only quantum process tomography. In the order presented, the first one is an extension of quantum process tomography to a system that allows more processes to be studied, the second one is a teleportation scheme where one can tune different noise mechanisms to study the effect of decoherence and imperfect state preparation on the optimal teleportation strategy, and the last one is a general two photon bi-qubit state tomographer which can also be used for quantum key distribution with tomographic security.

The teleportation experiment design was discussed and developed with Bruno Taketani from the UFRJ and will be set up in the laboratory at CITEDEF in 2012. The state tomographer / quantunm key distributor was developed with Ariel Bendersky and is now being setup in the laboratory at CITEDEF.

A.1 SEQPT on two polaization qubits

This is a proposal to perform quantum process tomography on two qubits using the polarization degrees of freedom (DOF) of two photons. Entangled photons are generated SPDC are used. In contrast with the experiments presented in the bulk of this thesis, in this case both photons are used to store and process quantum information. A priori, the main drawback of this approach is that the needed controlled operations between the two qubits coded in different photons can only be done probabilistically. On the good side, this approach frees the path DOFs so they can be used as extra qubits to study dynamics of controlled environments.

In principle, for two photon gates, gate probabilities can be achieved as close to unity as desired[KLM01], but this requires the use of an increasing amount of ancillary photons and complicated setups. This is not only complicated from an experimental perspective. It might also spoil the necessary assumption that the noise in the state preparation and measurement is much less than that we

want to measure in the channel $\mathcal{E}$. The probabilistic CPhase gate on polarization qubits proposed by Hofmann-Takeuchi [HT02] has many advantages: it requires no ancillas, it can be easily implemented [LWP+05, KSW+05, OHTS05], and it works as a CPhase on polarization qubits even when there is some information in the path degree of freedom of the photons (see Appendix B). As this gate relies on post-selection only it can only be used once for subsequent uses would spoil the error syndromes[HT02].

The experimental setup is shown in Figure A.1. State preparation is performed with half wave plates and polarizers on each photon. Preparing states in the XX, YY and ZZ bases is done through the solid paths while the states of the belle and beau bases are done through the dotted ones. The SPDC source must emit pairs of photons maximally entangled in polarization. Will suppose, for simplicity that it produces the state $(|HH\rangle + |VV\rangle)/\sqrt{2}$. To prepare the unentangled states of the XX, YY and ZZ bases the photons go through a horizontal polarizer letting only the state $|HH\rangle$ go through with probability $1/2$. (Alternatively this can be done by modifying the polarization of the pump beam and using always the same paths). To prepare the entangled states of the belle and beau bases the photons circumvent the polarizer and go directly to the first set of quarter-half-quarter (QHQ) wave plates. There, state preparation is finished with the by applying rotations on each photon to achieve the randomly selected input state and basis.

After the photons go through the channel state readout is done in a similar fashion. For measurement in the unentangled bases the photons are sent directly to the QHQ wave plates. For the entangled, belle and beau bases, a controlled operation between the qubits must be done (see table 7.1). To do so the Hofmann-Takeuchi CPhase gate, described in Section 3.2.2 is an optimal solution. By making the photons go through this gate and then the set of QHQ wave plates one can perform proyective measurements on these bases. Effective gate operation occurs with probability 1/9 and is confirmed by the detection of one photon in each output port.

Many operations can be done on this quantum channel. All unitary gates on single qubits are easily implemented. For example, a spin flips on any qubit is done by rotating the polarizations with a half wave plate at the desired path. Hadamards and phase flips, as well as any other type of two qubit gates unitary gates, can be done with the same QHQ wave plate combination. Moreover, as shown below, non

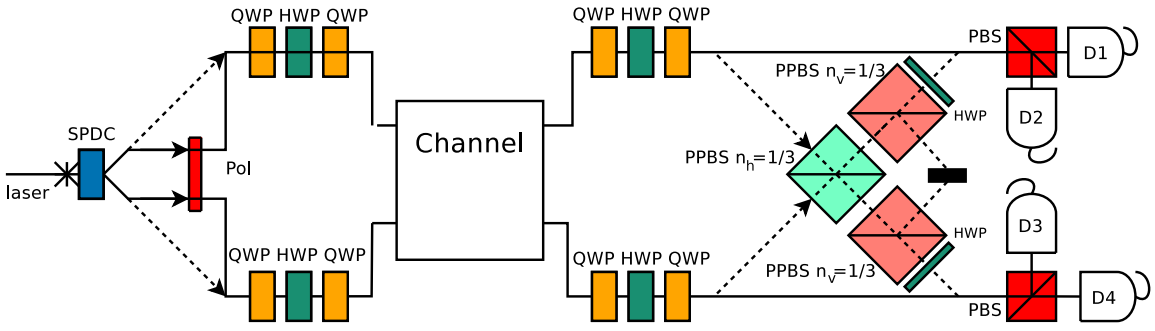

Figure A.1: Tomographer for two qubits encoded in the polarization of two photons.

unitary gates can be designed for this tomographer.

Besides the drawback of non deterministic operation, this tomographer has a huge advantage over the ones used in the core of this thesis: the path qubits of the photons can be used as and environment to simulate or model controlled non unitary processes on the polarization qubits. They can be used to engineer an environment. As discussed in Appendix B, one needs to ensure that the CPhase gate, used in the last step of our tomography scheme, keeps on working even when the photons carry information in their path degree of freedom (i.e.: when they are in superposition of two different paths). This will only happen if these qubits state is spanned in their symmetric subspace: the gate will work when the whole state of the two photons can be written as

$$|\psi_{sym}\rangle = |a_p\rangle \left|\psi_m^+\right\rangle + |b_p\rangle \left|\phi_m^+\right\rangle + |c_p\rangle \left|\phi_m^-\right\rangle \tag{A.1}$$

where the sub-indices m and p indicate the path (momentum) or polarization qubits respectively; ψ^+, ϕ^+, ϕ^- denote the symmetric bell states and a, b, c can be any state.

The underlining physical reason for this behavior is that the gate operation relies on Bosonic interference effects so if the pair path modes have weight in the antisymmetric subspace (the singlet state ψ^-) they do not interfere as bosons but, rather, as fermions and the gate does not work as intended. Only if the spatial part is symmetric photons will interfere as expected, effectively doing a CPhase gate on the polarization qubits leaving the path ones unaltered. This difference in interference behavior is actually the basic physical phenomena behind Hong-Ou-Mandel interferometry which is responsible for the operation of this gate. Here, however it poses a limitation on its extension.

Maintaining the path qubits in the symmetric subspace restricts very heavily the kind of operations that can be done on the whole set of qubits, the main drawback is that all controlled operations between the path and polarization qubits are not closed in this subspace. However as described in Appendix B some operations are allowed and they could be used to design controlled interactions between the system (polarization of both photons) and the environment (symmetric subspace of the path of both photons).

A.2 Noisy teleportation

Teleportation is an algorithm by which the state of a quantum system is transfered to another distant one using entanglement and classical communication as physical resources[NC00]. The first demonstration used two pairs of polarization entangled photons[BPM$^+$97], but the second one by the De Martini group[BBDM$^+$98] used just one pair of photons and stored an extra qubit in the path of of one of those photons. Their experiment used a complicated set of gates which can be strongly simplified. Moreover, the path qubit on the other photon can be used as an environment to study the effects of noise on the teleportation protocol used.

It turns out to be that several kinds of noise actually enhance teleportation fidelity [BmcHHH00]. In other cases, depending on the type of the noise present, different teleportation algorithms yield better or worse fidelities. All these cases

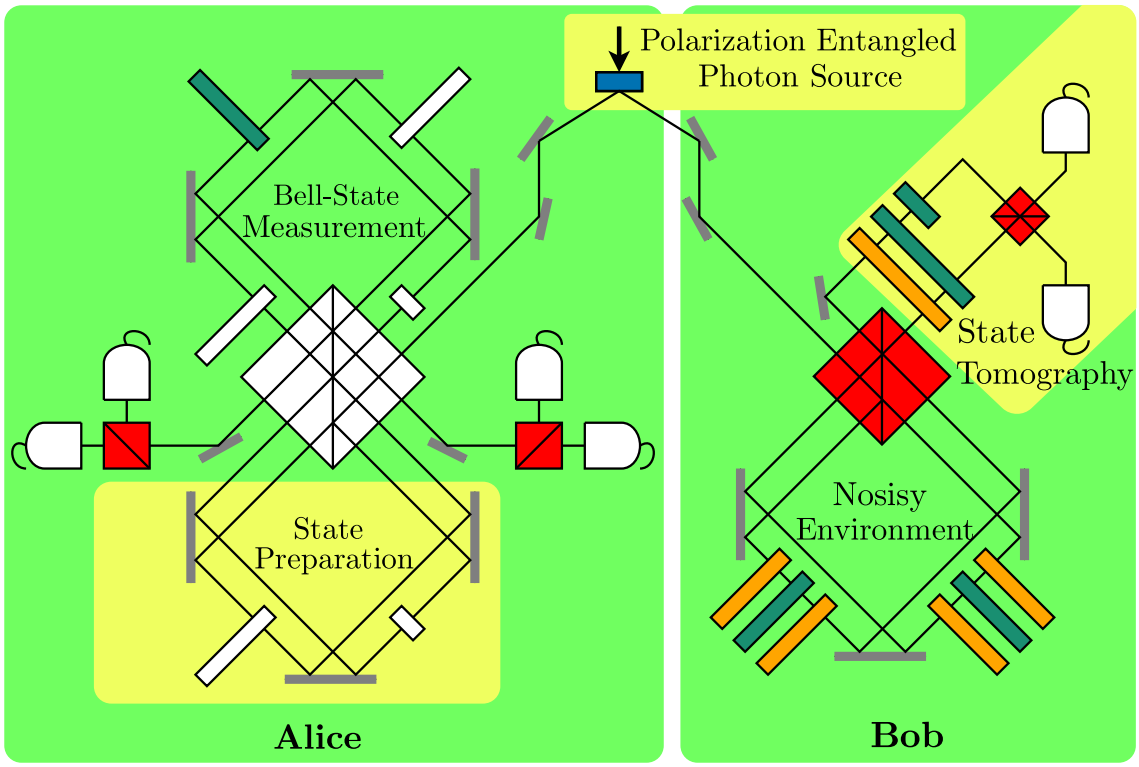

Figure A.2: Noisy teleportation experimental design. Blue: nonlinear crystal for spontaneous parametric down conversion. Red cubes: polarizing beam splitters. White cubes: non-polarizing beam splitters. Green/yellow plates: half/quarter wave plates. White plates: phase plates, Gray: mirrors.

were studied in Bruno Taketani's PhD thesis [Tak11] with whom the following experiment was discussed.

The basic idea is illustrated in Figure A.2. A polarization entangled photon source is used as the entanglement resource. Alice prepares the state she wants to teleport to Bob on the path qubit of the photon she gets. To do a projective measurement in the bell basis she then does deterministic controlled operation between the path and polarization of this photon. The information of her measurement is then sent to Bob who rotates the polarization of his photon accordingly to recover the state Alice had previously prepared. Additionally Bob's polarization photon may suffer from decoherence due to controlled interactions with its path qubit in an extension of the controlled environment designed and used by the Rio group in [ADMHM$^+$07].

The teleportation scheme, neglecting the noise part, is as follows. To describe the states the creation operator formalism is used (the daggers and the vacuum state are not written for clarity). The entangled photon source produces the state:

$$A_t B_t (a_H b_H + a_V b_V) \tag{A.2}$$

Capital letters indicate the path qubit, lowercase for polarization, (A, a) for Alice's photon and (B, b) for Bob's.
Then Alice, with an appropriate BS and phase shift plates, prepares the state she

wants to teleport.(we leave out B_t because it will never change during these first steps)

$$(\alpha A_t + \beta A_b)(a_H b_H + a_V b_V) \tag{A.3}$$

then, by placing a wave plate to rotate the polarization depending on the path, a CNOT on $a_{H,V}$ with $A_{t,b}$ as a control is implemented

$$\alpha A_t(a_H b_H + a_V b_V) + \beta A_b(a_V b_H + a_H b_V) \tag{A.4}$$

following Alice must do a Hadamard gate on the $A_{t,v}$ modes with a 50:50 BS at the exit of the interferometer. ($A_{t,v} \rightarrow A_t \pm A_v$) This results in the state.

$$\alpha(A_t + A_b)(a_H b_H + a_V b_V) + \beta(A_t - A_b)(a_V b_H + a_H b_V) \tag{A.5}$$

Regrouping terms one has:

$$A_t a_H(\alpha b_H + \beta b_V) + A_t a_V(\alpha b_V + \beta b_H) + A_b a_H(\alpha b_H - \beta b_V) + A_b a_V(\alpha b_V - \beta b_H) \tag{A.6}$$

At this point Alice measures and can discriminate position and polarization, the state collapses to the commuting observables $a_{H,V}$, $A_{t,b}$. Depending on Alice's measurement outcome Bob will then have his photon one of the following states

$$\begin{aligned} A_t a_H &\rightarrow \alpha b_H + \beta b_V \\ A_t a_V &\rightarrow \alpha b_V + \beta b_H \\ A_b a_H &\rightarrow \alpha b_H - \beta b_V \\ A_b a_V &\rightarrow \alpha b_V - \beta b_H \end{aligned} \tag{A.7}$$

So, if Alice tells Bob her measurement outcome, Bob will know which unitary operations to do on his state in order to obtain the state Alice wanted to teleport; that is: $\alpha b_H + \beta b_V$.

A.3 Bi-qubit two-photon QST and QKD

The experimental setup shown in Figure A.3 can be used for a couple of different experiments on Quantum State Tomography (QST) and Quantum Key Distribution (QKD). It consists of a Type-I down conversion source producing hyper-entangled photon pairs in their polarization and path degrees of freedom similar to that presented by at [BCMDM05]. The combination of subsequent interferometers and wave plates allows one to rotate and measure in any of the mutually unbiased bases associated with any pair of qubits.

For state tomography this is useful for such a 4 qubit state has never been properly tomographed. Several experiments have shown it is effectively a hyper-entangled state, but none have done its full state tomography[RT90, BCMDM05]. Moreover this two-photon bi-qubit system can be used to test general aspects of the theory of quantum measurement with copies developed by Bendersky et. al.[BPC09].

As a quantum key distributor this proposal, schematically shown in Figure A.3, can work in two ways. With a protocol in which both parties choose a base out of the 5 mutually unbiased bases and use the coinciding measurements to extract a key.

The non coinciding measurements are used to do state tomography. This renders the protocol with tomographic security. As an alternative this this same setup a protocol in which the two parties use both their qubits as quadbits (4-dimensional states) can be done. In this case they would measure in only two bases making the key extraction rate higher.

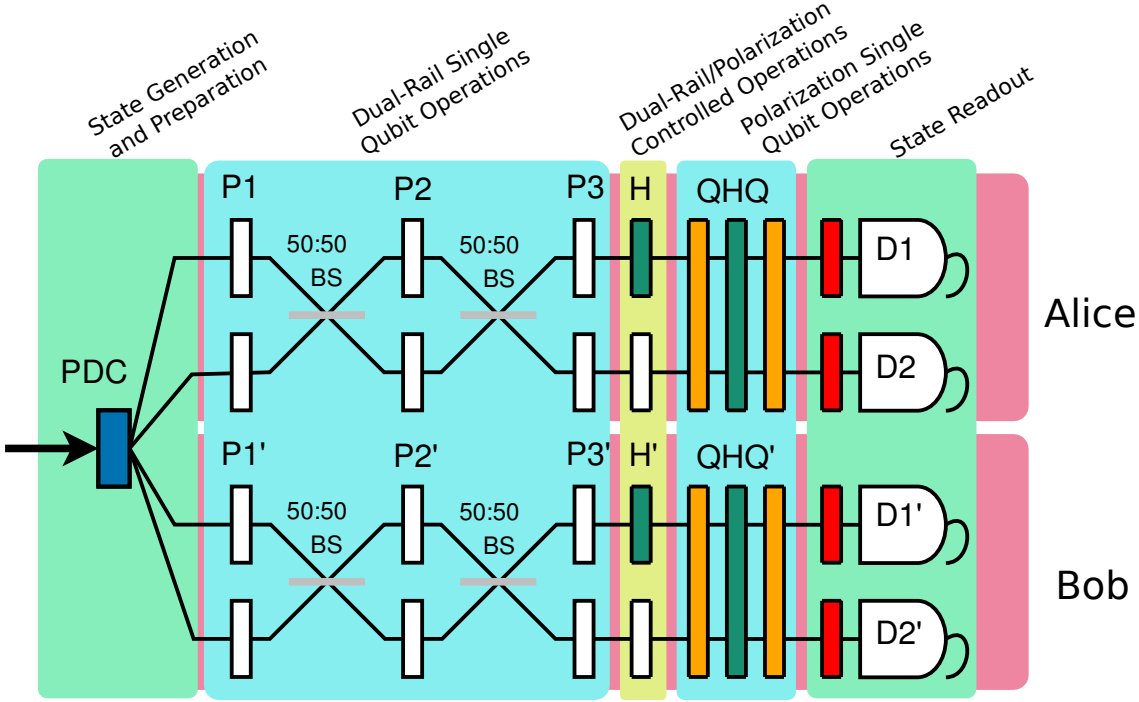

Figure A.3: Bi-qubit state tomographer / quantum cryptographer. Blue: nonlinear crystal for the generation of hyper-entangled states by spontaneous parametric down conversion. Red plates: polarizers. White cubes: non-polarizing beam splitters. Green/yellow plates: half/quarter wave plates. White plates: phase plates, Gray: mirrors.

Appendix B

Gates for Photons with Momentum and Polarization Qubits.

We have found that it is possible to make a controlled gate between the polarization qubits of two photons while leaving the momentum ones unchanged. The only gates where this works on are the ones that don't use ancillas [HT02, SKK01]. Figuratively one can understand this the following way. In the gates using ancillas there is always some probability that photons at the output ports of the gate are not be the same ones that went in, they could have originally been an ancilla. In such a case the information on the momentum modes is lost[1]. Conversely in the two proposals that do not use ancillas this information is not lost. These gates need not to be modified in any sense, their behavior just has to be reanalyzed for in this more complex situation.

The gate proposed and realized by Sanaka et. al.[SKK01] works with a Franson-type layout, it is a CNOT on the polarization qubits and when photons and it behavior does not change when photons have have extra information in their momentum DOF, i.e. when they are in a superposition of two paths. This layout has a huge experimental disadvantage: Franson-type interference is based on photon superposition of two paths paths which differ by an amount of time a detector can resolve, to current standards this is a path difference o about a meter. Even worst, if two gates want to be implemented in sequence, the second one has to have the double path difference than the first one in order to perform effective post-selection, i.e. correct coincidence counting.

The rest of this Section will focus on the controlled gate proposed by Hofmann and Takeuchi [HT02] which was later simplified and realized experimentally by three different groups at the same time [LWP$^+$05, KSW$^+$05, OHTS05]. Is is a CPhase gate on polarization qubits which works well and leaves the momentum ones unchanged as long as they are in a symmetric state. This means the state of the system must be such that it can be written as

$$|\psi_{sym}\rangle = |a_p\rangle \left|\psi_m^+\right\rangle + |b_p\rangle \left|\phi_m^+\right\rangle + |c_p\rangle \left|\phi_m^-\right\rangle \tag{B.1}$$

where $|a_p\rangle$, $|b_p\rangle$, $|c_p\rangle$ can be any unnormalized state of the polarization qubits and

[1]It really is not correct to think of photons as distinguishable in experiments that rely on two photon interference. However in this case it helps understand why gates that use ancillas will never work with information stored in other degrees of freedom.

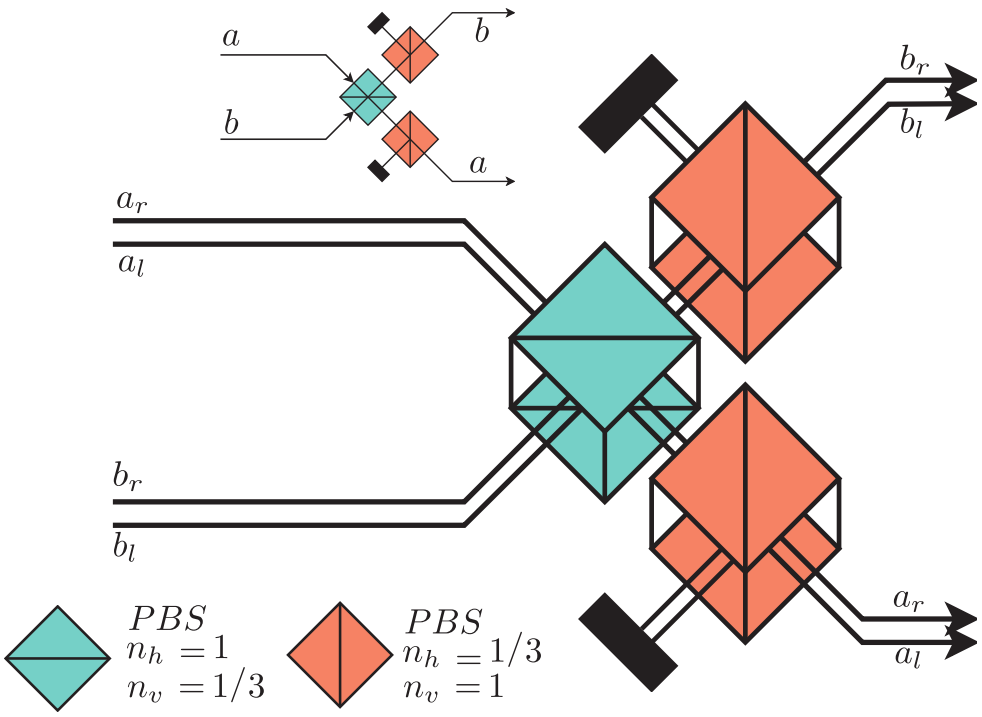

Figure B.1: **The extended CPhase gate**. Also shown is the corresponding labelling of modes. (Inset shows the original CPhase gate.)

$|\phi_m^+\rangle$, $|\phi_m^-\rangle$, $|\psi_m^+\rangle$ are the symmetric Bell states in the momentum qubits. As shown below, this poses only some restrictions on the kind of things that can be done. This gate's post-selection rules, however, also impede cascading them.

An extension to the Hofmann and Takeuchi Gate

Following the idea of the Hofmann Takeuchi gate given in Section 3.2.2 we now extend the analysis to include photons that have a momentum qubit too. Each photon will now have two qubits; one in its polarization degree of freedom (DOF) and the other in its momentum DOF. The representation of the states, in terms of Fock operators, now has one more index (r, l) indicating its momentum DOF. For example, for the photon in mode a, one has $a_{hr}, a_{hl}, a_{vr}, a_{vl}$. This is schematically shown in Figure B.1. When these photons are sent through the CPhase gate all the possible modes transform as

$$\begin{aligned} a_{hi}b_{hj} &\rightarrow \frac{1}{3}a_{hi}b_{hj} + \psi_q \\ a_{hi}b_{vj} &\rightarrow \frac{1}{3}a_{hi}b_{vj} + \psi_q \\ a_{vi}b_{hj} &\rightarrow \frac{1}{3}a_{vi}b_{hj} + \psi_q \\ a_{vi}b_{vj} &\rightarrow -\frac{1}{3}(2a_{vj}b_{vi} - a_{vi}b_{vj}) + \psi_q \end{aligned} \tag{B.2}$$

where i, j can be either r or l.
At first sight, because of the last line, it might seem that the gate will only work of the momentum DOF is in a superposition of $i, j = r$ and $i, j = l$ but closer inspection shows that it also works for the superposition

$$a_{vr}b_{vl} + a_{vl}b_{vr} \rightarrow -\frac{1}{3}(a_{vr}b_{vl} + a_{vl}b_{vr}) + \psi_q \tag{B.3}$$

it works too. In ket notation this state is $a_{vr}b_{vl} + a_{vl}b_{vr} \rightarrow |VV\rangle\,|\psi_m^+\rangle$. We therefore conclude that this gate will performs a CPhase on the polarization DOF qubits leaving momentum DOF qubits unchanged when the momentum qubits are in the subspace spanned by $|\phi_m^+\rangle$, $|\phi_m^-\rangle$, $|\psi_m^+\rangle$ (or equivalently $|00\rangle$, $|11\rangle$, $|\psi_m^+\rangle$).

The physical principle behind this behavior is simple. The gate relies on Bosonic interference to work correctly. The state of any two pair of photons has 3 relevant properties: polarization (H,V), momentum (r,l) and which path the photon is on (a,b). A they are bosons, the ket representing the state of both must allways be symmetric upon a permutation of the photons. Interference only takes place in the first PBS and when both have vertical polarization (see equation 3.25, horizontal polarization is just transmitted while different polarizations never interfere). The polarization part $|VV\rangle$ of the state is symmetric and can be factorized out. The two remaining parts must be on a whole symmetric. If the momentum part is symmetric then the which path part will also be, so will interfere at the PBS in the same way as before, i.e. as bosons. Instead, if the momentum part is antisymmetric then so is the 'which path' part, and photons will interfere in a different way at the PBS, i.e. as fermions, and the gate wont work. This difference in interference, which is the basis of Hong-Ou-Mandel (HOM) interferometry, here poses a limit to the type of states on which this CPhase will work. Actually, this interferometer can be seen as a mixture between the dual-rail HOM bell state analyzer of [MMWZ96] and the polarization HOM bell state analyzer of [MWKZ96].

Possible Logic Gates with the extended Hofmann and Takeuchi Gate

One might wonder what kind of logic operation one can do with this CPhase. Our aim is to get as close as we can to universal 4 qubit logic. The main building blocks that will be used are the CPhase described above and the fact that any gate two qubit can be performed deterministically between the polarization and momentum qubit of the same photon. The main restriction is that momentum qubits have to be in the subspace spanned only by $|\phi^+\rangle$, $|\phi^-\rangle$, $|\psi^+\rangle$ in order to make a CPhase between the polarization qubits. Such a state is of the kind of equation B.1. It is interesting to see which operations one can do on these states that will not take them out of this subspace (i.e. under which operations the subspace is closed). The main interest in finding these operations is that as long as one stays in this subspace the polarization CPhase described above can be done. The following operations fulfill the required restriction. Each can be applied as many times as desired and in any order.

a Any single qubit operations on any the polarization qubits

b Any single qubit operations on both the momentum qubits (the same one on both at the same time).

c The CPhase on the polarization qubits itself.

d Any controlled operation between the qubits of the same photon as long as the control is always the momentum.

Note that **a** and **c** are sufficient to do any unitary operation on the polarization qubits [NC00].

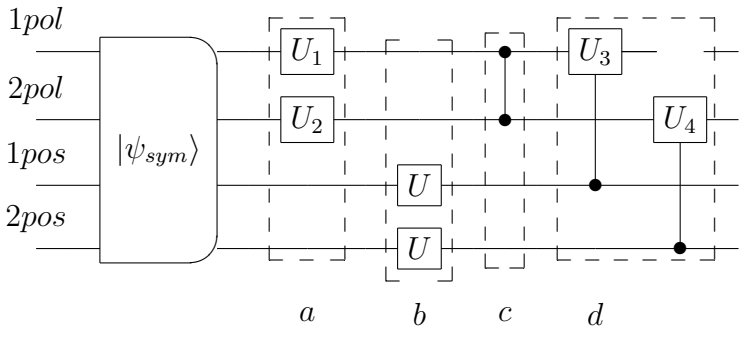

It is straight forward to realize that the triplet subspace is closed under operations **a**, **c** and **d**. That it is closed under the **b** set of operations can be seen by showing that it is invariant under the Hadamard and $\pi/8$ gates[2] (on both momentum qubits at the same time), for any single qubit gate can be approximated by combinations of these; alternatively this can also be proved directly by checking how the state changes under an arbitrary single qubit operations which is the same on both momentum qubits [NC00].

If more restrictions are set on the input state, i.e. on the subspace in which the polarization qubits are, some more operations can be done. For example:

- *The polarization qubits are on the triplet subspace.* If this is the case one can also do the CPhase on the momentum qubits as long as one hasn't done operations of type **a**, **b** and **d** yet. To do so one must swap the momentum and polarization qubits, which can be done deterministically [Fiorentino Wong SWAP], then perform the CPhase and finally swap back.

- *The polarization qubits are on the subspace spanned by ϕ^+, ϕ^-.* On can make any controlled operation between the qubits of the same photon with polarization as the control (in **d** the controls were the momentum qubits.)

An alternative interpretation is possible. One could consider, instead of 4 qubits with restricted operations, two qubits and one qutrit. The qubits will be on the polarization DOF, while the qutrit would be shared by the momentum DOF of both photons. The mapping of logical and physical sates could be, for example $|\phi_m^+\rangle \equiv |0\rangle$, $|\phi_m^-\rangle \equiv |1\rangle$, $|\psi_m^+\rangle \equiv |2\rangle$.

[2] The Hadamard gate is $H = (X + Z)/\sqrt{2}$ and $\pi/8$ gate is $T = e^{i\pi/8}[e^{-i\pi/8}\ 0;\ 0\ e^{i\pi/8}]$.

Appendix C

Ghost Imaging

Ghost imaging is a technique that allows reconstructing an image by correlation measurements. By measuring correlations between fluctuations in the field in two spatially separated, but correlated, pseudo-thermal beams an image can be obtained. Even if none of them contains intensity (or phase) information to reconstruct the image it can be recovered for the correlations between both. During the first months of setting up the laboratory at CITEDEF some experiments exploring this technique, as well as basic properties of pseudo-thermal beams, were studied.

This Section presents the results obtained. Some of the basic results measured are described in books such as Loudon's "The quantum theory of light" [Lou00]. The technique of ghost imaging, however is more recent. The seminal article by Bennink et. al. [BBB02] let to much research in the area. In a collaboration with the LPI laboratory at UBA a proceeding was published regarding this technique[CDS$^+$11].

This Section has no proper text apart from this introduction. All experiments are explained step by step in the caption of the images.

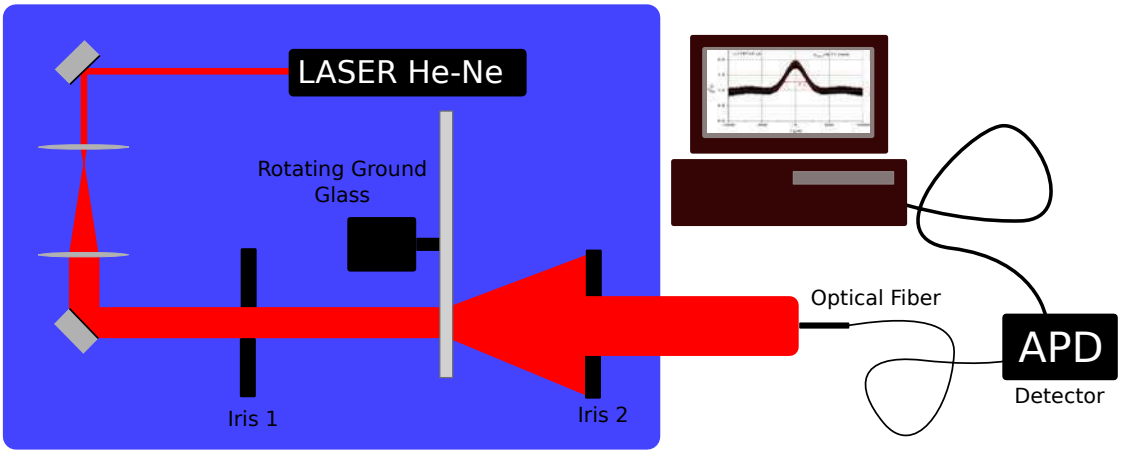

Figure C.1: **Experimental setup for pseudo-thermal light generation**. A Helium-Neon laser is expanded and sent through a rotating ground glass. This generates a moving speckle pattern. Measurements are made by collecting photons on a bare multi mode optical fiber which acts as a point detector and measuring with an avalanche photon counting diode. Data processing was done either by downloading time series from a digital oscilloscope and analyzing them on Matlab or via Labview on NI6602 counting card.

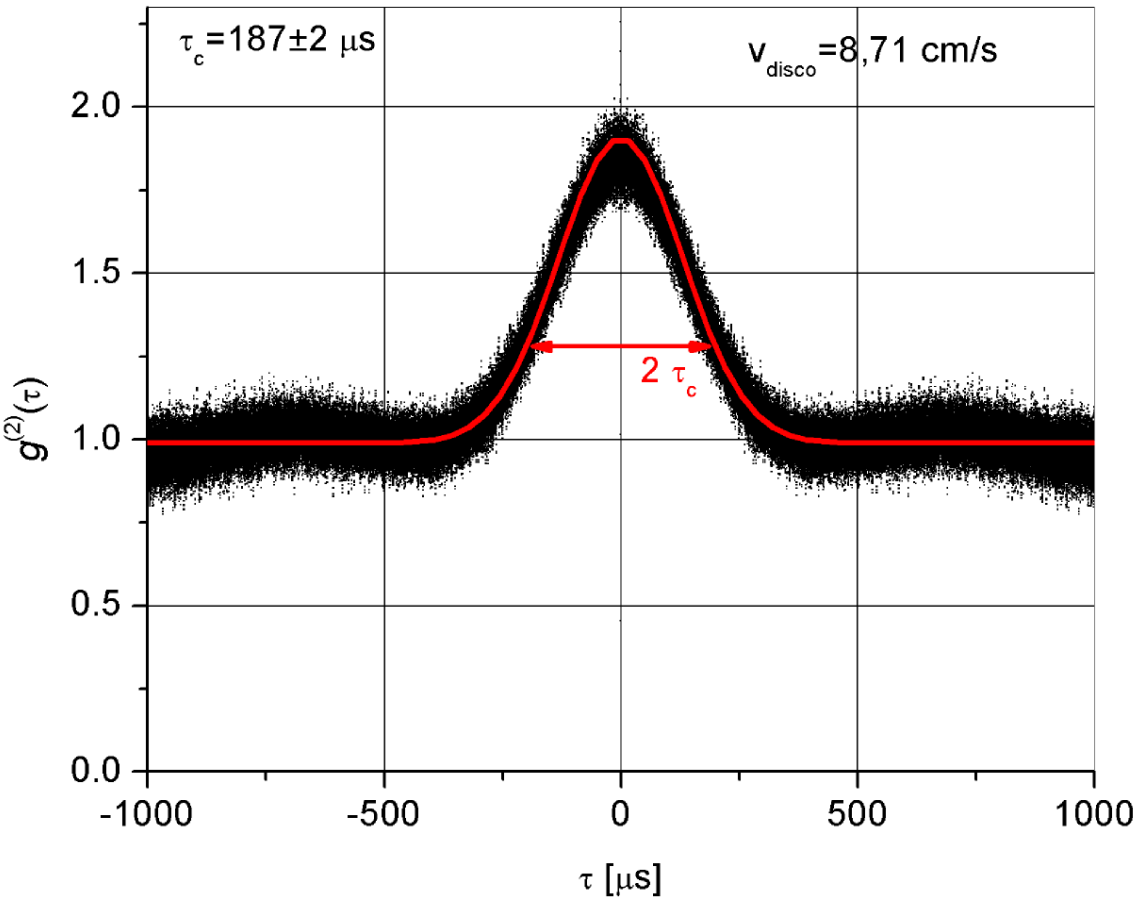

Figure C.2: **Second order correlation function.** The image shows the probability two photons appear separated by a time τ. For thermal or pseudo-thermal light the probability of finding two photons together is twice the probability of finding them separated by long times. Long and short times are scales set by the correlation time. For this case in which pseudo-thermal light is used the time obtained is $187 \pm 2\mu s$. This time depends on the disk angular speed, how fine or thick it is ground and on the size of the beam over the glass[MW95]. Correlation times for thermal sources are normally in the order of the picosecond so they are very difficult to measure whit current electronics. This is the main reason for using pseudo thermal light sources to study statistical properties of light. These measurements were taken by downloading the photon counters output signal from a digital oscilloscope. Many time series were recorded and the correlation function of each signal was calculated and averaged over all the measurements.

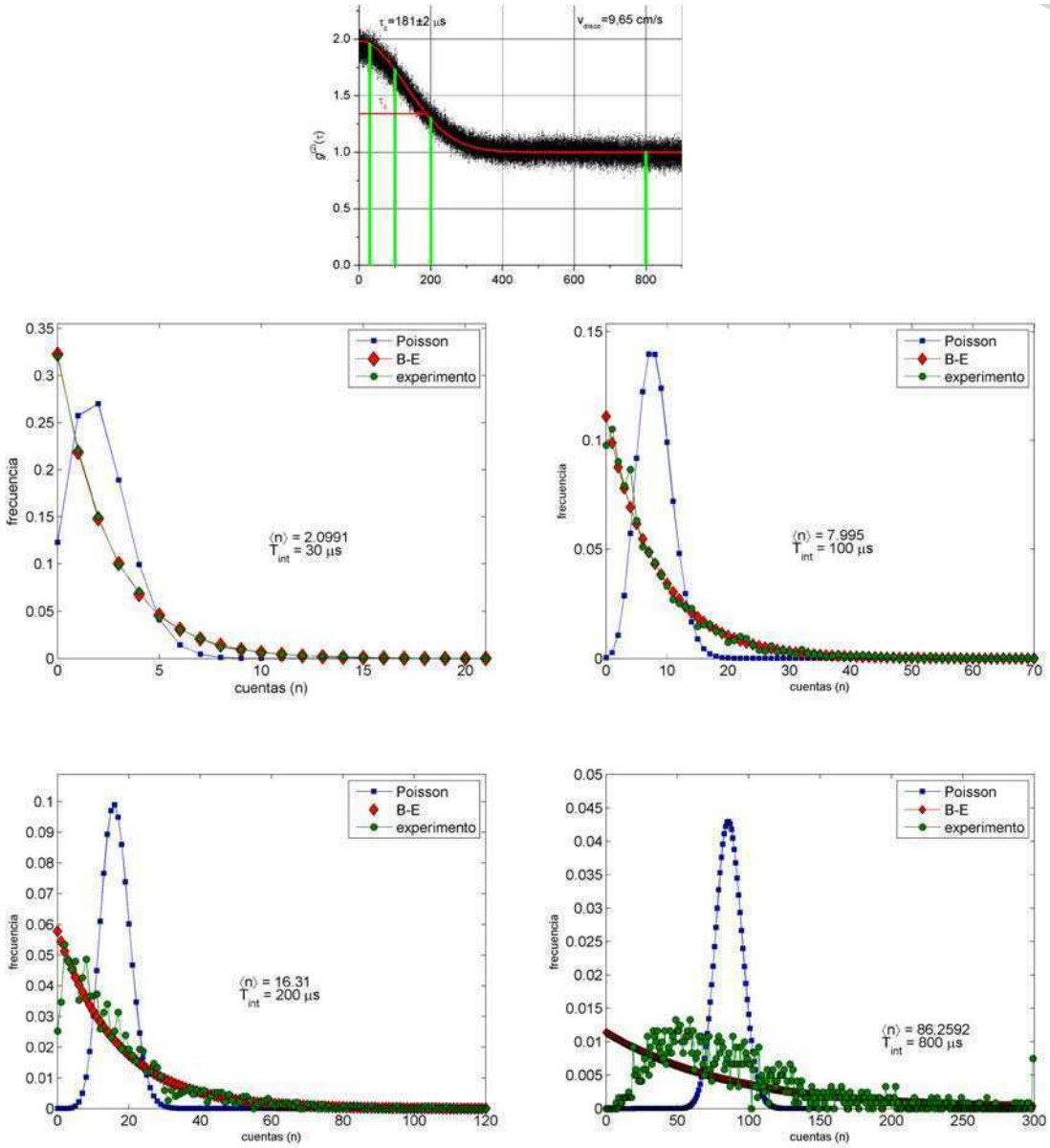

Figure C.3: **Statistical analysis.** Depending on the nature of the photon source and on the capability to detect or not well enough to resolve its characteristics one will see different statistical behaviour of the measured data. The four lower plots show the probability of detecting n photons in a varying time window. The times selected for each plot are indicated in the second order correlation function plot at the top. The measured data is plotted in green. The theoretical predictions for different distributions and same mean value as the measured one are plotted in red (for Bose-Einstein statistics) and in blue (for Poissonian statistics). It is clearly seen that when the measurement time is within the correlation time the observed statistics is mainly that of Bose-Einstein which corresponds to thermal light. However if the measurement time is a few times larger than the correlation time the measured statistics departs strongly form the Bose-Einstein type and starts approaching the Poissonian distribution which corresponds to randomly unconnected events.

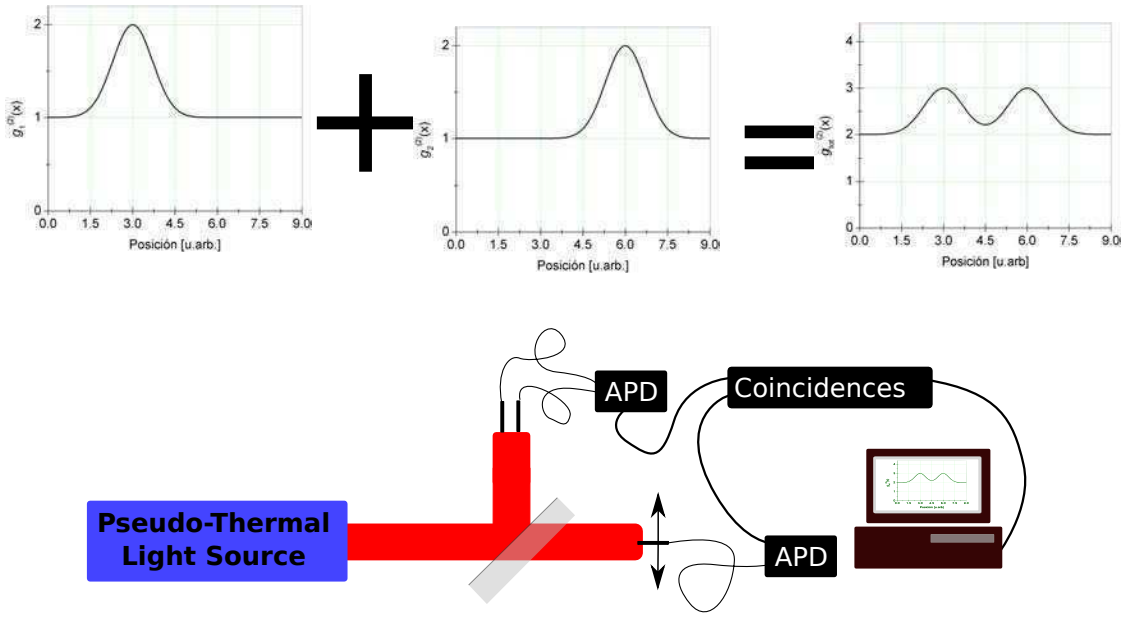

Figure C.4: **Basics of Ghost Imaging.** The idea behind ghost imaging is exemplified in the picture. The beam is split in two in a 50:50 beam splitter. On the top side the one has two fibers which collect light from two different places and are sent to the same detector. The top branch has no information on where the fibers are placed. The bottom branch has only one fiber connected to a different detector. The position of the bottom fiber can be scanned in the transverse plane. Coincidence counts are detected for zero delay between measurements in each branch. If only one fiber were present in the top branch one would see the second order correlation function, but in this case as a function of the position. If puts both fibers one would be able to resolve the position of each one. The information on the position of the top fibers is not present either on the top or bottom detector but in the correlation of the two. When adding an extra fiber there is also a decrease in visibility. This is because each fiber will also be sending extra uncorrelated light into the top detector. If more fibers were added to the top branch then the signal to noise ratio would decrease as the inverse of the amount of fibers.

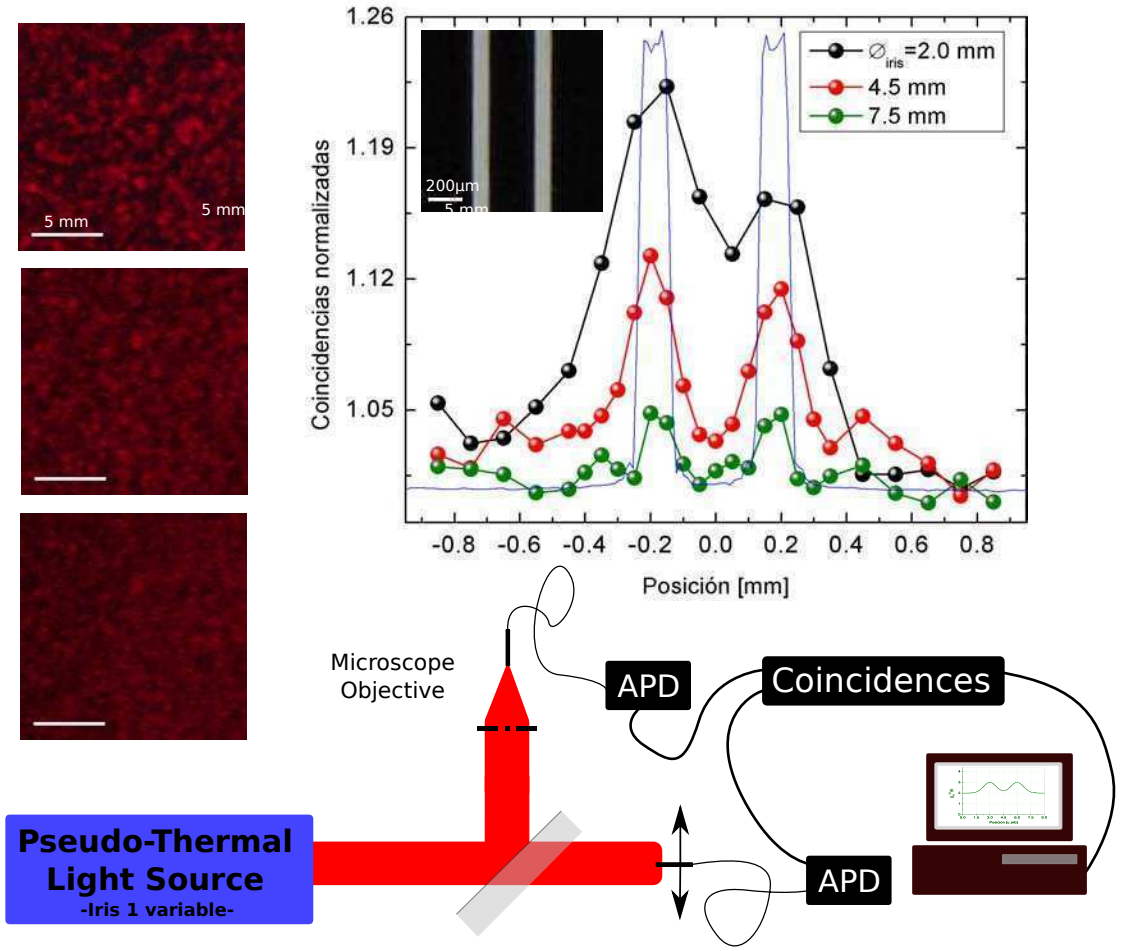

Figure C.5: **Visibility in ghost imaging.** A simple ghost imaging experiment in which two slits are imaged by placing them in front of the top detector and collecting all the light that goes through it with a microscope objective lens and an optical fiber. The transverse correlation size is changed by modifying the focusing of the He-Ne beam on the ground glass. It is seen, as expected, that for larger grain sizes (larger correlation length) the visibility is better but the resolution is worse. This can be understood as follows: if the grain is of the order of the size of the slit then they act as point receivers (as in the the Figure before); instead if the grain size is much smaller then each slit is a collection of receivers which will reduce the signal to noise ratio by the relative areas of the grain and the total hollow area illuminated.

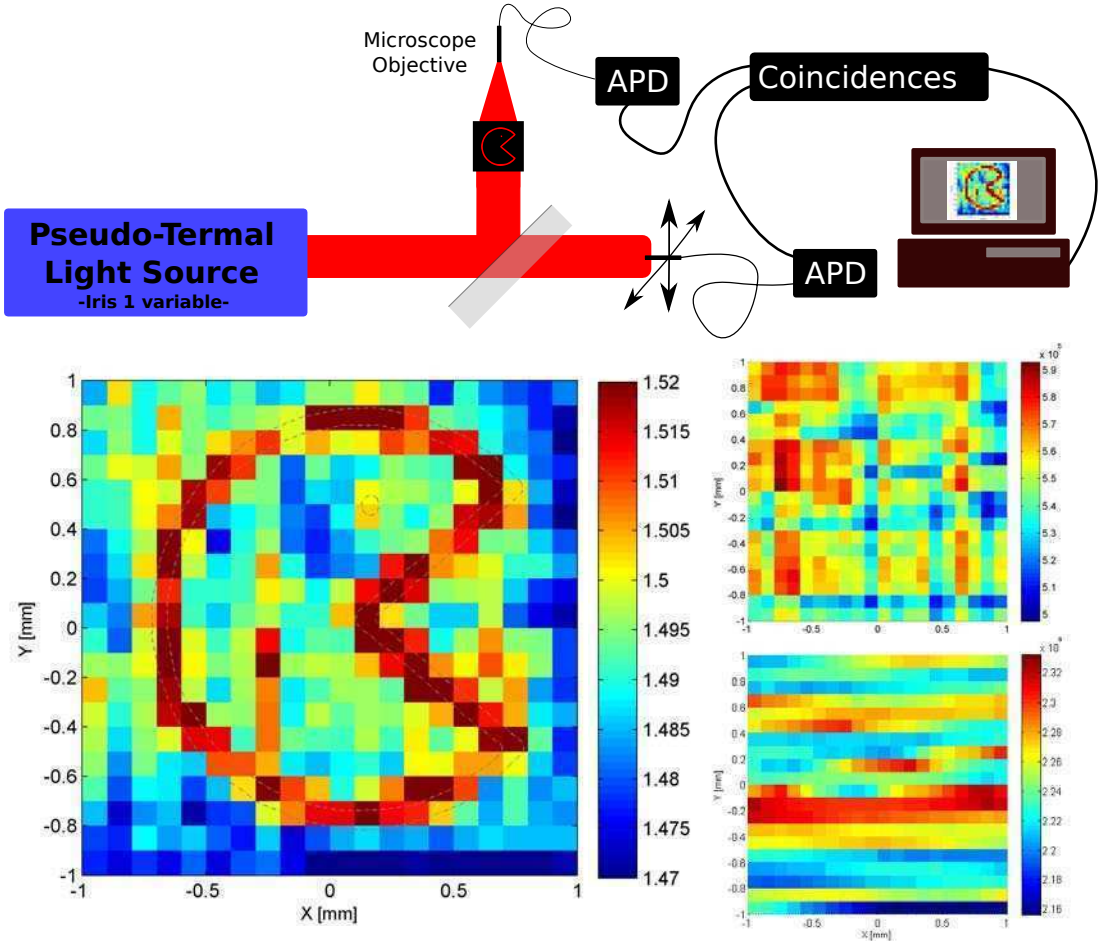

Figure C.6: **Ghost Imaging.** A full ghost imaging experiment where a 2 dimensional image is recovered form the correlations of the measurements in both measurement sides. The main panel shows the reconstructed image while the side panels show the photon counts on each detector which have no correlation with the measured image. The top side panel shows the counts registered in the detector behind the image while the bottom one shows the total counts at the scanning detector on the lower branch.

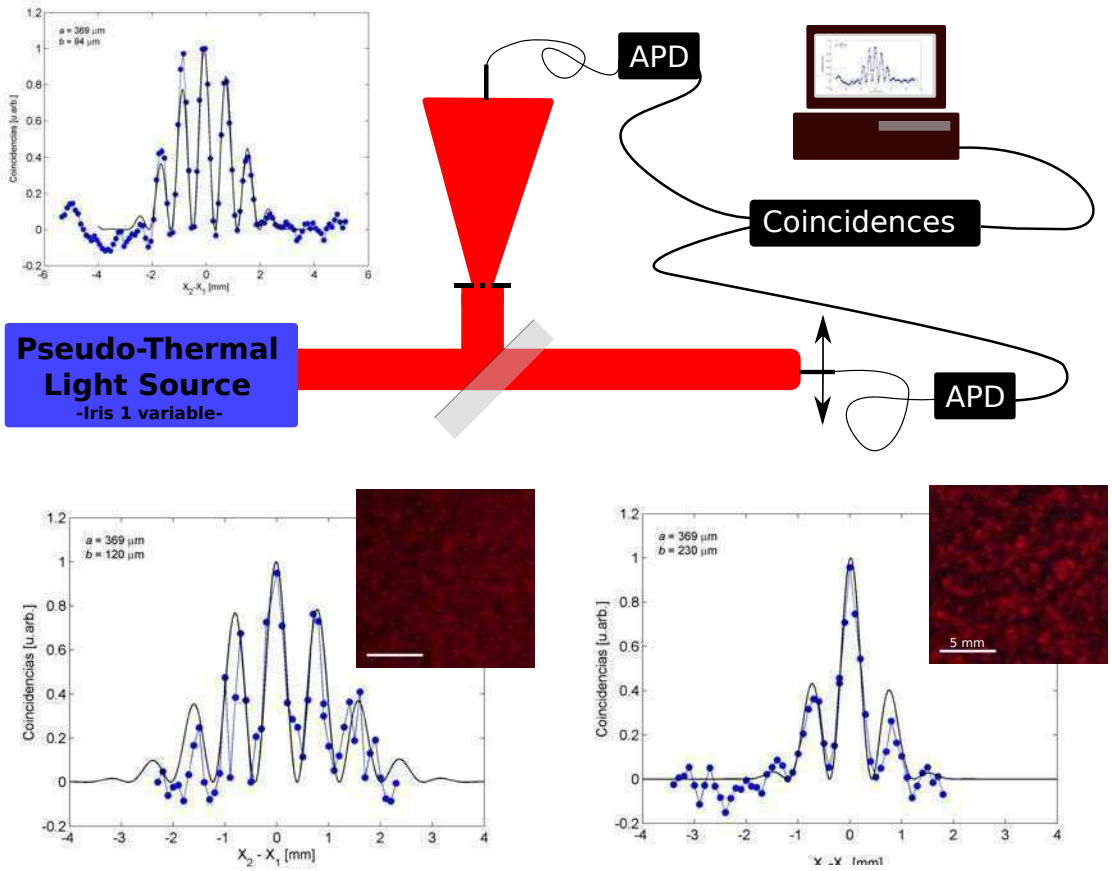

Figure C.7: **Ghost Diffraction.** As well as images, diffraction patters can be recovered form the correlation information in the two detections. In this case, however the detector behind the slits mus be a point detector placed in the far field of the slits. Here, also, a change in grain size changes fringe visibility.

Appendix D

Interferometer Active Stabilization

Two methods were used to actively stabilize the arms of Mach-Zehnder interferometers. Both methods utilize as a reference the interference signal form an extra beam propagating inside the interferometer close to the signal beam. This reference beam is then monitored in a photo-diode where an error signal is reconstructed. The reconstruction of this error signal is the main difference between both methods. In the final step the error signal is sent to a proportional-integral (PI) circuit which controls the position of a piezoelectric disc on which one of the mirrors of the interferometer is mounted.

D.1 Sider-fringe Stabilization

The simplest stabilization method used generates an error signal by comparing the reading from the photo-diode to a reference voltage. By changing the voltage on the piezoelectric disk one changes the relative path length of the interferometer producing a sinusoidal output at the photo-diode corresponding to the interference fringes. If one sets the reference voltage to some place between the minimum and maximum of the interference fringe then the error signal will grow if one goes over and decrease if one goes under the set value. This signal then goes to the PI circuit which controls the position of the movable mirror. More details on the circuit are seen in Figure D.1. The basic idea of this method was taken from [MSW92] where it was used to stabilize the frequency of an external cavity laser diode to a reference gas cell.

The main problem associated with this method is that it is amplitude dependent so it cannot lock well near the maximum or minimum of signals. If the overall signal varies so does the locking position. To solve this problem we introduced a lock-in stabilization method.

D.2 Lock-in Stabilization

The aim of this method is to be able to stabilize to the maximum (or minimum) of a reference signal irrespective of its amplitude. The idea behind the lock-in

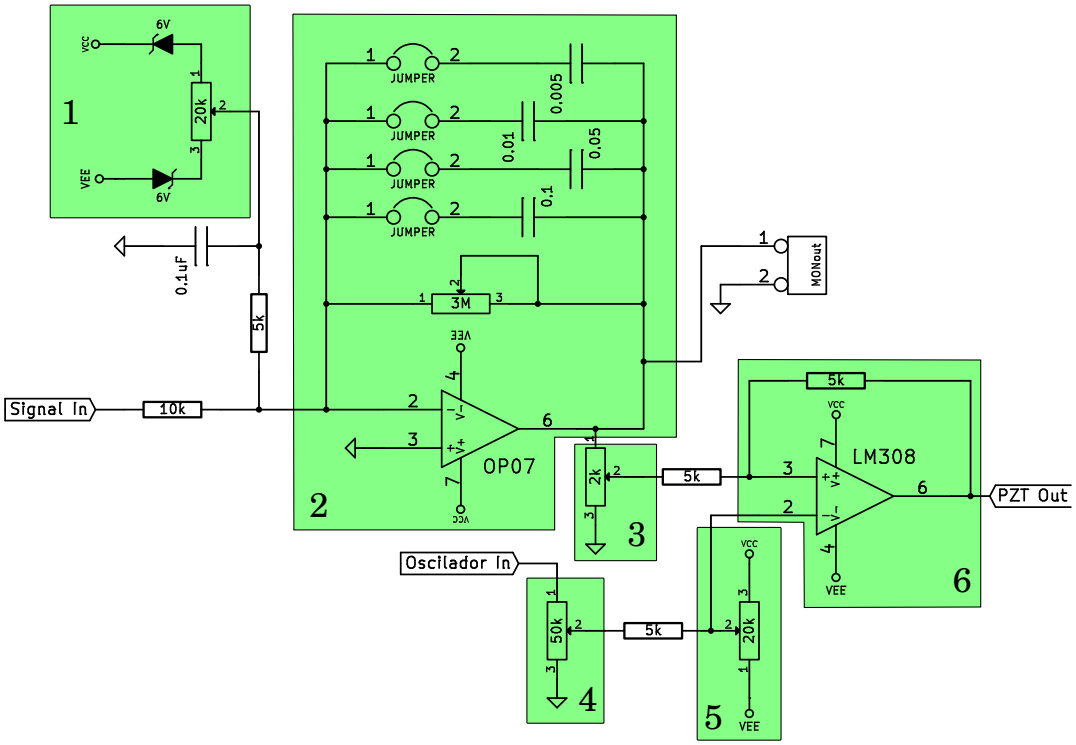

Figure D.1: **Sider-fringe electronics.** Block 1 sets the reference voltage which is compared to the input singal (Singal In) at the entrance of block 2. Block 2 compared the input and reference signal with a very high gain damped amplification stage which serves as comparator and PI loop. Block 3 sets the overall gain of of the loop. Blocks 4 and 5 allow for an external modulation signal as well as setting an offset. Finally all signals are added in an operational amplifier in block 6 and sent to the piezoelectric disk (PZT Out).

stabilization method is to produce a phase sensitive signal at the interferometer. This way one can detect whether one is on one side or the other of a peak. To do so, a small modulation is introduced at the piezoelectric disk. This modulation will produce an error singal with a modulation that will be in or out of phase depending on which side of the peak one is at. Figure D.2 schematically exemplifies this idea.

The phase sensitive signal is then compared to the reference signal producing an error signal which is proportional to the phase difference between the modulation and the response. The circuit in Figure D.3 is used to compare the relative phase between both signals. The idea for this circuit was taken from the book The Art of Electronics[HH89] and from class notes of a course on electronics by Jorge Aliaga[Ali]. The output of this circuit is is sent to the same PI circuit as in the sider-fringe method with its set point is always fixed at zero.

There are three relevant times which must be taken into account for the design of a proper lock-in module as shown. The characteristic time at which the interferometer moves and that one wants to correct T_{sig}. The integration time T_{int} and the modulation time T_{mod}. The design parameters must be chosen such that $T_{sig} \gg T_{int} \gg T_{mod}$. In the our setup we had approximately $T_{sig} \approx 1s$, $T_{int} \approx 50ms$ $T_{mod} \approx 0.5ms$.

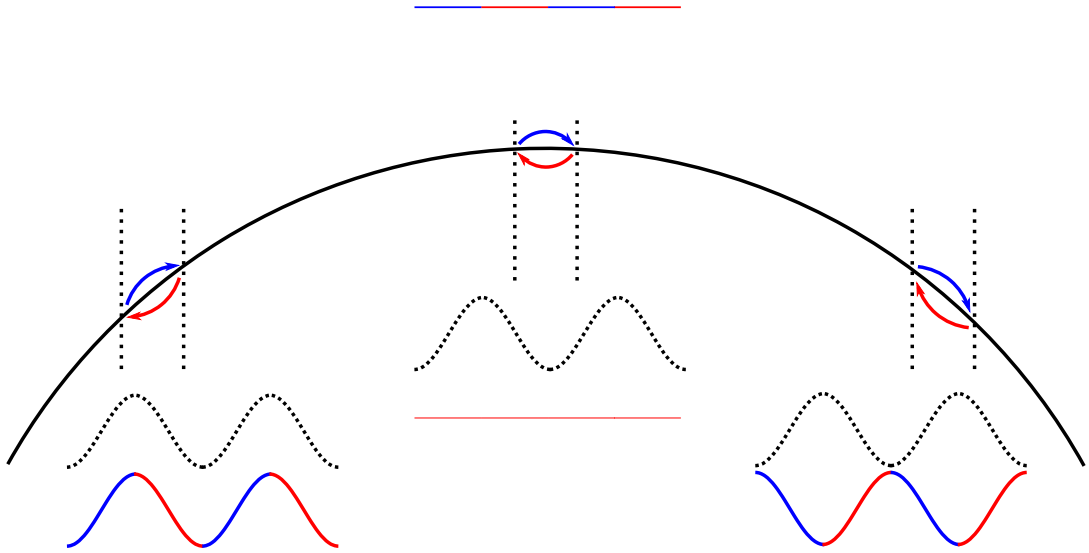

Figure D.2: Idea behind lock in phase sensitive signal generation. The back curve shows the response at the photo-diode as a function of the position of the mirror. When introducing a small modulation in this position the modulation in the output signal (red and blue) will be in phase or out of phase with respect to the modulation signal (dashed) depending on which side of the peak one is. At the top the modulation seen at the output will be almost null.

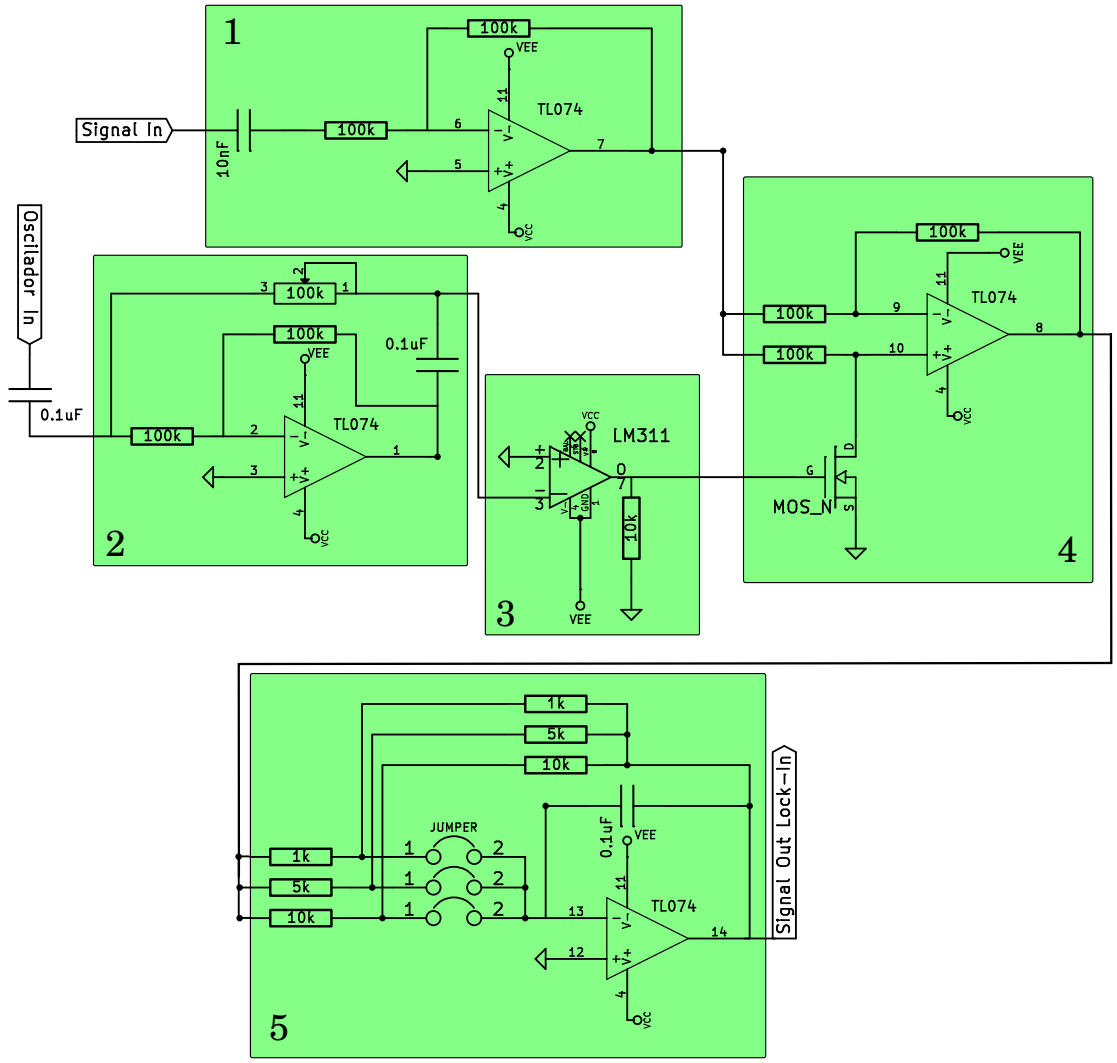

Figure D.3: Lock in amplifier. Block 1 filters the DC component of the signal letting only the AC part in. Block 2 is a phase shifter which acts on the reference signal. In block 3 the reference signal is discretized so as to control the multiplicator of block 4. In block 4 the signal is multiplied alternatively by ± 1 depending on the output of block 3. Finally in block 5 the signal is integrated.

Appendix E

Review of Other QPT Methods

Several methods for complete or partial quantum process characterization have been proposed and demonstrated in different experimental setups [ABJ$^+$03, LWC$^+$08, ESM$^+$07, HTW$^+$06, SKM$^+$09]. A short review of their main ideas and downfalls is presented here.

Ancilla-assisted quantum process tomography

Ancilla-assisted quantum process tomography is a method that uses the duality between channels and states stated by the Choi–Jamiołkowski isomorphism[Cho75, Jam72]. This isomorphism states a one to one relationship between channels and states. This method was proposed in [DC01, DLP01] and realized experimentally on a photonic setup similar to the one used in the experiments of this thesis in [ABJ$^+$03]

To do process tomography with the use of this isomorphism one must evolve a special quantum state chosen in such a way that the output state will be the state isomorphic to the channel. Then by performing tomography on this state one can reconstruct the channel. The problem with this method is that state tomography of this final state is an inefficient task for it involves taking an exponentially large amount of measurements and then inverting a matrix which is also exponentially large. Also a problem of this method is that it requires n extra ancillary qubits.

The state $\rho_{\mathcal{E}}$ isomorphic to a channel $\mathcal{E}$ can be constructed by the application of the channel to one of the parts of bipartite state which is maximally entangled:

$$\rho_{\mathcal{E}} = \frac{1}{D} \left(\mathcal{E} \otimes \mathbb{I}\right) \left(\sum_{i,j} |ii\rangle \langle jj| \right). \tag{E.1}$$

Then by doing state tomography on $\rho_{\mathcal{E}}$ one obtains all the relevant information about the channel. In circuit notation this can be ilustrated as:

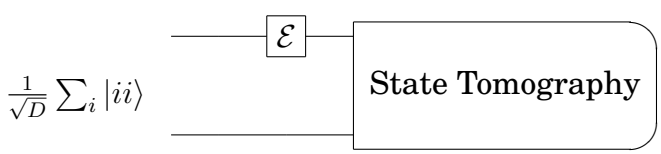

(E.2)

Direct characterization of quantum dynamics

Direct characterization of quantum dynamics is, in a sense an evolution of ancilla-assisted quantum tomography which solves the problem of inverting an exponentially big matrix and allows one to directly measure the diagonal elements of the χ matrix. However for off diagonal elements the the problem of inverting an exponentially big matrix is still present. This method was designed by Lidar and Mosheni [ML06] and experimentally demonstrated by Lui et. at. [LWC$^+$08].

One can see that if one measures in the basis spanned by the states

$$|\psi_k\rangle = \frac{1}{\sqrt{D}} \sum_i E_k \otimes \mathbb{I} \, |ii\rangle \,, \tag{E.3}$$

where E_k are generalized Pauli operators, then the probability of obtaining the state $|\psi_k\rangle$ is exactly the value of χ_{kk}. Thus, just by measuring in this basis, one directly obtains the diagonal matrix elements from the probabilities of the different outcomes.

To obtain the off diagonal elements a non-maximally entangled state must be used, but in this case the coefficients are not obtained directly but through the inversion of a matrix which could be exponentially large.

Symmetrized characterization of noisy quantum processes

Symmetrized characterization of noisy quantum processes[ESM$^+$07] and error characterization in quantum information processing[LLC09] are very similar methods in which the channel is transformed by a set of operations called twirling. By the application of these operations the channels is symmetrized and only diagonal χ matrix elements survive. This allows for easy estimation of general errors which can be used to design error correcting strategies. The method is efficient and requires resources that scale only as the number of qubits.

The bad side of this method is that the symmetrization procedure erases most of the information of the off diagonal coefficients of the χ matrix. For example, one can find that a single bit flip error occurs with certain probability but one will not distinguish on which qubit.

Appendix F

Sampling Without Replacement.

The following demonstration of how the error scales when one samples a finite set of elements without replacing those already measured was provided by Ricardo Piegaia.

If $y = (\sum x_i)/n$, then

$$\begin{aligned} Var(y) &= (1/n^2)[\sum_i Var(x_i) + \sum_{i \neq j} Cov(x_i, x_j)] \\ &= (1/n^2)[nVar(x_i) + n(n-1)Cov(x_i, x_j)] \\ &= \sigma^2/n + [(n-1)/n]Cov(x_i, x_j) \end{aligned} \tag{F.1}$$

One must also calculate for $i \neq j$ the covariance:

$$\begin{aligned} Cov(x_i, x_j) &= \langle x_i x_j \rangle - \langle x_i \rangle \langle x_j \rangle \\ &= \langle x_i x_j \rangle - \langle x \rangle^2 \end{aligned} \tag{F.2}$$

$$\begin{aligned} \langle x_i x_j \rangle &= (\sum_{i \neq j} x_i x_j)/N(N-1) \\ &= (\sum_{i \neq j} x_i x_j + \sum_{i=j} x_i x_j - \sum_{i=j} x_i x_j)/N(N-1) \\ &= (\sum_{i,j} x_i x_j - \sum_i x_i^2)/N(N-1) \\ &= [(\sum x_i)^2 - \sum x_i^2)/N(N-1) \\ &= \frac{N}{N-1}\langle x \rangle^2 - \frac{1}{N-1}\langle x^2 \rangle \end{aligned} \tag{F.3}$$

Then

$$\begin{aligned} Cov(x_i, x_j) &= \langle x_i x_j \rangle - \langle x \rangle^2 \\ &= \frac{1}{N-1}\langle x \rangle^2 - \frac{1}{N-1}\langle x^2 \rangle \\ &= -\sigma^2/(N-1) \end{aligned} \tag{F.4}$$

Replacing in the above equation one obtains:

$$\begin{aligned} Var(y) &= \sigma^2/n - [(n-1)/n]\sigma^2/(N-1) \\ &= \left(1 - \frac{n-1}{N-1}\right)\frac{\sigma^2}{n} \end{aligned} \tag{F.5}$$

Bibliography

[ABJ+03] JB Altepeter, D. Branning, E. Jeffrey, TC Wei, PG Kwiat, RT Thew, JL O Brien, MA Nielsen, and AG White, *Ancilla-assisted quantum process tomography*, Phys. Rev. Lett. **90** (2003), no. 19, 193601.

[ADMHM+07] MP Almeida, F. De Melo, M. Hor-Meyll, A. Salles, SP Walborn, PH Ribeiro, and L. Davidovich, *Environment-induced sudden death of entanglement*, Science **316** (2007), no. 5824, 579.

[ADR82] Alain Aspect, Jean Dalibard, and Gérard Roger, *Experimental test of bell's inequalities using time- varying analyzers*, Phys. Rev. Lett. **49** (1982), no. 25, 1804–1807.

[AGS66] FT Arecchi, E. Gatti, and A. Sona, *Time distribution of photons from coherent and gaussian sources* 1*, Physics Letters **20** (1966), no. 1, 27–29.

[AJK] Joe Altepeter, Evan Jeffrey, and Paul Kwiat, *Quantum state tomography*, `http://research.physics.illinois.edu/QI/Photonics/Tomography/`.

[Ali] Jorge Aliaga, *Lock-in. guia de trabajos prácticos n8.*, `http://www.df.uba.ar/users/jaliaga/electronica/P8/Practica_8.pdf`.

[Are65] F. T. Arecchi, *Measurement of the statistical distribution of gaussian and laser sources*, Phys. Rev. Lett. **15** (1965), 912–916.

[BAH+10] R.C. Bialczak, M. Ansmann, M. Hofheinz, E. Lucero, M. Neeley, AD O'Connell, D. Sank, H. Wang, J. Wenner, M. Steffen, et al., *Quantum process tomography of a universal entangling gate implemented with josephson phase qubits*, Nature Physics **6** (2010), no. 6, 409–413.

[BBB02] Ryan S. Bennink, Sean J. Bentley, and Robert W. Boyd, *"two-photon" coincidence imaging with a classical source*, Phys. Rev. Lett. **89** (2002), 113601.

[BBB09] D. Branning, S. Bhandari, and M. Beck, *Low-cost coincidence-counting electronics for undergraduate quantum optics*, American Journal of Physics **77** (2009), 667.

[BBDM+98] D. Boschi, S. Branca, F. De Martini, L. Hardy, and S. Popescu, *Experimental realization of teleporting an unknown pure quantum state via dual classical and einstein-podolsky-rosen channels*, Physical Review Letters **80** (1998), no. 6, 1121–1125.

[BBRV08] Bandyopadhyay, Boykin, Roychowdhury, and Vatan, *A new proof for the existence of mutually unbiased bases*, Algorithmica **34** (2008), 512–528.

[BCJD99] Gavin K. Brennen, Carlton M. Caves, Poul S. Jessen, and Ivan H. Deutsch, *Quantum logic gates in optical lattices*, Phys. Rev. Lett. **82** (1999), 1060–1063.

[BCMDM05] M. Barbieri, C. Cinelli, P. Mataloni, and F. De Martini, *Polarization-momentum hyperentangled states: Realization and characterization*, Phys. Rev. A **72** (2005), 052110.

[BDPS99] K. Banaszek, G. M. D'Ariano, M. G. A. Paris, and M. F. Sacchi, *Maximum-likelihood estimation of the density matrix*, Phys. Rev. A **61** (1999), 010304.

[Bel87] J. S. Bell, *Speakable and unspeakable in quantum mechanics*, Cambridge University Press, 1987.

[Ben06] Ariel Bendersky, *Conjuntos de Bases Mutuamente No Sesgadas y Sus Aplicaciones*, Master's thesis, Universidad de Buenos Aires, Argentina, 2006.

[Ben11] Ariel Martín Bendersky, *Nuevos algoritmos cuánticos para tomografíde procesos y estados*, Ph.D. thesis, Universidad de Buenos Aires, 2011.

[BLPK05] Julio T. Barreiro, Nathan K. Langford, Nicholas A. Peters, and Paul G. Kwiat, *Generation of hyperentangled photon pairs*, Phys. Rev. Lett. **95** (2005), 260501.

[BmcHHH00] Piotr Badziąg, Michał Horodecki, Paweł Horodecki, and Ryszard Horodecki, *Local environment can enhance fidelity of quantum teleportation*, Phys. Rev. A **62** (2000), 012311.

[BPC09] Ariel Bendersky, Juan Pablo Paz, and Marcelo Terra Cunha, *General theory of measurement with two copies of a quantum state*, Phys. Rev. Lett. **103** (2009), 040404.

[BPM+97] D. Bouwmeester, J.W. Pan, K. Mattle, M. Eibl, H. Weinfurter, and A. Zeilinger, *Experimental quantum teleportation*, Nature **390** (1997), no. 6660, 575–579.

[BPP08] A. Bendersky, F. Pastawski, and J.P. Paz, *Selective and efficient estimation of parameters for quantum process tomography*, Phys. Rev. Lett. **100** (2008), no. 19, 190403.

[BPP09] _____, *Selective and efficient quantum process tomography*, Phys. Rev. A **80** (2009), no. 3, 32116.

[BPS+08] H. Benítez, L. Perez, C.T. Schmiegelow, M.G. Kovalsky, M.A. Larotonda, and A.A. Hnilo, *Generador cuántico de números aleatorios*, Anales AFA (2008).

[BSS+10] Irene Bongioanni, Linda Sansoni, Fabio Sciarrino, Giuseppe Vallone, and Paolo Mataloni, *Experimental quantum process tomography of non-trace-preserving maps*, Phys. Rev. A **82** (2010), 042307.

[BvL05] Samuel L. Braunstein and Peter van Loock, *Quantum information with continuous variables*, Rev. Mod. Phys. **77** (2005), 513–577.

[CDS+11] M G Capeluto, H Duisterwinkel, C T Schmiegelow, D Francisco, S Ledesma, and C Iemmi, *Ghost imaging and ghost diffraction with pseudo-thermal light generated by means of a programmable slm*, Journal of Physics: Conference Series **274** (2011), no. 1, 012004.

[Cho75] M Choi, *Completely positive linear maps on complex matrices*, October **10** (1975), no. 3, 285–290.

[CRO+11] A. Crespi, R. Ramponi, R. Osellame, L. Sansoni, I. Bongioanni, F. Sciarrino, G. Vallone, and P. Mataloni, *Integrated photonic quantum gates for polarization qubits*, Arxiv preprint arXiv:1105.1454 (2011).

[Dan05] Christoph Dankert, *Efficient Simulation of Random Quantum States and Operators*, Master's thesis, University of Waterloo, Canada, 2005.

[DC01] W. Dür and J. I. Cirac, *Nonlocal operations: Purification, storage, compression, tomography, and probabilistic implementation*, Phys. Rev. A **64** (2001), 012317.

[DCEL09] C. Dankert, R. Cleve, J. Emerson, and E. Livine, *Exact and approximate unitary 2-designs and their application to fidelity estimation*, Phys. Rev. A **80** (2009), no. 1, 012304.

[DeM02] D. DeMille, *Quantum computation with trapped polar molecules*, Phys. Rev. Lett. **88** (2002), 067901.

[DGN99] Valentin G. Dmitriev, Gagik G. Gurzadyan, and David N. Nikogosyan, *Handbook of nonlinear optical crystals (springer series in optical sciences)*, Springer, 1999.

[DGS77] P. Delsarte, J.M. Goethals, and J.J. Seidel, *Spherical codes and designs*, Geom. Dedicata **6** (1977), no. 3, 363–388.

[DiV00] D.P. DiVincenzo, *The physical implementation of quantum computation*, Arxiv preprint quant-ph/0002077 (2000).

[DLP01] G. M. D'Ariano and P. Lo Presti, *Quantum tomography for measuring experimentally the matrix elements of an arbitrary quantum operation*, Phys. Rev. Lett. **86** (2001), 4195–4198.

[DM02] D. Dehlinger and MW Mitchell, *Entangled photon apparatus for the undergraduate laboratory*, American Journal of Physics **70** (2002), 898.

[DM10] L.-M. Duan and C. Monroe, *Colloquium: Quantum networks with trapped ions*, Rev. Mod. Phys. **82** (2010), 1209–1224.

[EKW01] B.G. Englert, C. Kurtsiefer, and H. Weinfurter, *Universal unitary gate for single-photon two-qubit states*, Phys. Rev. A **63** (2001), no. 3, 32303.

[ESM+07] J. Emerson, M. Silva, O. Moussa, C. Ryan, M. Laforest, J. Baugh, D.G. Cory, and R. Laflamme, *Symmetrized characterization of noisy quantum processes*, Science **317** (2007), no. 5846, 1893.

[Exc] Excelitas, *Avalanche photodiodes datasheet*, `http://www.excelitas.com/downloads/dts_pe_pd_09_avalanchephotodiodes.pdf`.

[FH01] J. Fiurášek and Z. Hradil, *Maximum-likelihood estimation of quantum processes*, Phys. Rev. A **63** (2001), 020101.

[FW04] Marco Fiorentino and Franco N. C. Wong, *Deterministic controlled-not gate for single-photon two-qubit quantum logic*, Phys. Rev. Lett. **93** (2004), 070502.

[GC99] D. Gottesman and I. Chuang, *Demostrating the viability of universal quantum computation using teleportation and single qubit operations*, Nature (London) **402** (1999), 390.

[GHW04] Kathleen S. Gibbons, Matthew J. Hoffman, and William K. Wootters, *Discrete phase space based on finite fields*, Phys. Rev. A **70** (2004), 062101.

[GLN05] Alexei Gilchrist, Nathan K. Langford, and Michael A. Nielsen, *Distance measures to compare real and ideal quantum processes*, Phys. Rev. A **71** (2005), 062310.

[Ham] Hamamatsu, *Photon counting - using photomultiplier tubes*, `http://sales.hamamatsu.com/assets/applications/ETD/Photon_Counting.pdf`.

[HH89] P. Horowitz and W. Hill, *The art of electronics*, vol. 2, Cambridge university press Cambridge, 1989.

[HMM03] Andrew P. Hines, Ross H. McKenzie, and Gerard J. Milburn, *Entanglement of two-mode bose-einstein condensates*, Phys. Rev. A **67** (2003), 013609.

[HOM87] C. K. Hong, Z. Y. Ou, and L. Mandel, *Measurement of subpicosecond time intervals between two photons by interference*, Phys. Rev. Lett. **59** (1987), 2044–2046.

[HSP10] Klemens Hammerer, Anders S. Sørensen, and Eugene S. Polzik, *Quantum interface between light and atomic ensembles*, Rev. Mod. Phys. **82** (2010), 1041–1093.

[HT02] Holger F. Hofmann and Shigeki Takeuchi, *Quantum phase gate for photonic qubits using only beam splitters and postselection*, Phys. Rev. A **66** (2002), no. 2, 024308.

[HTW+06] M Howard, J Twamley, C Wittmann, T Gaebel, F Jelezko, and J Wrachtrup, *Quantum process tomography and linblad estimation of a solid-state qubit*, New Journal of Physics **8** (2006), no. 3, 33.

[Jam72] A. Jamiolkowski, *Completely positive linear maps on complex matrices*, Rep. Math. Phys. **3** (1972), 275.

[Jon05] J. A. Jones, *Nmr quantum computation: A critical evaluation*, pp. 139–154, Wiley-VCH Verlag GmbH & Co. KGaA, 2005.

[KBKY99] J. Kim, O. Benson, H. Kan, and Y. Yamamoto, *A single-photon turnstile device*, Nature **397** (1999), no. 6719, 500–503.

[KLM01] E. Knill, R. Laflamme, and G. J. Milburn, *A scheme for efficient quantum computation with linear optics*, Nature (London) **409** (2001), 46–52.

[KMN+07] Pieter Kok, W. J. Munro, Kae Nemoto, T. C. Ralph, Jonathan P. Dowling, and G. J. Milburn, *Linear optical quantum computing with photonic qubits*, Rev. Mod. Phys. **79** (2007), 135–174.

[KMW+95] Paul G. Kwiat, Klaus Mattle, Harald Weinfurter, Anton Zeilinger, Alexander V. Sergienko, and Yanhua Shih, *New high-intensity source of polarization-entangled photon pairs*, Phys. Rev. Lett. **75** (1995), 4337–4341.

[KMZW00] Christian Kurtsiefer, Sonja Mayer, Patrick Zarda, and Harald Weinfurter, *Stable solid-state source of single photons*, Phys. Rev. Lett. **85** (2000), 290–293.

[KOW01] Christian Kurtsiefer, Markus Oberparleiter, and Harald Weinfurter, *High-efficiency entangled photon pair collection in type-ii parametric fluorescence*, Phys. Rev. A **64** (2001), 023802.

[KR05] A. Klappenecker and M. Rotteler, *Mutually unbiased bases are complex projective 2-designs*, ISIT 2005. Proc. Int. Symposium on Information Theory, 2005, p. 1740.

[KSW+05] Nikolai Kiesel, Christian Schmid, Ulrich Weber, Rupert Ursin, and Harald Weinfurter, *Linear optics controlled-phase gate made simple*, Physical Review Letters **95** (2005), no. 21, 210505.

[KWO+10] R. Krischek, W. Wieczorek, A. Ozawa, N. Kiesel, P. Michelberger, T. Udem, and H. Weinfurter, *Ultraviolet enhancement cavity for ultrafast nonlinear optics and high-rate multiphoton entanglement experiments*, Nature Photonics **4** (2010), no. 3, 170–173.

[KWW+99] Paul G. Kwiat, Edo Waks, Andrew G. White, Ian Appelbaum, and Philippe H. Eberhard, *Ultrabright source of polarization-entangled photons*, Phys. Rev. A **60** (1999), R773–R776.

[KYI01] Masato Koashi, Takashi Yamamoto, and Nobuyuki Imoto, *Probabilistic manipulation of entangled photons*, Phys. Rev. A **63** (2001), no. 3, 030301.

[LBPC10] C. C. López, A. Bendersky, J. P. Paz, and D. G. Cory, *Progress toward scalable tomography of quantum maps using twirling-based methods and information hierarchies*, Phys. Rev. A **81** (2010), no. 6, 062113.

[LBZ02] J. Lawrence, Č. Brukner, and A. Zeilinger, *Mutually unbiased binary observable sets on N qubits*, Phys. Rev. A **65** (2002), no. 3, 032320.

[LD98] Daniel Loss and David P. DiVincenzo, *Quantum computation with quantum dots*, Phys. Rev. A **57** (1998), 120–126.

[LJR+09] J. Leach, B. Jack, J. Romero, M. Ritsch-Marte, R. W. Boyd, A. K. Jha, S. M. Barnett, S. Franke-Arnold, and M. J. Padgett, *Violation of a bell inequality in two-dimensional orbital angular momentum state-spaces*, Opt. Express **17** (2009), no. 10, 8287–8293.

[LLC09] C. C. López, B. Lévi, and D. G. Cory, *Error characterization in quantum information processing: A protocol for analyzing spatial correlations and its experimental implementation*, Phys. Rev. A **79** (2009), no. 4, 042328.

[Lóp09] C. C. López, *Scalable approaches to the characterization of open quantum system dynamics*, Ph.D. thesis, Massachusetts Institute of Technology, Cambridge, MA, USA, 2009.

[Lou00] R. Loudon, *The quantum theory of light*, Oxford University Press, USA, 2000.

[LR09] A. I. Lvovsky and M. G. Raymer, *Continuous-variable optical quantum-state tomography*, Rev. Mod. Phys. **81** (2009), 299–332.

[LVN+09] G. Lima, A. Vargas, L. Neves, R. Guzmán, and C. Saavedra, *Manipulating spatial qudit states with programmable optical devices*, Optics Express **17** (2009), no. 13, 10688–10696.

[LWC+08] W.T. Liu, W. Wu, P.X. Chen, C.Z. Li, and J.M. Yuan, *Direct characterization of quantum dynamics with single-photon two-qubit states*, Phys. Rev. A **77** (2008), no. 3, 032328.

[LWP+05] N. K. Langford, T. J. Weinhold, R. Prevedel, K. J. Resch, A. Gilchrist, J. L. O'Brien, G. J. Pryde, and A. G. White, *Demonstration of a simple entangling optical gate and its use in bell-state analysis*, Physical Review Letters **95** (2005), no. 21, 210504.

[Mel90] P. A. Mello, *Averages on the unitary group and applications to the problem of disordered conductors*, Journal of Physics A: Mathematical and General **23** (1990), no. 18, 4061+.

[MFP08] Nicolas C. Menicucci, Steven T. Flammia, and Olivier Pfister, *One-way quantum computing in the optical frequency comb*, Phys. Rev. Lett. **101** (2008), 130501.

[MG07] G. McConnell and D. Gross, *Efficient 2-designs from bases exist*, Arxiv preprint arXiv:0710.1502 (2007).

[Mil89] G. J. Milburn, *Quantum optical fredkin gate*, Phys. Rev. Lett. **62** (1989), 2124–2127.

[MKB+00] P. Michler, A. Kiraz, C. Becher, W. V. Schoenfeld, P. M. Petroff, Lidong Zhang, E. Hu, and A. Imamoglu, *A quantum dot single-photon turnstile device*, Science **290** (2000), no. 5500, 2282–2285.

[MKH+09] T. Monz, K. Kim, W. Hänsel, M. Riebe, A. S. Villar, P. Schindler, M. Chwalla, M. Hennrich, and R. Blatt, *Realization of the quantum toffoli gate with trapped ions*, Phys. Rev. Lett. **102** (2009), 040501.

[ML06] M. Mohseni and D. A. Lidar, *Direct characterization of quantum dynamics*, Phys. Rev. Lett. **97** (2006), 170501.

[MMWZ96] Markus Michler, Klaus Mattle, Harald Weinfurter, and Anton Zeilinger, *Interferometric bell-state analysis*, Phys. Rev. A **53** (1996), no. 3, R1209–R1212.

[MQK+09] X. Ma, A. Qarry, J. Kofler, T. Jennewein, and A. Zeilinger, *Experimental violation of a bell inequality with two different degrees of freedom of entangled particle pairs*, Physical Review A **79** (2009), no. 4, 042101.

[MRP98] C. H. Monken, P. H. Souto Ribeiro, and S. Pádua, *Transfer of angular spectrum and image formation in spontaneous parametric down-conversion*, Phys. Rev. A **57** (1998), 3123–3126.

[MSB+11] Thomas Monz, Philipp Schindler, Julio T. Barreiro, Michael Chwalla, Daniel Nigg, William A. Coish, Maximilian Harlander, Wolfgang Hänsel, Markus Hennrich, and Rainer Blatt, *14-qubit entanglement: Creation and coherence*, Phys. Rev. Lett. **106** (2011), 130506.

[MSL09] M.G. Mingolla, C.T. Schmiegelow, and M.A. Larotonda, *Fuente de pares de fotones entrelazados en polarización.*, Anales AFA (2009).

[MSS01] Yuriy Makhlin, Gerd Schön, and Alexander Shnirman, *Quantum-state engineering with josephson-junction devices*, Rev. Mod. Phys. **73** (2001), 357–400.

[MSW92] KB MacAdam, A. Steinbach, and C. Wieman, *A narrow-band tunable diode laser system with grating feedback, and a saturated absorption spectrometer for cs and rb*, American Journal of Physics **60** (1992), 1098.

[MVWZ01] A. Mair, A. Vaziri, G. Weihs, and A. Zeilinger, *Entanglement of the orbital angular momentum states of photons*, Nature **412** (2001), no. 6844, 313–316.

[MW95] L. Mandel and E. Wolf, *Optical coherence and quantum optics*, Cambridge Univ Pr, 1995.

[MWKZ96] Klaus Mattle, Harald Weinfurter, Paul G. Kwiat, and Anton Zeilinger, *Dense coding in experimental quantum communication*, Phys. Rev. Lett. **76** (1996), no. 25, 4656–4659.

[NAB+08] M. Neeley, M. Ansmann, R.C. Bialczak, M. Hofheinz, N. Katz, E. Lucero, A. O'Connell, H. Wang, AN Cleland, and J.M. Martinis, *Process tomography of quantum memory in a josephson-phase qubit coupled to a two-level state*, Nature Physics **4** (2008), no. 7, 523–526.

[NC00] M. A. Nielsen and I. L. Chuang, *Quantum computation and quantum information*, Cambridge University Press, 2000.

[OHTS05] Ryo Okamoto, Holger F. Hofmann, Shigeki Takeuchi, and Keiji Sasaki, *Demonstration of an optical quantum controlled-not gate without path interference*, Physical Review Letters **95** (2005), no. 21, 210506.

[PCR+08] Alberto Politi, Martin J. Cryan, John G. Rarity, Siyuan Yu, and Jeremy L. O'Brien, *Silica-on-silicon waveguide quantum circuits*, Science **320** (2008), no. 5876, 646–649.

[Per] PerkinElmer, *Avalanche photodiode: A user guide*, `http://www.perkinelmer.com/CMSResources/Images/44-6538APP_AvalanchePhotodiodesUsersGuide.pdf`.

[Per84] Asher Peres, *Stability of quantum motion in chaotic and regular systems*, Phys. Rev. A **30** (1984), 1610–1615.

[PJF01] T. B. Pittman, B. C. Jacobs, and J. D. Franson, *Probabilistic quantum logic operations using polarizing beam splitters*, Phys. Rev. A **64** (2001), no. 6, 062311.

[PLU95] Horacio M. Pastawski, Patricia R. Levstein, and Gonzalo Usaj, *Quantum dynamical echoes in the spin diffusion in mesoscopic systems*, Phys. Rev. Lett. **75** (1995), 4310–4313.

[PR04] Arthur O. Pittenger and Morton H. Rubin, *Mutually unbiased bases, generalized spin matrices and separability*, Linear Algebra and its Applications **390** (2004), 255 – 278.

[PRS05] Juan Pablo Paz, Augusto José Roncaglia, and Marcos Saraceno, *Qubits in phase space: Wigner-function approach to quantum-error correction and the mean-king problem*, Phys. Rev. A **72** (2005), no. 1, 012309.

[PRS+10] N. Piro, F. Rohde, C. Schuck, M. Almendros, J. Huwer, J. Ghosh, A. Haase, M. Hennrich, F. Dubin, and J. Eschner, *Heralded single-photon absorption by a single atom*, Nature Physics (2010).

[PZ02] J. Paz and W. Zurek, *Environment-induced decoherence and the transition from quantum to classical*, Fundamentals of Quantum Information (2002), 77–148.

[RBKSS05] J. L. Romero, G. Björk, A. B. Klimov, and L. L. Sánchez-Soto, *Structure of the sets of mutually unbiased bases for n qubits*, Phys. Rev. A **72** (2005), no. 6, 062310.

[RBSC04] J. M. Renes, R. Blume-Kohout, A. J. Scott, and C. M. Caves, *Symmetric informationally complete quantum measurements*, Journal of Mathematical Physics **45** (2004), 2171–2180.

[RLBW02] T. C. Ralph, N. K. Langford, T. B. Bell, and A. G. White, *Linear optical controlled-not gate in the coincidence basis*, Phys. Rev. A **65** (2002), no. 6, 062324.

[RT90] J. G. Rarity and P. R. Tapster, *Experimental violation of bell's inequality based on phase and momentum*, Phys. Rev. Lett. **64** (1990), 2495–2498.

[Sac01] Massimiliano F. Sacchi, *Maximum-likelihood reconstruction of completely positive maps*, Phys. Rev. A **63** (2001), 054104.

[Sak85] J.J. Sakurai, *Modern quantum mechanics*, Reading, MA: Addison Wesley,— c1985, edited by Tuan, San Fu **1** (1985).

[Sam80] Stuart Samuel, $\mathrm{U}(N)$ *integrals,* $1/N$*, and the De Wit-'t Hooft anomalies*, J. Math. Phys. **21** (1980), no. 12, 2695–2703.

[SCB+11] A. Stute, B. Casabone, B. Brandstatter, D. Habicher, PO Schmidt, TE Northup, and R. Blatt, *Toward an ion-photon quantum interface in an optical cavity*, Arxiv preprint arXiv:1105.0579 (2011).

[SGG+02] D Stucki, N Gisin, O Guinnard, G Ribordy, and H Zbinden, *Quantum key distribution over 67 km with a plug & play system*, New Journal of Physics **4** (2002), no. 1, 41.

[SKK01] K. Sanaka, K. Kawahara, and T. Kuga, *Franson-type experiment realizes two-qubit quantum logic gate*, Arxiv preprint quant-ph/0108001 (2001).

[SKM+09] A. Shabani, R. L. Kosut, M. Mohseni, H. Rabitz, M. A. Broome, M. P. Almeida, A. Fedrizzi, and A. G. White, *Efficient measurement of quantum dynamics via compressive sensing*, ArXiv e-prints (2009).

[SMWF+07] Tobias Schmitt-Manderbach, Henning Weier, Martin Fürst, Rupert Ursin, Felix Tiefenbacher, Thomas Scheidl, Josep Perdigues, Zoran Sodnik, Christian Kurtsiefer, John G. Rarity, Anton Zeilinger, and Harald Weinfurter, *Experimental demonstration of free-space decoy-state quantum key distribution over 144 km*, Phys. Rev. Lett. **98** (2007), 010504.

[SWM10] M. Saffman, T. G. Walker, and K. Mølmer, *Quantum information with rydberg atoms*, Rev. Mod. Phys. **82** (2010), 2313–2363.

[Tak11] Bruno Taketani, *Teletransporte quântico e descoerência*, Ph.D. thesis, Universidade Federal do Rio de Janeiro, 2011.

[TGT+11] D. S. Tasca, R. M. Gomes, F. Toscano, P. H. Souto Ribeiro, and S. P. Walborn, *Continuous-variable quantum computation with spatial degrees of freedom of photons*, Phys. Rev. A **83** (2011), 052325.

[TND+04] JJ Thorn, MS Neel, VW Donato, GS Bergreen, RE Davies, and M. Beck, *Observing the quantum behavior of light in an undergraduate laboratory*, American journal of physics **72** (2004), 1210.

[VC05] L. M. K. Vandersypen and I. L. Chuang, *Nmr techniques for quantum control and computation*, Rev. Mod. Phys. **76** (2005), 1037–1069.

[Wal04] Stephen Patrick Walborn, *The brothers q: Multimode entangled photons with parametric down conversion*, Ph.D. thesis, Universidade Federal de Minas Gerais, 2004.

[WGP+07] A.G. White, A. Gilchrist, G.J. Pryde, J.L. O'Brien, M.J. Bremner, and N.K. Langford, *Measuring two-qubit gates*, JOSA B **24** (2007), no. 2, 172–183.

[Wika] Wikipedia, *Diode iv curve.*, `http://en.wikipedia.org/wiki/File:Diode-IV-Curve.svg`.

[Wikb] _____, *Superconducting nanowire single-photon detector*, `http://en.wikipedia.org/wiki/Superconducting_nanowire_single-photon_detector`.

[WJS+98] Gregor Weihs, Thomas Jennewein, Christoph Simon, Harald Weinfurter, and Anton Zeilinger, *Violation of bell's inequality under strict einstein locality conditions*, Phys. Rev. Lett. **81** (1998), 5039–5043.

[WMPR10] S.P. Walborn, C.H. Monken, S. Pádua, and P.H. Souto Ribeiro, *Spatial correlations in parametric down-conversion*, Physics Reports **495** (2010), no. 4-5, 87 – 139.

[WRD+06] SP Walborn, P.H.S. Ribeiro, L. Davidovich, F. Mintert, and A. Buchleitner, *Experimental determination of entanglement with a single measurement*, Nature **440** (2006), no. 7087, 1022–1024.

[WRD+07] S. P. Walborn, P. H. Souto Ribeiro, L. Davidovich, F. Mintert, and A. Buchleitner, *Experimental determination of entanglement by a projective measurement*, Phys. Rev. A **75** (2007), 032338.